Alanine-EPR dosimetry in remote audits of clinical photon beams

Hans Lindbo Røpke-Haarsløv

Internal supervisor: Ian Bearden *Niels Bohr Institute, University of Copenhagen*

External supervisor: Claus E. Andersen *Center for Nuclear Technologies, Technical University of Denmark*

August 31, 2016

Abstract

There is a need for multiple independent auditing methods for clinical photon beams, for which alanine-EPR dosimeters could be a candidate. In this thesis we attempt to solve some key questions related to developing the alanine remote audit dosimetry system for traceable measurements at DTU Risø(SSDL): **1.** which of the two ^{60}Co source designs at Risø are better for developing the alanine dosimetry system? **2.** What is the energy response for alanine dosimeters in MV-beams, and is there a trend in the response as a function of beam quality? **3.** Propose a method in which alanine can be used for remote audits of clinical photon beams at Danish hospitals.

Calibration curves of irradiated alanine in the dose-range 1 - 100 Gy are made for both source designs and they are compared on a number of parameters. We find the open source design to be preferable because of low traceability uncertainty and customizable choice of effective measuring point in the calibration. The energy dependence of alanine dosimeters where found experimentally by MV-irradiations of alanine and Farmer chamber dosimeters, and simulated using the egsNRC software for Monte Carlo simulations of particle transport. The experimental results had relative uncertainties of 1.2%, dominated by the uncertainty in the calculated Farmer chamber k_Q values. The uncertainties were too high for detecting a trend beyond a constant dependence in beam quality. The simulated results showed a constant energy dependence of $H_Q = 0.9961 \pm 0.0004$ for MV-beams in the reference conditions of the performed experiment, we argue that changes in either the phantom or the effective point of measurement(for alanine dosimeters) could give a different H_Q. We describe two possible auditing procedures: a dose-rate audit with traceable relative uncertainty 0.7%, and a dose-distribution audit of the treatment planning system of clinical photon beams. Both procedures are relatively simple to perform and require special made phantoms, that can be mailed as part of the remote audit.

Contents

1 Introduction **4**

2 Purpose **4**

3 Theory **5**
- 3.1 The Atom and its Nucleus . . . 5
  - 3.1.1 Liquid Drop Model . . . 6
- 3.2 Types of Radiation . . . 7
  - 3.2.1 Alpha Emission . . . 7
  - 3.2.2 Isobaric Transitions . . . 8
  - 3.2.3 Gamma Radiation . . . 9
  - 3.2.4 Internal Conversion . . . 9
- 3.3 Radiation Interacting with Matter . . . 10
  - 3.3.1 Cross Sections . . . 10
  - 3.3.2 Charged Particles . . . 11
  - 3.3.3 Photons . . . 14
- 3.4 Dose Kerma and Dosimetric Principles . . . 17
  - 3.4.1 Kerma . . . 18
  - 3.4.2 Dose . . . 19
  - 3.4.3 Cavity Theory . . . 20
  - 3.4.4 Absolute and Relative Dosimetry . . . 21
- 3.5 Statistics . . . 23
  - 3.5.1 Statistical Formalism . . . 23
  - 3.5.2 χ^2 Distribution . . . 24
  - 3.5.3 Runs Test . . . 25

4 Alanine-EPR Dosimetry **25**
- 4.1 Magnetic Moment . . . 25
- 4.2 Alanine and Free Radicals . . . 26
- 4.3 EPR . . . 27
- 4.4 Spectrum Analysis . . . 28
- 4.5 Energy Dependence . . . 30
- 4.6 Bruker EMX-micro . . . 32

5 Ionisation Chamber Dosimetry **33**
- 5.1 Farmer Chamber Correction Factors . . . 34

6 Monte Carlo **36**
- 6.1 Random Sampling in egsNRC . . . 36
- 6.2 Condensed Histories . . . 38
- 6.3 User Codes and Uncertainty . . . 39

7 Experiments and Simulations **39**
7.1 Open Source Geometry . . . 39
7.1.1 Results . . . 42
7.2 Closed Geometry . . . 44
7.2.1 Results . . . 45
7.3 MV-Irradiations . . . 46
7.3.1 Results . . . 48
7.4 Monte Carlo Simulations . . . 51
7.4.1 Results . . . 52

8 Analysis and Discussion **52**
8.1 Cobalt Source Geometry Comparison . . . 52
8.1.1 Uncertainty in Matching Reference Conditions . . . 52
8.1.2 Background Calculations . . . 54
8.1.3 Asymmetrical EPR Readout . . . 54
8.1.4 Calibration Uncertainties . . . 55
8.1.5 Dose Determination Uncertainty . . . 60
8.1.6 Geometry Comparison . . . 62
8.2 Alanine Energy Dependence . . . 63
8.2.1 Background Calculations . . . 63
8.2.2 Monitor Chamber . . . 63
8.2.3 Asymmetrical EPR readout . . . 63
8.2.4 Polarity Deviation . . . 63
8.2.5 Temperature Interpolation . . . 63
8.2.6 $TPR_{20,10}$ Uncertainty . . . 64
8.2.7 k_Q Factors. . . . 66
8.2.8 Vertical Water Tank Placement . . . 67
8.2.9 F_{Q,Q_0} . . . 67
8.2.10 H_{Q,Q_0} . . . 69
8.3 Possibility of Audits . . . 71
8.3.1 Current Clinical Applications of Alanine . . . 72
8.3.2 Risø's Alanine Dosimetry System for Auditing Clinical Photon Beams 73

9 Conclusion **74**

References **76**

1 Introduction

Dosimetry is the field of quantifying and measuring the energy deposited to a medium, by any type of radiation. The importance of dosimetry is best viewed in reference to Intensity Modulated Radiotherapy(IMRT), where a human body is irradiated with certain intensities from different directions, in order to give a high dose in the tumour area and minimal dose in the surrounding tissue. Cancer cells are very sensitive to radiation because they can't repair themselves as effectively as normal cells, but radiation is also a carcinogen in itself, so too high a dose would kill the tumour but also increase the chance of developing a new cancer in a near future, and too low a dose would not remove the tumour completely. Errors in the dose-rate therefore has fatal consequences, and the clinical photon beams, used for radiotherapy must be inspected for errors often by multiple independent methods. Current methods include ionisation chambers and Thermal Luminescence dosimeters(TLD). Alanine-EPR dosimetry has been used for decades in calibration of industrial irradiations, but the National Physics Laboratory of the UK(NPL) [44] proposed that it could be used as an auditing tool for clinical photon beams. Alanine is a solid-state dosimeter where the production of free radicals can be read out using electron spin resonance spectroscopy. Alanine has a highly linear and stable dose to signal response, and has many favourable aspects for remote audit dosimetry: low beam energy signal dependence, non-destructive dose readout, easy transfer between clinic and laboratory, low signal fading, and tissue equivalence. DTU Risø(secondary standard dosimetric laboratory) want to develop a traceable alanine-EPR dosimetry system for remote auditing of clinical photon beams at Danish hospitals. This thesis attempts to answer three key questions regarding the development of the alanine dosimetry system at DTU Risø.

2 Purpose

The project is a master thesis in physics at the University of Copenhagen. The key research questions are:

- DTU has two ^{60}Co source designs that potentially both can be used for calibration of alanine pellets: gamma cells and free-field sources. Which of these source designs provides the lowest uncertainty on the final result and which are most practical to use?

- We need to measure the absorbed dose to water. What is the difference in energy response for the alanine between the two ^{60}Co source designs and what is the difference from ^{60}Co to the various accelerator photon energies? Do the energy correction factors correlate with the traditional beam quality index? What are the correction factors for the beams at DTU and what correction factors can be used for the beams at Danish hospitals? What is the effective point of measurement?

- Propose a system/method of how the alanine could be used for measurements under reference conditions at Danish hospitals? This work may require that a phantom is designed for this purpose. Estimate the uncertainty for the method including how well the system can be set up. Demonstrate the method at one or more Danish hospitals.

To solve these questions, we will make alanine calibrations for each source design, by irradiating alanine dosimeters to known doses. We will investigate the theory behind energy dependence for dosimeters in general, and obtain both experimental(from photon beam irradiations) and simulated(Monte Carlo simulations of particle transport) values of energy dependence of alanine dosimeters. An auditing method inspired by the results will be proposed, with expected traceable uncertainty.

3 Theory

3.1 The Atom and its Nucleus

To understand why some atoms are radioactive, we must first understand how the atom is structered. In the scope of atomic physics atoms consists of 3 different particles: the positively charged protons, the neutraly charged neutrons and the negatively charged electrons. Protons and neutrons make up the nucleus of the atom, they are pulled together by the strong nuclear force, when the distance between them is of the order of 10^{-15}m [13]. The electrons are pulled towards the protons in the nucleus by the electromagnetic force, but instead of making classical orbits around the nucleus, like the moon does around the Earth, the atom is a quantum system and must follow the laws of quantum mechanics. In non-relativistic quantum mechanics the behaviour of the atom-bound electrons is calculated by the Scrodinger equation [19]:

$$i\hbar\frac{d\Psi(\vec{r},t)}{dt} = -\frac{\hbar^2}{2m_e}\nabla^2\Psi(\vec{r},t) + V(\vec{r},t)\Psi(\vec{r},t) \tag{1}$$

Where $\hbar$ is Planck's reduced constant, m_e is the mass of the electron, $V(\vec{r},t)$ is the electric coulumb potential from the positively charged nucleus and the repulsion from potential other electrons in the same atom. $\Psi(\vec{r},t)$ is the wave function describing the possible whereabouts for the electron at any time t, meaning that $|\Psi(\vec{r},t)|^2$ is the probability density function for the location[1] of the electron. When solving the Scrodinger equation for electrons in atoms, we find that the possible solutions are quantised in energy and angular momentum. The electron state is then categorised by shell($K, L, M, N, O..$), orbital($s, p, d, f, g..$), and spin($\uparrow, \downarrow$), where two electrons are prohibited from occopying the same state following Pauli's exclusion principle [18]. The electrons which occopy the lower shells tends to spend more time near the nucleus and often have a higher binding energy, but for a high atomic number he orbital, which determines the angular momentum of the electrons orbit around the nucleus, also has an impact on the binding energy. The electrons may transition between these states by either absorbing energy, or by emitting energy in the form of a photon[2]. In the nucleus each nucleon is attracted to each other by the strong nuclear force and all protons repels each other by the electromagnetic force. One way to describe the nucleus and the binding energy of each nucleon is with the liquid drop model [41].

[1] Weather or not the electron actually has a position when it isn't measured, depends on your interpretation of quantum Mechanics. This however, is not relevant for this thesis and will not be discussed further.

[2] Not all transitions are allowed, because there must be conservation of angular momentum [18]

3.1.1 Liquid Drop Model

The nuclear force does not interact simultaneously with all nucleons in the nucleus, like the electromagnetic force does with all charge, but it is instead inclined to binding pairs of neighbouring nucleons with opposite spins. So like a drop of water held together by surface tension and short range interactions, similarly a model for the nucleus can be made, that is described as such. This model gives a formula for the binding energy of the nucleus, meaning the energy needed to pull all nucleons infinitely far away from each other.
The first term in the binding energy takes into account that the nucleons only binds its neighbours, meaning that we can expect a positive term being proportional to the number of nucleons(A):

$$E_B = C_1 A \tag{2}$$

The second term is the surface tension term, that takes into account that the nucleons on the surface of the nucleus have less neighbours to bind with. We can therefore expect a negative term that is proportional to the surface area. The surface area is $4\pi R^2$ and $R \propto A^{1/3}$, so:

$$E_B = C_1 A - C_2 A^{2/3} \tag{3}$$

The third term is the protons repulsion and must be proportional to the electromagnetic force. Each proton repels the other protons, so with Z as the number of protons in the nucleus the term should be proportional to $Z(Z-1)$, and with the electrostatic potential being inversely proportional to the radius we get:

$$E_B = C_1 A - C_2 A^{2/3} - C_3 \frac{Z(Z-1)}{A^{1/3}} \tag{4}$$

The third term is the Asymmetry term that favours nucleus with equal amounts of protons and neutrons. This is because protons and neutrons are fermions(spin $\frac{1}{2}$) and must follow Pauli's exclusion principle, which states that 2 identical fermions cannot occupy the same quantum state. The nucleons will then fill up the lowest energy states(highest binding energy) first, and since neutrons and protons have different possible states, an excess of neutrons would fill more high energy states(low binding energy) so the binding energy pr. nucleon would be lower, compared to a nucleus with the same number of nucleons, but equal amounts of neutrons and protons see figure 1. The term should depend on $|A-2Z|$, but in a non linear fashion because a large deviation from equality should result in a penalty larger than the sum of its parts, so we choose $(A-2Z)^2$. We would also like the deviation from equality to mean less for nuclei with many nucleons, so we divide by A, and get:

$$E_B = C_1 A - C_2 A^{2/3} - C_3 \frac{Z(Z-1)}{A^{1/3}} - C_4 \frac{(A-2Z)^2}{A} \tag{5}$$

The nuclear force favours pairing of neutrons and protons, so we get a positive term when both, the number of protons and the number of neutrons are even, and a negative term when they both are odd. In the case where one is even and the other is odd we expect zero contribution, and the best fit comes from adding the following term: $\pm C_5 A^{-4/3}$, so the model becomes:

$$E_B = C_1 A - C_2 A^{2/3} - C_3 \frac{Z(Z-1)}{A^{1/3}} - C_4 \frac{(A-2Z)^2}{A} \pm C_5 A^{-4/3} \tag{6}$$

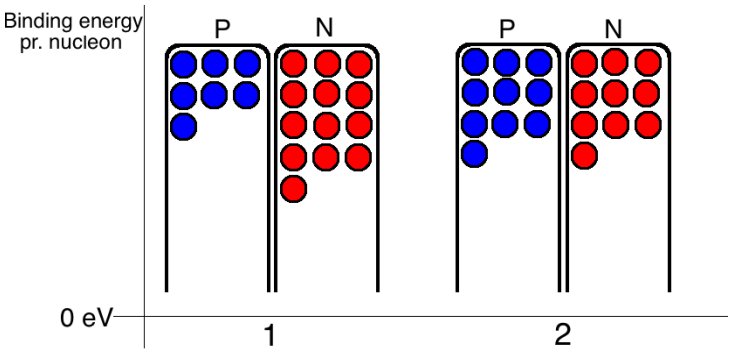

Figure 1: *This figure makes a rough illustration of the nucleon's energy states in 2 atomic nuclei: 1 and 2. Each nucleus has $A = 20$, with the blue spheres representing protons and the red spheres representing neutrons. On the y-axis is the binding energy pr. nucleon, that illustrates how the binding energy decreases, when more nucleons are added. By summing up the binding energy for 1 and 2, it is clear that nucleus number 2 has the highest total binding energy and thereby demonstrating the need for an asymmetry term in the liquid drop model.*

it is clear to see that some atoms have a higher binding energy than others, meaning they are more stably. In the same way that an object caught in a potential well would be "pulled" towards the center, would an atom seek to increase its binding energy any way it could. After any such transition the difference in binding energy is expelled as radiation in the ways described in the following subsections. Equation 6 can be fitted to the known binding energies as expected.

3.2 Types of Radiation

In this section we look at some of the different types of radiation that can occur.

3.2.1 Alpha Emission

If an atom has a low ratio of neutrons to protons it could be a candidate for α emission. for such an atom the protons repulsion will decrease the binding energy to the point where the quantum fluctuations of the nucleons could tunnel through the potential of the nuclear force. The nucleus is therefore unstable and will decay to a more stable daughter nucleus, by emitting an Helium nucleus(α particle) this would decrease the atomic number by 2, and the nucleon number by 4. An example of α decay is Radium-226:

$$^{226}_{88}\mathrm{Ra} \rightarrow {}^{222}_{86}\mathrm{Rn}^{*} + {}^{4}_{2}\mathrm{He} \tag{7}$$

The superscript $*$ means that the nucleus is in a excited state[3]. The decay must obey the mass and energy conservation laws:

$$M_p = M_d + M_\alpha + 2M_e + Q \tag{8}$$

Where M_p is the mass of the parent, M_d is the mass of the daughter, M_e is the mass of the electron, M_α is the mass of the α particle and Q is the mass associated with the kinetic energy and the energy of the excited states. The 2 electron masses comes from

[3]in the case of Radium-226, 5.7% of the α decays goes to Radon in an excited state.

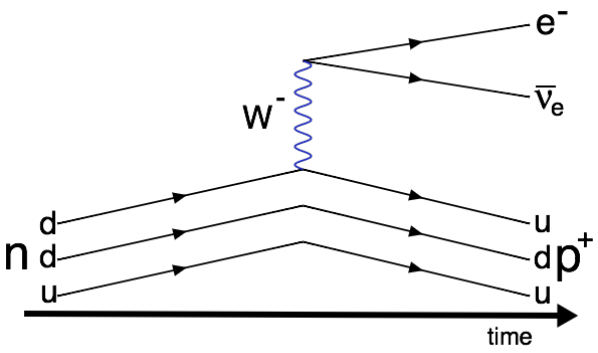

Figure 2: *This figure shows the Feynman diagram of β minus decay, where the negative down quark emits a W^- boson which decays into an electron and a anti-electron neutrino, the quark is now transformed into a positive up quark resulting in the transformation: $n \rightarrow p + e^- + \bar{\nu}_e$ a reverse transformation is also possible: $p \rightarrow n + e^+ + \nu_e$ this is called β plus decay.*

the orbital electrons that are lost when the atomic number decreases. The daughter and the α particle would both have a higher binding energy pr. nucleon, leaving an excess of energy that is Q in the above equation, this energy can be found as:

$$Q = M_p - M_d - M_\alpha - 2M_e \tag{9}$$

and ranges between 4 and 9 MeV, depending on the parent. Since the division of kinetic energy depends on conservation of momentum and energy, and the possible excited states are quantised, the energy of the α particle doesn't follow a continues spectrum but have certain discrete values unique to the parent nucleus.

3.2.2 Isobaric Transitions

Isobaric transitions are transitions in which the nucleon number of the parent and the daughter nucleus is the same. When the the neutron to proton ratio is too high, electroweak theory [20] enables the possibility of changing the negatively charged down quark($-\frac{1}{3}$) to the positively charged up quark($+\frac{2}{3}$) by emitting a electron and a anti-neutrino. It is therefore possible to transform a neutron into a proton: $n \rightarrow p + e^- + \bar{\nu}_e$ see figure 2. An example of β minus decay is the isotope carbon-14:

$$^{14}_{6}\mathrm{C} \rightarrow {}^{14}_{7}\mathrm{N}^* + e^- + \bar{\nu}_e \tag{10}$$

It is also possible to make the reverse transformation if the ratio of neutron to proton ration is too low and α emission is not energetically possibly or favourable. In that case a up quark transforms to a down quark while emitting a anti-electron and a neutrino: $p \rightarrow n + e^+ + \nu_e$ this is called β plus decay. The energy of β emission is quantised for the same reason as α emission, however this energy is divided between the anti-neutrino/neutrino and the electron/ anti-electron according to a spectrum. When undergoing β plus decay, the atomic number is decreased by one, and automatically lose an orbital electron in the process, so by mass and energy conservation we know that[4]

$$M_p = M_d + M_{-e} + M_{+e} + Q \tag{11}$$

Where $M_{\pm e}$ is the mass of the anti-electron/electron and Q is the mass associated with kinetic energy and the energy of the excited states. The equation above shows us that

[4]Since the electron-neutrinos mass is negligible small we will not include its mass term in the conservation equations

the parent must be at least 2 electron masses heavier, or else β plus decay cannot occur, for such a case the proton can absorb a orbital electron from the K-shell to make the following transformation: $e^- + p \rightarrow n + \nu_e$ this is called orbital electron capture or K capture. For K capture the conservation equation is:

$$M_p + M_e = M_d + \phi + Q \tag{12}$$

Where ϕ is the binding energy of the orbital electron. An example of K capture is:

$$^{40}_{19}\mathrm{K} + e^- \rightarrow ^{40}_{18}\mathrm{Ar}^* + \nu_e \tag{13}$$

3.2.3 Gamma Radiation

As shown in the two previous sections, sometimes after α decay, β decay or K capture the daughter nucleus is in an excited state. The nucleus will almost immediately after the transition decay to a more stable nucleus, thereby emitting a photon of high energy called a γ ray. The carbon-14 equation would then be:

$$^{14}_{6}\mathrm{C} \rightarrow ^{14}_{7}\mathrm{N}^* + e^- + \bar{\nu_e} \rightarrow ^{14}_{7}\mathrm{N} + \gamma + e^- + \bar{\nu_e} \tag{14}$$

The possible excited states of the nucleus are quantised and unique to the nucleus, so the energy of the γ rays give a signature, that can be used to determine radioactive compounds in a sample. In the case of β plus decay, an anti-electron is emitted, which after losing its kinetic energy by interacting with its surroundings, will hit a electron and annihilate transforming into two photons of total energy: $(M_{e^-} + M_{e^+})c^2 = 1022$ keV. Each photon has energy 511 keV and due to conservation of momentum is emitted in the opposite direction of the other:

$$e^+ + e^- \rightarrow \gamma + \gamma \tag{15}$$

These photons are as a general rule in health physics associated with γ radiation.
The isotope ^{60}Co is a γ emitter, which has two characteristic γ energies: 1.17 MV and 1.33 MV emitted in almost equal quantities, as 99.88 % of decays are

$$^{60}\mathrm{Co} \rightarrow ^{60}\mathrm{Ni}^{**} + e^- + \mu_e^- \rightarrow ^{60}\mathrm{Ni}^* + \gamma_{1.17} + e^- + \mu_e^- \rightarrow ^{60}\mathrm{Ni} + \gamma_{1.33} + \gamma_{1.17} + e^- + \mu_e^- \tag{16}$$

the almost mono-energetic γ spectra is one of the reasons that ^{60}Co is used as the reference beam quality in dosimetry.

3.2.4 Internal Conversion

The excited nucleus may also instead of emitting a γ ray, transfer its energy to a tightly bound electron, in the same way as an internal photoelectric effect. The energy of the "would be" γ ray is then the same as the kinetic energy of the electron minus the binding energy of the electron:

$$E_\gamma = \phi + E_e \tag{17}$$

This is called internal conversion.

3.3 Radiation Interacting with Matter

3.3.1 Cross Sections

When photons or charged particles travel through a medium, they can make different interactions, the probability of these interactions is described by their cross sections(σ) which has the unit Barns [$10^{-24}cm^2$]. Cross sections can classically be described as the area, pr. scattering target, a particle must hit for the interaction to happen. Therefore a small cross section means a small probability and vice versa. Mathematically we say that, if a particle has cross section σ for interacting with a target, and the particle is travelling in a medium with a density of targets(called target density) n, then the interaction rate, in $[\frac{number\ of\ interactions}{distance}]$ is σn. This means that if $N(x)$ is the number of, non-interacted, incident particles in a beam after travelling a distance x then:

$$N(x+\Delta x) = N(x) - \sigma n \Delta x N(x) \quad \Rightarrow \quad \frac{dN(x)}{dx} = -\sigma n N(x) \tag{18}$$

If we normalize $N(x)$, then according to the law of large numbers, we get the probability density function(PDF) for having not interacted after travelling a distance x:

$$p(x) = \frac{N(x)}{\int_0^\infty N(x')dx'} = \frac{1}{\sigma n} e^{-\sigma n x} \tag{19}$$

The right hand side of equation 19 is easily found from equation 18, and is the form of a Poisson process, which makes sense as the Poison distribution describes finite events(interactions) occurring in a continuum(distance), following a rate(σn) [7]. Yet as will be shown in the following sub-subsections, the incident particle will have multiple possible interactions, each with associated cross sections(σ_i) and targets(n_i), and the cross section is often dependent on the incident particles energy and medium composition. In a arbitrary environment, with the energy of the incident particles being distributed according to a energy spectrum($N_s(E)$), both the cross section and target density would depend on the position, and equation 18 becomes:

$$\frac{dN_s(\bar{r}, E)}{d\bar{r}} = -\sum_{i=1} \sigma_i(E, \bar{r}) n_i(\bar{r}) N_s(\bar{r}, E) \tag{20}$$

The fractional number of incident particles($\frac{N(\bar{r})}{N_0}$) is then found by integrating over the energy spectrum, and normalising:

$$\frac{N(\bar{r})}{N_0} = \frac{\int_0^{E_{max}} N_s(\bar{r}, E)dE}{\int_0^\infty \int_0^{E_{max}} N_s(\bar{r}, E)dEd\bar{r}} \tag{21}$$

After a scattering interaction there will often be a transfer of energy and change of direction, these are determined by the differential cross sections $\frac{d\sigma}{d\Omega}$, and $\frac{d\sigma}{dE_t}$, which act as scattering angle- and energy transfer probability distributions:

$$\sigma = \int_0^{4\pi} \frac{d\sigma}{d\Omega} d\Omega = \int_0^{E_{max}} \frac{d\sigma}{dE_t} dE_t \tag{22}$$

where Ω is the scattering solid angle(in spherical coordinates $d\Omega = \sin(\theta)d\phi d\theta$), E_t is the energy transferred during scattering, and E_{max} is the maximum energy transferred during scattering.

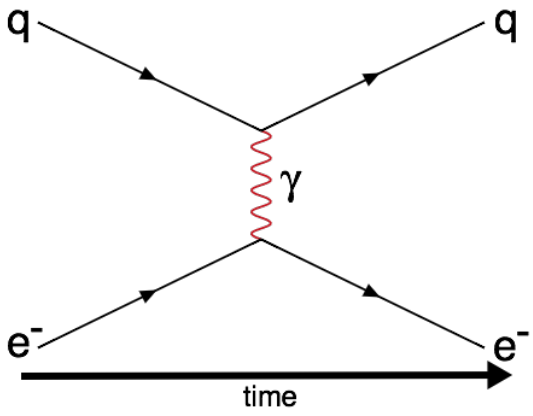

Figure 3: *This figure shows the Feynman diagram of an electric interaction between a quark and a electron as described by quantum electrodynamics. The same interaction is also possible with electrons and anti-electrons instead of quarks, and is the mechanism behind electronic excitation and electronic ionisation.*

3.3.2 Charged Particles

After either α decay, β minus decay, β plus decay or internal conversion, an charged particle is emitted with high kinetic energy e.g ${}^{4}_{2}\mathrm{He}^{++}$, e^- and e^+. When traversing through matter, the particle interacts with the medium in the following different ways:

- **Collisions:** The charged particle can interact electrically with the coulomb potential of the orbital electrons in medium, thereby transferring energy to them. When the incident particle is an electron, the interaction is called Møller scattering($e^-e^- \rightarrow e^-e^-$) and is described by the Møller cross section, and if the incident particle is an anti-electron the interaction is called Bhabha scattering($e^-e^+ \rightarrow e^-e^+$) and is described by the Bhabha cross section [20] [26] see Figure 3. If the energy transferred is less than the electrons binding energy, then the electron will be put in a excited state, this is called electronic excitation or soft collisions. If the transferred energy is more than the electrons binding energy then the electron is knocked free, and an ionisation pair, consisting of the free electron(knock on electron) and the positive ion, is made, this is called electronic ionisation or hard collisions. The freed electron will have kinetic energy $E_k = E_t - \phi$, where the transferred energy E_t is determined by $\frac{d\sigma}{dE}$ where σ is either the Bhabha or the Møller cross section. If E_k is higher than ~ 0.1 keV the electron will make it's own ionisation trail, these are called δ rays. Electrons can also scatter of the coulomb potential of the positive nucleus, this is called Mott scattering and very little energy is lost during these collisions.

- **Bremsstrahlung:** From classical electrodynamics we know that when charge is accelerated, electromagnetic waves are emitted with photon energy proportional to the square of the acceleration. As charged particles travels through a medium, many elastic interactions with the coulomb potential of the nucleus occur, where the charged particle changes its direction a small part and giving a little kinetic energy to conserve momentum(Mott scattering). In a minority of the cases, the interactions are inelastic, and part of the kinetic energy is lost to emitting a photon, see figure 4. This is called Bremsstrahlung/ *Breaking radiation*, and the photons emitted are called x-rays. The energy spectrum of x-rays depend on the medium, which is exploited when making an x-ray beam. In an x-ray emitters like the mega-voltage linear accelerators used for radiotherapy, electrons are fired towards a piece of metal called the "target". The target should have a high atomic number, as the fraction of

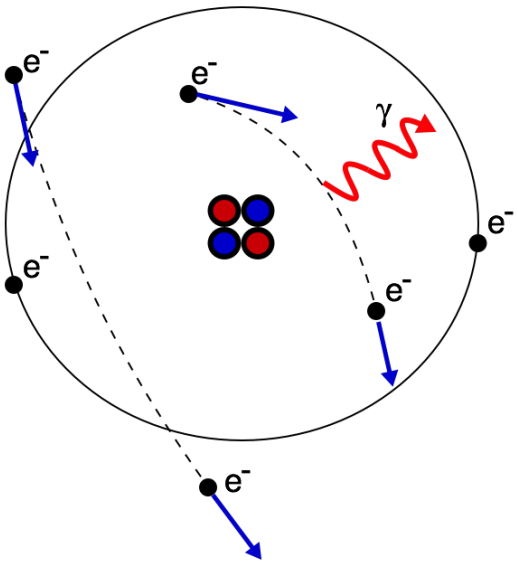

Figure 4: *This figure shows two free electrons scattering of the coulomb potential of* $^4_2$He *nucleus. One scatters inelastically and emits an x-ray, and the other scatters elastically suffering only a small change in momentum.*

energy that turns to x-rays increases linearly with atomic number of the target [13]

$$f_e = 1 \times 10^{-3} ZE \tag{23}$$

Tungsten is often used as target, even though other materials like lead have a higher atomic number, which is because tungsten have a very high melting point superior to other target candidates. The cross section is found by Bethe-Heitler theory

- **Cerenkov radiation:** When a charged particle travels through a dielectric material with a speed faster than the speed of light in that medium, electromagnetic waves are emitted as a cone following the charged particle. If the particle moved slower through the medium, then the disturbance in the electric field made by the particle would elastically even out the polarisation to equilibrium, however if the charged particle moves faster than the speed of light in the medium, then it would not be able to polarize fast enough to elastically even out the disturbance and would obtain an excited state which would emit photons when going back to equilibrium. Cerenkov radiation is what makes the characteristic blue glow found around a nuclear reactor core immersed in water. The threshold energy for a charged particle to emit Cerenkov radiation, is clearly when the speed is the same as the speed of light in the material: $v = \frac{c}{n}$ where n is the refractive index of the material, so the kinetic energy threshold is:

$$T_{cerenkov} = M_0 c^2 \left[\frac{1}{\sqrt{1 - \frac{v^2}{c^2}}} - 1 \right] = M_0 c^2 \left[\frac{1}{\sqrt{1 - \frac{1}{n^2}}} - 1 \right] \tag{24}$$

As an example the threshold for electrons/β-particles in water is 0.264 MeV and for α particles in water it is 1.9 GeV. Since naturally occurring α particles doesn't have energy even near that value, this is only relevant for electrons and anti-electrons, yet the energy loss due to Cherenkov radiation is insignificant compared to collisions and Bremsstrahlung [45].

So for heavy charged particles like the α particle, we need only take ionisation into account for finding the mean energy lost pr. distance travelled in the medium. To better compare results in radiation/medical physics, distance is replaced by a density independent distance called density thickness, by multiplying the distance by the density of the medium as such: 20 *cm in air at* 20 *celsius is* $20[cm] \times 1.2 \times 10^{-3}[g/cm^3] = 2.24 \times 10^{-2}[g/cm^2]$, the range of a particle travelling through a medium is therefore given in the units of g/cm^2. The mass stopping power of a medium is defined as the mean energy lost pr. density thickness: $-\left\langle \frac{dE}{dx} \right\rangle / \rho$ and for heavy charged particles in the energy range $0.1 \leq \beta\gamma \leq 1000$ the Bethe equation gives the colisional mass stopping power [35]

$$\left(\frac{S}{\rho}\right) = -\left\langle \frac{dE}{dx} \right\rangle / \rho = K \frac{z^2}{\rho} \frac{Z}{A} \frac{1}{\beta^2} \left[\frac{1}{2} \ln \frac{2m_e c^2 \beta^2 \gamma^2 T_{max}}{I^2} - \beta^2 - \frac{\delta(\beta\gamma)}{2} + \frac{C}{Z} \right] \tag{25}$$

Where T_{max} is the maximum kinetic energy that can be given to the bound electron during ionisation, I is the mean excitation potential for the medium, z is the charge of the incoming particle, β and γ are the relativistic quantities: $\beta = \frac{v}{c}$, $\gamma = \frac{1}{\sqrt{1-\beta^2}}$, δ is a density correction function, which corrects for the flattening of the electric field at relativistic speeds and C is a shell correction needed for non relativistic speeds that correct the assumption that the incoming particle moves faster than the orbital speed of electrons and $K = 4\pi N_A r_e^2 m_e^2 c^2$ with N_A as Avogadro's number and r_e as the classical electron radius. Electrons and anti-electrons differs from heavy particles in spin, charge, kinematics and in the case of electrons, there is the identical particles case, so the Bethe equation takes a different form:

$$\left(\frac{S^{\pm}_{col}}{\rho}\right) = -\left\langle \frac{dE}{dx} \right\rangle / \rho = \frac{1}{2} \frac{K}{\rho} \frac{Z}{A} \frac{1}{\beta^2} \left[\frac{1}{2} \ln \frac{m_e c^2 \beta^2 \gamma^2 T_{max}}{2I^2} + f^{\pm}(\gamma) - \delta(\gamma\beta) \right] \tag{26}$$

$$f^{-}(\gamma) = (1 - \beta^2) - \frac{2\gamma - 1}{\gamma^2} \ln 2 + \frac{1}{8} \left(\frac{\gamma - 1}{\gamma} \right)^2 \tag{27}$$

$$f^{+}(\gamma) = 2 \ln 2 - \frac{\beta^2}{12} \left(23 + \frac{14}{\gamma + 1} + \frac{10}{(\gamma + 1)^2} + \frac{4}{(\gamma + 1)^3} \right) \tag{28}$$

Where the superscript is $-$ for electrons and $+$ for positrons. T_{max} the maximum energy given to ionisation during a single collision is $T_{max} = 2m_e c^2 \gamma^2 \beta^2$ for electrons [35], this goes to zero for smaller and smaller energies, which show that in the process of slowing down, the electron performs a high number of collisions$(10^5 - 10^6)$. The total mass stopping power for electrons must also include contributions for Bremsstrahlung and cerenkov radiation:

$$\left(\frac{S_{Total}}{\rho}\right) = \left(\frac{S_{col}}{\rho}\right) + \left(\frac{S_{Xray}}{\rho}\right) + \left(\frac{S_{cerenkov}}{\rho}\right)$$

Mass stopping power data is shown for electrons in ^{82}Pb in figure 5. An close estimate of the mean range travelled by the charged particles is then found as:

$$R = \int_0^E \frac{1}{S_{Total}(E')} dE'$$

called the continues slowing down approximation range(CSDA range), which assumes the particles loses energy continuously by a rate given by the stopping power.

Figure 5: *This figure shows the mass stopping power of electrons travelling through* ^{82}Pb. *The collisional mass stopping power is* S_{col} *and the radiative is* $S_{Xray} + S_{cerenkov}$. *This data is found with ESTAR: stopping power and range tables for electrons.*

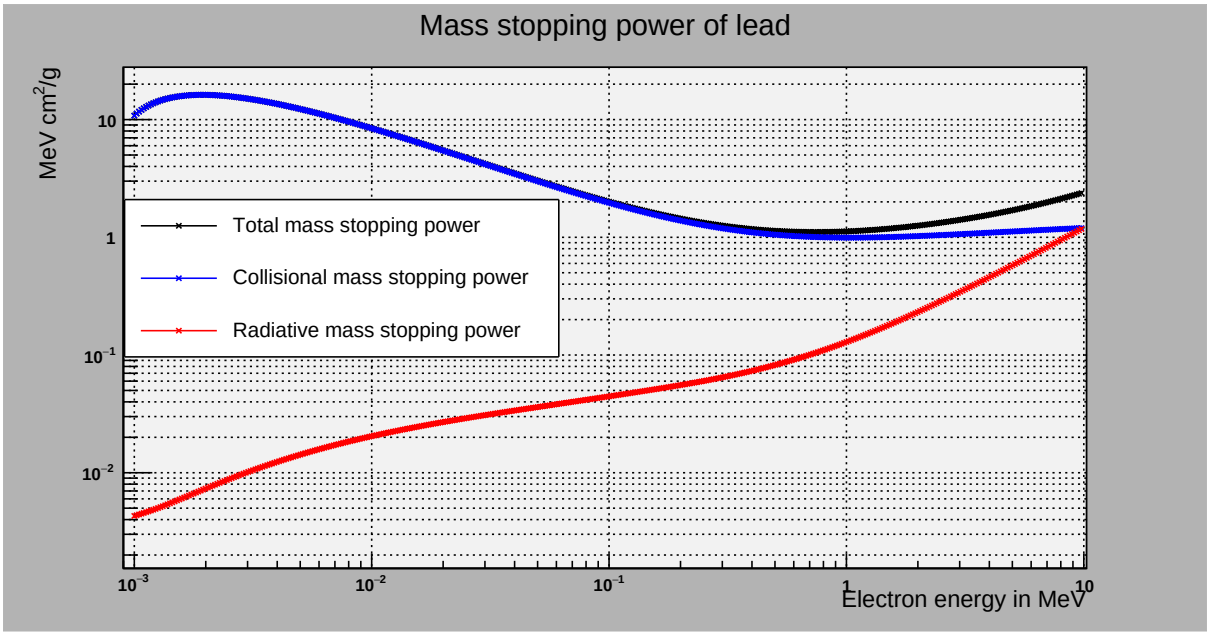

3.3.3 Photons

When high energy photons travel through a medium, they can make different interactions. These interactions are listed below.

- **Photoelectric Absorption:** In photoelectric absorption a incoming photon scatters with a bound electron, and all the photons energy is given to the target, which is then emitted with kinetic energy: $E_k = E_\gamma - \phi$. Photoelectric absorption is more probable for photons with energies near the binding energy of the electrons, which is why there are peaks for the K, L and M-shell binding energies in figure 6. The cross sections for photoelectric absorption is only calculated analytically for atomic number $Z = 1$, and is computed numerically for other materials [43], the cross section can however be approximated by [13]:

$$\sigma \propto \frac{Z^4}{E_\gamma^3} \tag{29}$$

  Where Z is the atomic number, and E_γ is the energy of the incident photon. For photoelectric absorption in ^{82}Pb, the cross section is shown in figure 6. After the electron leaves the atom a vacancy is left at its place, which is filled by atomic relaxation where one of the following three things happen:

  - An electron from an outer shell fills the vacancy, and thereby emits a photon with energy equal to the difference between the to electron states.
  - An electron from an outer shell fills the vacancy, and thereby knocks out an outer electron with energy equal to the difference between the two electron states. This is called an Auger electron.

– An electron from a different sub shell takes its place, and creates a new vacancy to be filled. This process is called Coster-Kronig.

Figure 6: *This figure shows the cross sections for non-coherent photon interactions in* ^{82}Pb*, for different energies. Notice that the peaks in Photo electric absorption coincide with the binding energy for electrons in* ^{82}Pb*, first peak from the right is the K-shell, second peak is the two orbitals(s,p) of the L-shell the third peak is the three orbitals(s,p,d) of the M-shell. This data was found with XCOM: photon cross section database*

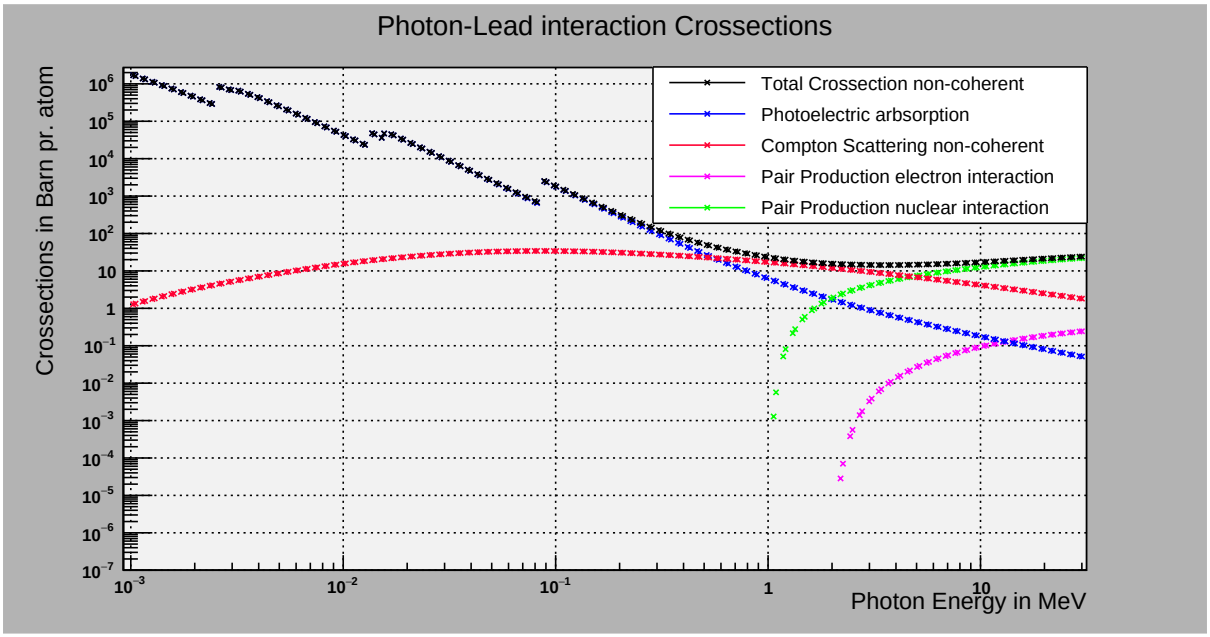

- **Compton Scattering:** Compton scattering is the elastic collision between a incoming photon and a electron, in which a transfer of momentum and kinetic energy is made, see figure 7. The photon gets scattered an angle θ from the scattered electron, which by energy and momentum conservation, can be found to have the following relationship:

$$\Delta\lambda = \lambda - \lambda' = \frac{\hbar}{m_e c}(1 - \cos\theta) \tag{30}$$

Where $\hbar$ is Plancks reduced constant, λ is the wavelength of the incoming photon and λ' is the wavelength of the outgoing photon. The cross section for Compton scattering is the Klein-Nishina cross section, who'es differential cross section is [20]:

$$\frac{d\sigma}{d\Omega} = \frac{\pi\alpha^2}{m_e^2}\left(\frac{\lambda}{\lambda'}\right)^2\left[\frac{\lambda}{\lambda'} + \frac{\lambda'}{\lambda} - \sin^2\theta\right] \tag{31}$$

Where λ and λ' is the wavelength of the incident and scattered photons, and α is the fine structure constant. Equation 31 describes the probability distribution for the solid angle of scattering, and together with equation 30 the energy of the scattered photon and electron is easily found. The total Klein-Nishina cross section in ^{82}Pb, is shown in figure 6.

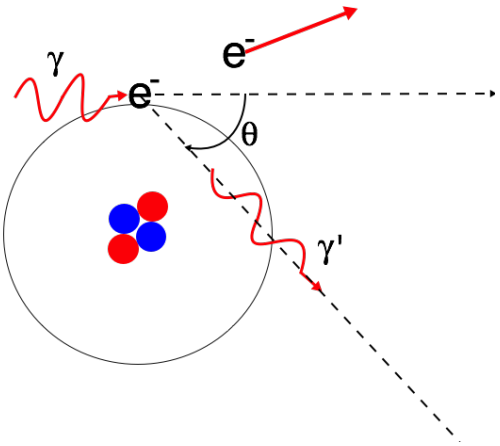

Figure 7: *This figure shows the schematic of compton scattering. An incoming photon γ scatters elastically with a electron, and transfers some of its energy. The outgoing photon travels now in a direction that deviates by the scattering angle θ*

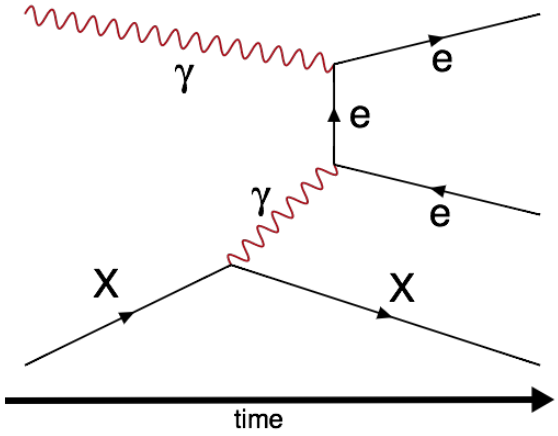

Figure 8: *This figure shows a feynman diagram of a pair production interaction. X is either an electron or a quark from a proton, which is needed for pair production to occur, see text. Observe the electrons charge is not added to the figure because the arrow of the fermion lines indicate whether the electron is regular or anti(In QED. anti-particles can be viewed as the regular particle travelling backwards in time.).*

- **Pair Production:** In pair production a photon transform into an electron and an anti-electron, by a conversion between energy and matter. Pair production is not possible in a vacuum, which can be easily explained to be kinematically forbidden: [20]
  Imagine one photon transforming into an electron and a anti-electron, then in the post-transformation center of mass frame the total momentum must be zero. In the same frame before the transformation, the total momentum is the momentum of the photon which is $\frac{E_\gamma}{c}$ for massless particles. The momentum, is therefore not conserved during the transformation and the photon must interact with an electric field from the medium as shown by the the feynman diagram in figure 8. The threshold energy for pair production can be calculated using conservation of energy and momentum, by imagining the photon γ moving along the z-direction and colliding with a particle of mass M in the particles rest frame, the energy conservation equation is then:

$$Mc^2 + E_\gamma = \sqrt{M^2c^4 + c^2p_M^2} + 2m_ec^2 \tag{32}$$

  Where we have used that for the threshold energy we can expect the produced particles to have zero kinetic energy. Due to the choice of the rest frame, we know the momentum conservation equation in the z-direction $p_\gamma = p_M = E_\gamma/c$, which together with equation 32, can be used to solve for E_γ finding the threshold energy

to be:

$$E_{min} = 2m_e c^2 \left(\frac{M - m_e}{M - 2m_e} \right) \approx 2m_e c^2 \left(1 + \frac{m_e}{M} \right) \tag{33}$$

Therefore if the mediating particle is the nucleus of an atom, m_e/M goes to zero and $E_{min} = 2m_e c^2 = 1.022$ MeV, where as for electron mediated pair production the threshold is $E_{min} = 4m_e c^2 = 2.044$ MeV. The electron and anti-electron will lose its kinetic energy as described in section 3.3.2, and the anti-electron will find a electron to annihilate with, emitting 2 photons of energy 511KeV. The cross section for nucleus mediated pair-production has the form $\sigma_{pp} = \alpha r_e^2 Z^2 P(E, Z)$, where α is the fine structure constant, r_e is the classical electron radius, Z is the atomic number and $P(E, Z)$ is a more complicated factor, described in more detail by Motz, Olsen and Koch [32]. For electron mediated pair production, the mediating electron is also released and is indistinguishable to the produced electron, and is therefore also called triplet production. The cross section for both pair and triplet production in ^{82}Pb, is shown in figure 6.

- **Rayleigh Scattering:** Rayleigh scattering or coherent scattering is an elastic interaction between the photon and a bound electron. Since nearly no energy is lost from the photon, and its direction only changes a small amount, it is not relevant in the calculation of absorbed dose in a medium but is however needed for the calculation of the attenuation coefficient, see the next section.

Figure 6 shows that photoelectric absorption is the dominating interaction for photon energies up to a few hundred KeV, Compton scattering then dominates till a few MeV, before pair production takes over. These dominating interaction intervals are unique to the medium, and differs for other materials, in the manner of the Compton scattering dominated domain decreasing for higher atomic number.

We know from section 3.3.1 that the number of un-interacted photons in a mono energetic photon beam is described by

$$N(x) = N(0)e^{-\sum_i \sigma_i n_i x} \tag{34}$$

In a radiation beam, the number of photons is high enough that $N(x)$ describes the attenuation of the beam, so we define the attenuation coefficient $\mu = \sum_i \sigma_i n_i$, which determines the exponential decrease of non-interacted beam: $I = I_0 e^{-\mu x}$. This makes it possible to determine the range of γ rays in various mediums for shielding purposes.
Since, for both Compton scattering and pair production, part of the energy is left as high energy photons, either as the Compton scattered photon(λ') or the two 521 keV photons from pair annihilation, we can define the energy absorption coefficient μ_{en} which describes the exponential loss of energy from the photon beam as $E = E_0 e^{-\mu_{en} x}$. μ_{en} is always smaller than μ and can be shown in comparison in figure 9.

3.4 Dose Kerma and Dosimetric Principles

In the process where energy from indirectly ionising radiation(photons or neutrons) is being absorbed by the medium, the energy must first be given to ionising particles(electrons

Figure 9: *This figure shows both the mass attenuation coefficient and the mass energy absorption coefficient for alanine. This data was found with NIST x-ray attenuation databases.*

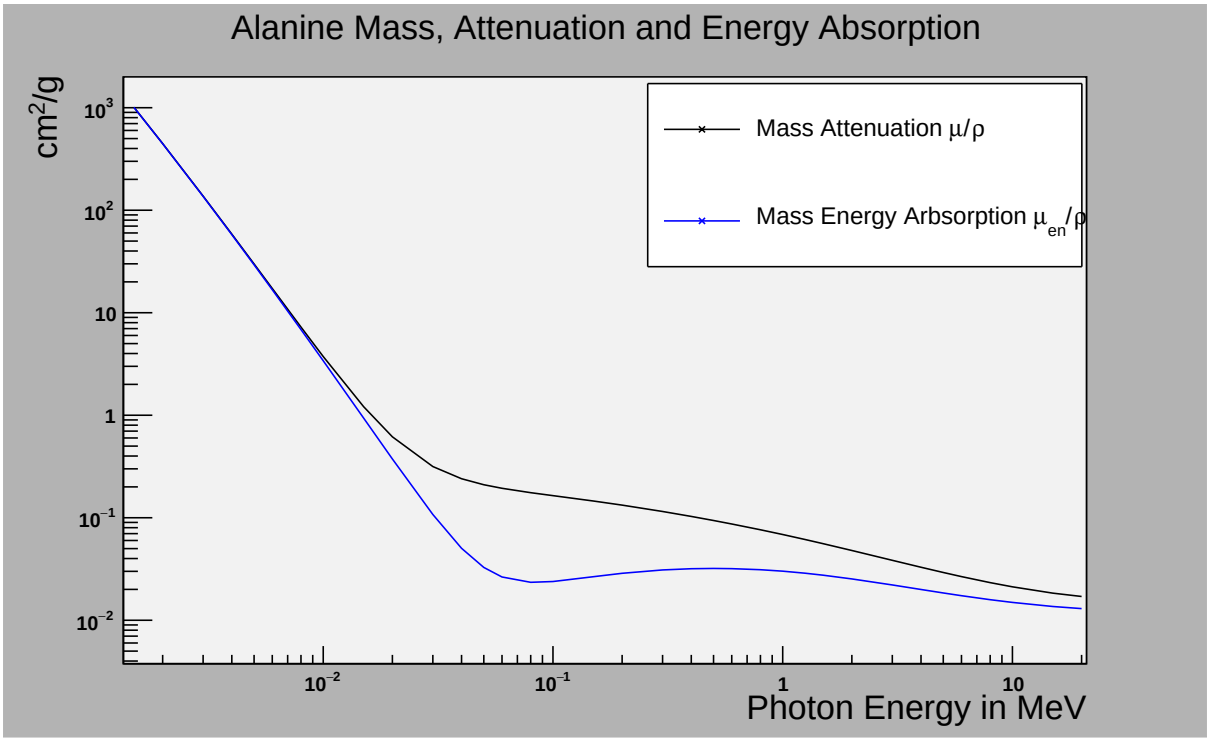

and anti-electrons), which transfers their energy along its path as described in section 3.3.2. This means that the energy loss described by μ_{en} isn't absorbed locally by the medium, but rather creates a shower of ionising particles. It is therefore relevant to define the quantity Kerma.

3.4.1 Kerma

Kerma is an acronym for kinetic energy released pr. unit mass, and has the units Gray$[J/cm^3]$, meaning the *sum of the initial kinetic energies pr. unit mass of all charged particles produced by the radiation* [13]. Kerma is the sum of collisional kerma K_{col}, the kinetic energy that will end up as ionisations in the medium, and radiative kerma K_{rad}, the kinetic energy that will end up as electromagnetic waves through Bremsstrahlung, pair annihilations and cherenkov radiation. We need to introduce a couple of quantities, to be able to describe Kerma mathematically.

The particle fluence $\Phi = \frac{dN}{dA}$ is the number of indirectly ionising particles incident on a sphere with cross sectional area A, and is therefore independent of the particles direction, e.g particles with opposite direction don't cancel out. The energy fluence $\Psi = \frac{dE}{dA}$ is the radiant energy incident on a sphere of cross sectional area A, so if E is the particle energy then $\Psi = \Phi E$. The absorption cross section μ_{en} is the fractional energy transformed to kinetic energy of charged particles, after travelling a small distance dx, so $\Psi\mu_{en} = \frac{dE_t}{dA}\frac{1}{dx} = \frac{dE_t}{dV}$ is the kinetic energy released in a small volume dV. We divide

by the density of the medium, and find the collisional Kerma[5]

$$K_{col} = \Psi \left(\frac{\mu_{en}}{\rho} \right) = \frac{dE_t}{dV} \frac{dV}{dm} = \frac{dE_t}{dm} \tag{35}$$

Equation 35 describes the kerma of a mono energetic beam of particles, and not a spectrum as expected in a real source. In the case of a spectrum we integrate over the energy of the incident particles [25]:

$$K_{col} = \int_0^{E_{max}} \Phi_E(E) E \left(\frac{\mu_{en}(E)}{\rho} \right) dE \tag{36}$$

3.4.2 Dose

Dose is the energy given to the medium through charged particle collisions pr. unit mass, and it has the unit Gray$[J/kg]$. Similar to the expression of the collisional kerma, we can write an expression for the absorbed dose given to a medium(med):

$$D_{med} = \int_0^{E_{max}} \Phi_{med,E}(E) \left(\frac{S_{col}(E)}{\rho} \right)_{med} dE \tag{37}$$

Where $\Phi_{med,E}(E)$ is charged particle fluence in the medium with energy E, and $\frac{S_{col}}{\rho}$ is the collisional mass stopping power as shown in section 3.3.2. If $\Phi_{med} = \int_0^{E_{max}} \Phi_{med,E}(E) dE$ is the total charged particle fluence in the medium, and

$$\left(\frac{\bar{S}_{col}}{\rho} \right)_{med} = \frac{1}{\Phi_{med}} \int_0^{E_{max}} \Phi_{med,E}(E) \left(\frac{S_{col}(E)}{\rho} \right)_{med} dE \tag{38}$$

equation 38 is the spectrum averaged mass stopping power, then equation 37 can be written as:

$$D_{med} = \Phi_{med} \left(\frac{\bar{S}_{col}}{\rho} \right)_{med} \tag{39}$$

When dose is given by indirectly ionising radiation, like photons, the intermediary step of kerma gives rise to a build-up region. When a photon beam passes from one material to another, e.g. air to water, the change in μ_{en} will course the kerma to change discontinuously as passing the boundary. The electron fluence Φ_{med}, however, will change continuously as ionising electrons in material 1 crosses the boundary to material 2, and giving a different Φ_{med} than should be expected from the local kerma, see figure 10. When the amount of electrons born from ionisations is equal to the amount absorbed by the medium we have charged particle equilibrium(CPE), when CPE is reached the build-up region ends, and the normal beam energy absorption continues. As seen in figure 10, there is a small deviation between kerma and absorbed dose in the non build-up region, this is due to the "delay" associated with the intermediary step of energy transfer. There is therefore not CPE, but transient charged particle equilibrium(TCPE) in the non build-up region.

[5]Equation 35 describes only the collisional kerma because the absorption coefficient doesn't include the kinetic energy that turns to secondary photons.

Figure 10: *This figure illustrates how the absorbed dose and kerma behaves in the build-up region. on the y-axis is log Gy, and on the x-axis is distance. The difference between kerma and absorbed dose in the non-build up zone is due to the intermediary step in the process of photon energy to charged particles to absorbed dose.*

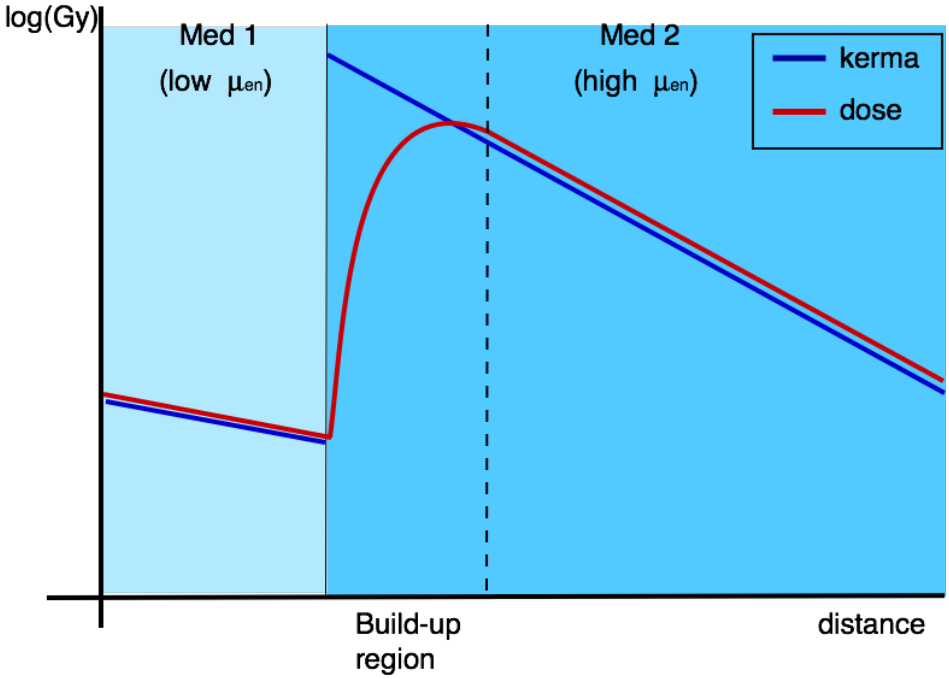

3.4.3 Cavity Theory

When we want to measure either dose or kerma in a radiated medium, we insert a dosimeter, which necessarily is made of a different material than the medium, so a perturbation of the TCPE is inevitable, and we need cavity theory to relate the absorbed dose in the cavity of the dosimeter, to the absorbed dose in the surrounding medium. In this thesis we will limit ourself to small cavities, which are cavities, where the range of the charged particles is much bigger than the dimensions of the cavity. In Bragg-Gray cavity theory we assume two conditions [25]

i The cavity is small enough, so it doesn't disturb the particle fluence.

ii The absorbed dose given to the cavity, is only from charged particles originating outside of the cavity.

If these two conditions are held, then the charged particle fluence would be the same, as if the cavity wasn't even there, and the only difference would be the mass stopping power in the cavity. So, using equation 39, the following relation can be made:

$$\Phi_{med} = \Phi_{cav} \quad \Leftrightarrow \quad \frac{D_{med}}{\left(\frac{\bar{S}_{col}}{\rho}\right)_{med}} = \frac{D_{cav}}{\left(\frac{\bar{S}_{col}}{\rho}\right)_{cav}} \quad \Leftrightarrow \quad D_{med} = D_{cav}\left(\frac{\bar{S}_{col}}{\rho}\right)_{med,cav} \tag{40}$$

Where the subscript of med, cav means its the ratio of med and cav. Bragg-Gray cavity theory does not take into account that some of the δ rays produced by hard collisions, will escape the cavity volume, and deposit the remainder of its kinetic energy outside the cavity, because the stopping power describes the energy lost from the charged particles, and not the energy absorbed by the medium. This is corrected for, with the Spencer-Attix cavity theory, where a kinetic energy cut off value Δ is chosen, for which a secondary electron, produced in the cavity, with kinetic energy higher than Δ, would most likely have the range to leave the cavity. The secondary electrons are then divided into two groups, where all secondary electrons produced which have $E_k < \Delta$ are viewed as locally absorbed energy, and all secondary electrons with $E_k > \Delta$ are called fast electrons, and are added to the electron fluence spectrum together with the incident charged particles($\Phi^{+\delta}_{med,E}$). The mass stopping power in Bragg-Gray cavity theory is then replaced by the restricted mass stopping power($\left(\frac{L_{col}}{\rho}\right)_{med}$), which is the mass stopping power for all soft collisions, and the hard collisions with energy transfers less than Δ. The Spencer-Attix relation is then written as:

$$\frac{D_{med}}{D_{cav}} = s_{med,cav} = \frac{\int_{\Delta}^{E_{k,max}} \Phi^{+\delta}_{med,E_k}(E_k) \left(\frac{L_{col}(E_k)}{\rho}\right)_{med} dE_k + \mathrm{TE}_{med}}{\int_{\Delta}^{E_{k,max}} \Phi^{+\delta}_{med,E_k}(E_k) \left(\frac{L_{col}(E_k)}{\rho}\right)_{cav} dE_k + \mathrm{TE}_{cav}} \tag{41}$$

Where the track end terms (TE) is the absorbed energy contribution from fast electrons, who's kinetic energy goes below Δ after collisional energy transfers. The track end terms can be approximated as [25]

$$\mathrm{TE}_{med} = \Phi^{+\delta}_{med,E}(\Delta) \left(\frac{S_{col}(\Delta)}{\rho}\right)_{med} \Delta \tag{42}$$

The integrals in equation 41, don't include absorbed dose given by incident charged particles with energy below Δ, this is because Δ is ideally chosen, so the amount of charged particles, with kinetic energy $< \Delta$, incident on the cavity, cancels out with the amount of charged particles, with kinetic energy $< \Delta$, who leaves the cavity. The Spencer-Attix restricted stopping power ratios($s_{med,cav}$) are found by Monte Carlo simulations of electron beams [16].

3.4.4 Absolute and Relative Dosimetry

A dosimeter is any device that can make a reading of the mean absorbed dose given to a measuring volume. In absolute dosimetry we use our theoretical models to calculate the conversion between the reading and the actual absorbed dose. For example, an ionisation chamber has a small cavity/measuring volume filled with air. The ionisation chamber works by collecting the charge from ion-pairs produced in the cavity, so the relation between collected charge and absorbed dose in the cavity is:

$$D_{air} = \frac{Q}{m} \frac{\bar{W}_{air}}{e} \tag{43}$$

Where $\bar{W}_{air}$ is the mean energy needed for producing one ion-pair in air, e is the elemental charge and m is the mass of the air in the cavity. Using Spencer-Attix cavity theory we

can find the conversion factor between D_{med} and the measured charge in the cavity(from here on after called M, for measurement.) [25]:

$$D_{med} = (M - M_0)N_{D_{med}} \quad \Rightarrow \quad N_{D_{med}} = \frac{\bar{W}_{air}}{e}\frac{s_{med,air}}{m}p_{\text{fl}}p_{\text{dis}}p_{\text{wall}}p_{\text{cel}} \tag{44}$$

Where all the p factors are correction factors needed to match the Ion chambers characteristics to the idealised cavity that meets the two conditions of Bragg-Gray cavity theory.

- p_{fl}: corrects for the perturbation of the electron fluence caused by the cavity. taken to be unity with uncertainty of $> 0.1\%$, for both ^{60}Co and MV-beams.

- p_{dis}: corrects for the displacement of the effective measurement point. We want the measurement M, to be associated with the center of the cavity, for a cylindrical ionisation chamber, however, the measurement M corresponds to a reading made slightly closer to the source. For a thimble chamber in ^{60}Co radiation, the correction factor can be found, with a 0.3% uncertainty, by $p_{\text{dis}} = 1 - 0.004r_{\text{cyl}}$, where r_{cyl} is the radius of the chamber in mm. For MV-beams the p_{dis} is found from irradiation experiments like [28]

- p_{wall}: corrects for the change in electron fluence, caused by the build up when passing the ionisation chamber walls. For cylindrical chambers with a wall of intermediate thickness, the correction factor is found with an uncertainty of 0.5% to be [25] [24]:

$$p_{\text{wall}} = \frac{\alpha s_{wall,air}\left(\frac{\mu_{en}}{\rho}\right)_{med,wall} + (1-\alpha)s_{med,air}}{s_{med,air}} \tag{45}$$

  Where α is the fraction of the absorbed dose given to the air cavity, which originated from electrons made in the wall, and is found by $\alpha = 1 - e^{-11.88t_{\text{wall}}}$, where t_{wall} is the wall density thickness(g/cm^2). When using MV-beams instead of ^{60}Co, equation 45 gives increase of maximum 0.2%.

- p_{cel}: corrects for the central electrodes lack of air equivalence, which for cylindrical chambers with an central electrode of 1 mm of aluminium in ^{60}Co radiation, increases the response by 7% with a 0.2% uncertainty. When using MV-beams there is a linear increase in the response from 0.43% to 0.75%, for $\text{TPR}_{20,10}$ between 0.80 to 0.58 [24], see section 5.1 for a description of $\text{TPR}_{20,10}$.

Therefore when calculating $N_{D,med,Q}$ for a dosimeter, where Q represents the type of radiation or beam quality(see section 5.1 for a description of beam quality), it is possible to determine the dose-rate in a medium brought to by a source Q. Once the dose-rate is determined, it can be used to calibrate other dosimeters, by taking a reading at the know dose-rate, and calculating the ratio $\frac{D_{med,Q}}{M_Q} = N_{D,med,Q}$. This is called relative dosimetry, as the calibration is traceable to the uncertainty of the dose-rate found by absolute dosimetry. In relative dosimetry the traceability only holds for irradiations, in which the details of the set up, is identical the set up of the calibration, called reference conditions. Any deviation from the reference conditions must be corrected for using correction factors

k_i, see section 5.1 for a description of Farmer chamber correction factors.

For better comparons of dose measurements made by different dosimetry laboratories in different mediums with different sources and so fourth, dose measurements are presented as absorped dose to water(D_W), and are traceable to a primary standard. A primary standard is a dose-rate measurement which is so accurate that it is used to reference dose measurements. They are often made using a graphite calorimeter to measure the dose-rate of a ^{60}Co source which is done at a primary standard dosimetry laboratory(PSDL). The national physics laboratory of the UK(NPL), and The Physikalisch-Technische Bundesanstalt(PTB) are two examples of PSDL. Dosimeters are then calibrated at PSDL's before being used in a secondary standard dosimetry laboratories(SSDL) for dosimetry purposes. Comparisons between primary standards of different PSDL, is done by key comparison values [42].

3.5 Statistics

3.5.1 Statistical Formalism

The uncertainties and errors in this thesis follows the definitions of [24], in which the error is the difference between measured value and the true value, so if we knew the error, then we would know the true value. Uncertainty is a measure of our lack of knowledge, often quantised by the standard deviation of the normal distribution. Uncertainties are classified into two groups: A and B. Type A uncertainties are those which are found through statistical analysis of repeated measurements, e.g the standard deviation of the mean after N measurement:

$$\sigma(\bar{x}) = \sqrt{\frac{1}{N}\frac{\sum_{i=1}^{N}(\bar{x} - x_i)^2}{N-1}} \tag{46}$$

Type B uncertainties are those gained from any other method which is not statistical analysis of repeated measurements, some examples are:

- When we use our knowledge of a system to apply and uncertainty following some distribution e.g. a triangular distribution, normal distribution or a uniform rectangular distribution.
- When uncertainties are quoted from other experiments, or calibrations.

Type A and B uncertainties can be added together in quadrature:

$$\sigma = \sqrt{\sigma_A^2 + \sigma_B^2} \tag{47}$$

If some quantity(f) depends on multiple values(x_i), each having their own uncertainty(σ_i), then the the uncertainty on f can be found using error propagation [7]:

$$\sigma_f = \sqrt{\sum_{i=1} \left(\frac{\partial}{\partial x_i} f(x_1, x_2 \dots)\right)^2 \sigma_i^2} \tag{48}$$

Error propagation works only for uncertainties following the normal distribution, so great care is needed when using type B uncertainties.
If we want to test if two measurements could be of the same value, we would test if their deviation was significant compared to their uncertainties, by calculating how many standard deviations they deviate:

$$z = \frac{|x_1 - x_2|}{\sqrt{\sigma_1^2 + \sigma_2^2}} \tag{49}$$

Then we integrate over the normal distribution:

$$P(> z) = 2 \int_z^\infty \frac{1}{\sqrt{2\pi}} e^{-\frac{x^2}{2}} dx \tag{50}$$

which is the probability of obtaining these, or worse, measurements if they indeed were of the same value, e.g. $P(> 1\sigma) = 31.7\%$, and $P(> 2\sigma) = 4.6\%$. z is often called the significance. All uncertainties stated in this thesis are 1 sigma(coverage factor $k = 1$) unless specifically stated otherwise.

3.5.2 χ^2 Distribution

When wanting to determine if some data points(y_i) fit some theoretical prediction($f(x)$), one can use the χ^2 method, where the following quantity is calculated: [7].

$$\chi^2 = \sum_{i=1} z_i^2 = \sum_{i=1} \frac{[y_i - f(x_1)]^2}{\sigma_i^2} \tag{51}$$

Where $\sigma_i = \sqrt{\sigma_{y_i}^2 + \sigma_{f(x_i)}^2}$ is the expected uncertainty between data point and prediction. The χ^2 quantity is proportional to the squared difference, and inversely proportional to the squared uncertainty, which makes it sensitive to large deviations, compared to the uncertainty. The χ^2 method is therefore also ideal to determine if a data fit is good or bad, which is done by calculating the probability of obtaining the found χ^2 or higher(worse results), if we assume that the prediction is correct. E.g if we obtain a value χ^2 then we integrating the χ^2 probability density function:

$$p = \int_{\chi^2}^\infty P(x, n) dx = \int_{\chi^2}^\infty \frac{2^{-n/2}}{\Gamma(n/2)} x^{n/2-1} e^{-x/2} dx \tag{52}$$

Where Γ is the gamma function, and n is the number of degrees of freedom, which in the cases of this thesis is the number of data points minus the parameters of the fit parameters of $f(x)$. Then the fit/model is rejected if p is less than some chosen rejection value, often 0.05, meaning that the fit is a bad fit if there is a $< 5\%$ chance of sampling the found value of χ^2. A rule of thumb is that we want χ^2/n to be close to 1, but if $\chi^2/n < 1$, then we probable overestimated the uncertainties, and other methods should be used.

3.5.3 Runs Test

If $\chi^2/n < 1$ then it is quiet possible that the uncertainties are overestimated, in that case we can perform the Runs test [7]. In the Runs test we exploit that in a perfect model($f(x)$) for some data points(y_i), we'd expect roughly half of the data to have a value higher than the model(A) and rest to be lower than the model value(B), the sequence in which they are arranged in higher and lower(e.g $AABABAAB...$) should follow the binomial distribution, for the possible ways you can arrange a sequence of N_A A's and N_B B's. Defining a run as every time the sequence changes between A and B(e.g $AAABBA$ has three runs, and $ABBABAAAB$ has 6 runs.), it can be found from the binomial distribution that the mean number of runs are:

$$\langle r \rangle = 1 + \frac{2N_A N_B}{N} \tag{53}$$

Where $N = N_A + N_B$. with the variance:

$$V_r = \frac{2N_A N_B(2N_A N_B - N)}{N^2(N-1)} \tag{54}$$

Once r, $\langle r \rangle$, and V_r are found, we can calculate the number of standard deviations we deviate from $\langle r \rangle$, as $z = \frac{|\langle r \rangle - r|}{\sqrt{V_r}}$. This is used to try and reject the model, using equation 50.

4 Alanine-EPR Dosimetry

4.1 Magnetic Moment

When a current I moves around an infinitesimal loop of area $|\bar{dA}|$, a magnetic moment is given as:

$$\bar{d\mu} = I\bar{dA} \tag{55}$$

Where the direction is the normal of the infinitesimal loop area. When the current goes around a loop of finite size, we can divide the finite loop up into many small infinitesimal loops and sum up the $\bar{d\mu}$ of equation 55, which can be done because the current of neighbouring $\bar{dA}$ all cancel out leaving only the current going around the full loop:

$$\bar{\mu} = I \int \bar{dA} \tag{56}$$

Therefore, in the case of a single charged particle moving in a loop, the current is proportional to the angular momentum($\bar{L}$) and a gyromagnetic ratio(γ) can be defined by $\bar{\mu} = \gamma \bar{L}$. In the atom, we have multiple potential sources of magnetic moments: the electrons orbital angular momentum(L), the electrons intrinsic spin(S), and the protons intrinsic spin(S_N), which all have singular charged particles with angular momentum, their gyromagnetic ratio is given [10].

$$\gamma_L = \mu_B = \frac{e\hbar}{2m_e}, \quad \gamma_S = g\mu_B, \quad \gamma_N = \mu_N = \frac{e\hbar}{2m_p} \tag{57}$$

Where μ_B is called the Bohr magneton, and $g \cong 2$ is known as the g-factor. The electron is a spin $\frac{1}{2}$ particle, meaning that the angular momentum along any direction(z), will have one of two possible values: $\hat{S}_z |\uparrow\rangle = \frac{\hbar}{2}$, $\hat{S}_z |\downarrow\rangle = -\frac{\hbar}{2}$. The magnetic moment contribution of electron spin is $\mu = \pm g\mu_B \frac{\hbar}{2}$. If we apply a external magnetic field($\bar{B}$) to a magnetic moment, then a torque($\bar{\tau}$) on the magnetic moment is given, which depend on the direction of $\bar{B}$ and $\bar{\mu}$:

$$\bar{\tau} = \frac{d\bar{L}}{dt} = \bar{\mu} \times \bar{B}, \quad \Leftrightarrow \quad \frac{d\bar{\mu}}{dt} = \gamma \bar{\mu} \times \bar{B} \tag{58}$$

With energy $E = -\bar{\mu} \cdot \bar{B}$. So the magnetic moment will precess around the direction of $\bar{B}$, with constant angle between the two vectors. For electron spin in a magnetic field, the binding energy is:

$$E = E_0 - \bar{\mu} \cdot \bar{B} = E_0 \pm g\mu_B \hat{S}_z B_z = E_0 \pm g\mu_B \frac{\hbar}{2} B_z \tag{59}$$

Where B_z is the component of the external magnetic field in the direction of $\hat{S}_z$. This splitting of energy levels in a magnetic field is called the Zeeman effect, and with the absorption/emission of photons with energy $g\mu_B \hbar B_z$, it is possible for the electron to change it's spin state.

4.2 Alanine and Free Radicals

If a molecule has an even number of electrons, then the spins would be paired up, so each orbital contained one spin up electron, and one spin down electron. Such a molecule would leave only a negligible[6] excess magnetic moment, and is called diamagnetic. As explained in previous sections, radiation can knock electrons off the molecules in the medium, thereby leaving molecules with unpaired electrons, which are called free radicals. Free radicals would in most cases quickly either react with the surroundings, or absorb a new electron giving the free radical a short lifetime. But for some crystalline compounds they could have a lifetime of multiple years. One such compound is crystalline alanine, which have a free radical lifetime of many years [40]. Alanine is an amino acid, the type used for dosimetry is L-α alanine which has the molecular structure:

$$\mathrm{CH_3} - \mathrm{CH(NH_2)} - \mathrm{COOH} \tag{60}$$

The most common free radical created at room temperature during irradiation is [40]:

$$\mathrm{CH_3} - \dot{\mathrm{C}}\mathrm{H} - \mathrm{COOH} \tag{61}$$

In alanine dosimetry crystalline L-α alanine is often mixed with some binding material and shaped into small pellets(alanine dosimeters). The pellets used for this thesis was made with paraffin wax as the binding material. The hypothesis of alanine-EPR dosimetry

[6]negligible for the purpose of EPR at least. In Nuclear Magnetic Resonance(NMR) the coupling between nuclear spin, orbital angular momentum, and electron spin is non negligible.

is as follows: the absorbed dose to alanine, must be proportional to the number of free radicals produced by the radiation. And the free radicals have unpaired electrons, which can be measured with electron paramagnetic resonance spectroscopy, also called electron spin resonance spectroscopy.

4.3 EPR

In EPR the alanine sample is placed in the bottom of a small quartz tube, which is placed in a metal cavity placed in the center of a Helmholtz coil. Next to the cavity, there is located a microwave emitter, that emits microwaves of fixed wave length into the cavity, and a photosensitive detector, which can measure the microwaves that are reflected back[7]. A magnetic field(B) is applied to the sample with the Helmholtz coil, which splits the energy values of the free radicals unpaired electrons spin states. The magnetic field is varied in the vicinity of the energy splitting, for which the difference between spin up and down is the microwave photon energy. This will cause stimulated emission and stimulated absorption because the microwaves are polarised, so the oscillating magnetic field is perpendicular to B_z when the energy splitting matches the photon energy. But the rates for stimulated emission and absorption are the same, so what can we expect to measure with the photosensitive detector when varying the magnetic field? To answer this, we must first know which spin states are occupied.
We know from the Maxwell-Boltzman law, that the ratio of occupied high($\uparrow$)/low($\downarrow$) energy spin states is

$$\frac{n_\uparrow}{n_\downarrow} = e^{-\frac{\Delta E}{kT}} \tag{62}$$

Where ΔE is the binding energy differences between the spin up and down states in a single unpaired electron, k is Boltzman's constant, and T is the temperature in Kelvin. So for $\Delta E > 0$, we have that $\frac{n_\uparrow}{n_\downarrow} < 1$, meaning that the unpaired electrons occupy more $\downarrow$ states than up states. The detector should therefore measure increased photon absorption when the photon energy matches $g\mu_B\hbar B_z$. A sample reading will give a spectrum with the signal on the y-axis and the varied magnetic field on the x-axis, see figure 11. The signal is not given as measure microwaves collected at the current magnetic field, but instead as the change in the collected microwaves as a function of the changing magnetic field $\frac{\partial S}{\partial B_z}$ called absorption response. As the spectrum shows the first derivative, the two peaks of red color in figure 11, indicate a peak in absorption for B_z somewhere around 3397 G, which is when the photon energy matches $g\mu_B\hbar B_z$. Other absorption peaks, not visible in figure 11, also appears next to the one in figure 11, they come from other possible energy state transitions, explained originating from hyperfine interactions with the four adjacent carbon atoms [31]. For the free radicals to stabilise, the irradiated alanine dosimeters shouldn't be readout before at least after 24 hours after irradiation [33].

[7]These are called reflection spectrometers, but there exists also models which detect the photons transmitted through the sample, these are called transmission spectrometers. The EMX Bruker of this thesis is however a reflection spectrometer

Figure 11: *This figure shows the spectrum from a EPR readout of a alanine dosimeter irradiated with 100 Gy. On the x-axis is the magnetic field strength B_z in Gauss, and on the y-axis is the absorption response $\frac{\partial S}{\partial B_z}$ in arbitrary units.*

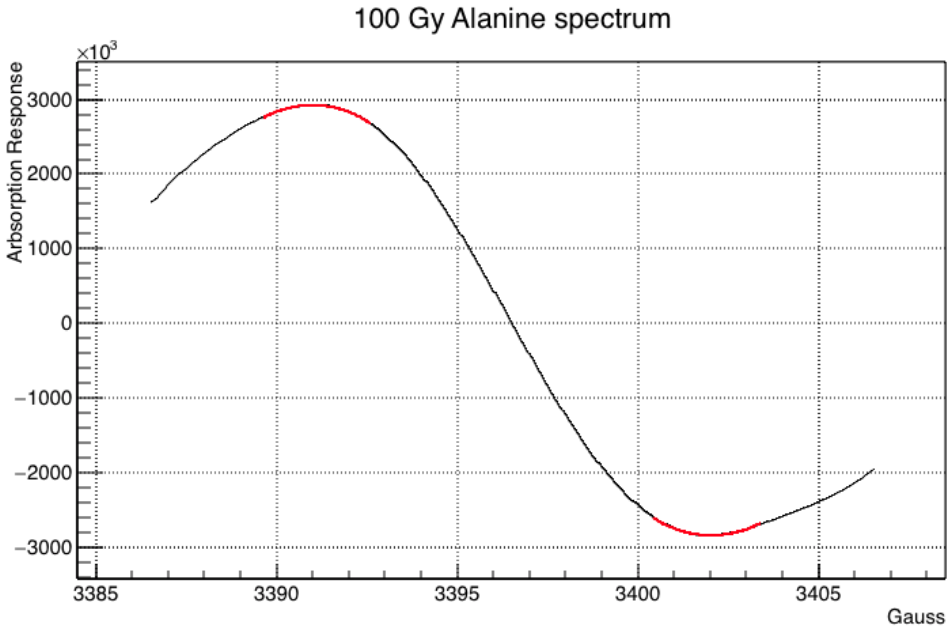

4.4 Spectrum Analysis

The height of the two absorption response peaks, would depend on the sharpness of the absorption peak, which would depend on the amount of free radicals, which is proportional to the absorbed dose given to the alanine dosimeter. It turns out that the difference in absorption response between the two peaks shown in figure 11, is proportional to the absorbed dose for doses between a few Gy and 100 kGy [40], for doses higher than 100 kGy the dependence is a little more complicated, and for doses below a few Gy the noise to signal ratio becomes very high. This distance is called the peak to peak amplitude. The algorithm used in this thesis for determining the absorbed dose given to a alanine dosimeter from it's EPR spectrum is described on the following pages.

We need an averaged background spectrum(A_0), made from readouts of un-irradiated alanine dosimeters, see figure 12, An EPR-spectrum from an alanine dosimeter with known dose(A_{ref}), and lastly the spectrum we want to investigate(A).

1. All spectra are weighted according to their dosimeters mass, as the number of free radicals is proportional to the mass.

2. A and A_{ref} are subtracted A_0, in an attempt to isolate the signal from the radiation induced free radicals. they are now denoted A_B and $A_{B,ref}$

3. The peak to peak amplitude(P2P) is found for both A_B and $A_{B,ref}$ by fitting a symmetrical fourth degree polynomials(f) in the vicinity of each peak:

$$f(B_z) = p_1 + p_2(B_z - p_0)^2 + p_3(B_z - p_0)^4 \tag{63}$$

   P2P is then found as $\Delta f(p_0)$ for the two fits.

Figure 12: *This figure shows the average EPR spectrum from a EPR readout of 10 un-irradiated alanine dosimeters. the error bars shown are the standard deviation of equation 46*

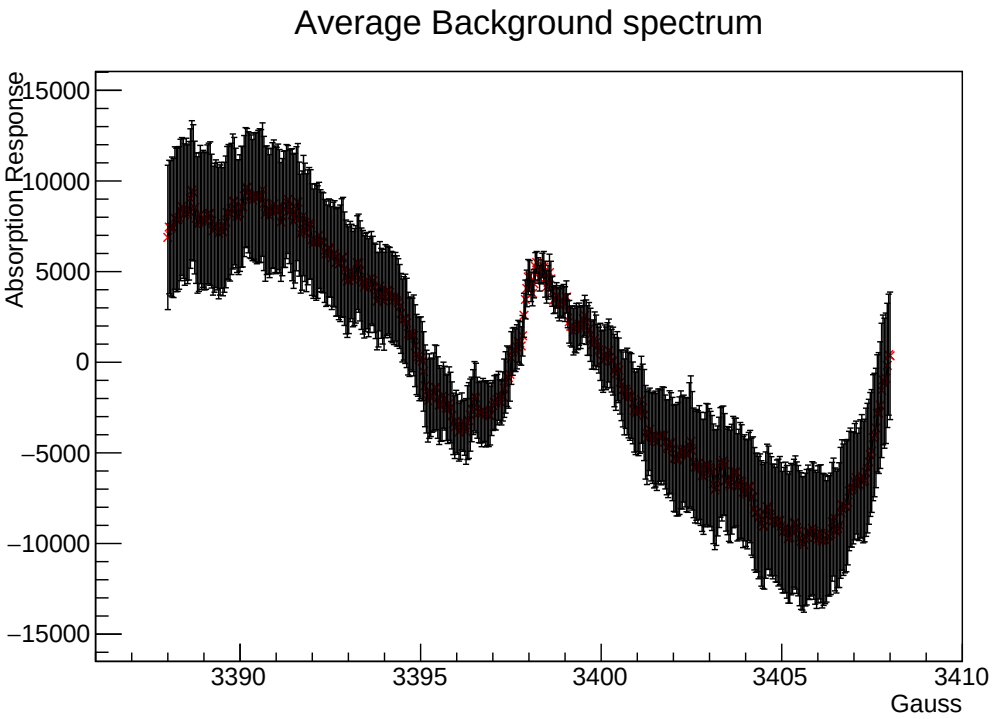

4. $A_{B,ref}$ is often of high dose, and will have a low noise to signal ratio relative to A_B, so in this step we scale down $A_{B,ref}$ to the size of A_b with the factor $\frac{\text{P2P}}{\text{P2P}_{ref}}$, fit a fourth degree polynomial to the deference and subtract it from A as such:

$$A'_B = A_B - \left(\frac{\text{P2P}}{\text{P2P}_{ref}} A_{B,ref} - A_B \right)_{f_4} \tag{64}$$

Where the subscript f_4 means we fitted it with a fourth degree polynomial. This will remove trends that makes the shape of A_B deviate from the shape $A_{B,ref}$, remember we assume that $A_{B,ref}$ has less noise, and therefore the more correct shape of a noiseless spectrum. Before we find $\frac{\text{P2P}}{\text{P2P}_{ref}} A_{B,ref} - A_B$, we move $\frac{\text{P2P}}{\text{P2P}_{ref}} A_{B,ref}$ along the x-axis(magnetic field axis) by the amount δ, to the point where the squared distance between the spectra is at a minimum:

$$\delta \in \min \left[\sum_{i=1} \left(\frac{\text{P2P}}{\text{P2P}_{ref}} A_{B,ref}(B_{z,i} + \delta) - A_B(B_{z,i}) \right)^2 \right]$$

Where the $\sum_i$ is over all data points in the spectra. This should diminish some of the errors associated with offsets on the magnetic field, either caused by drifts in the tuning, or temperature differences. An example of $\left(\frac{\text{P2P}}{\text{P2P}_{ref}} A_{B,ref} - A_B \right)_{f_4}$ can be seen in figure 13.

5. Step 2 and 3 are repeated till $A'_B \simeq A_B$. 2 or 3 iterations is usually enough.

Figure 13: *This figure shows a fourth degree polynomial fit of A_B subtracted by the scaled down $A_{B,ref}$*

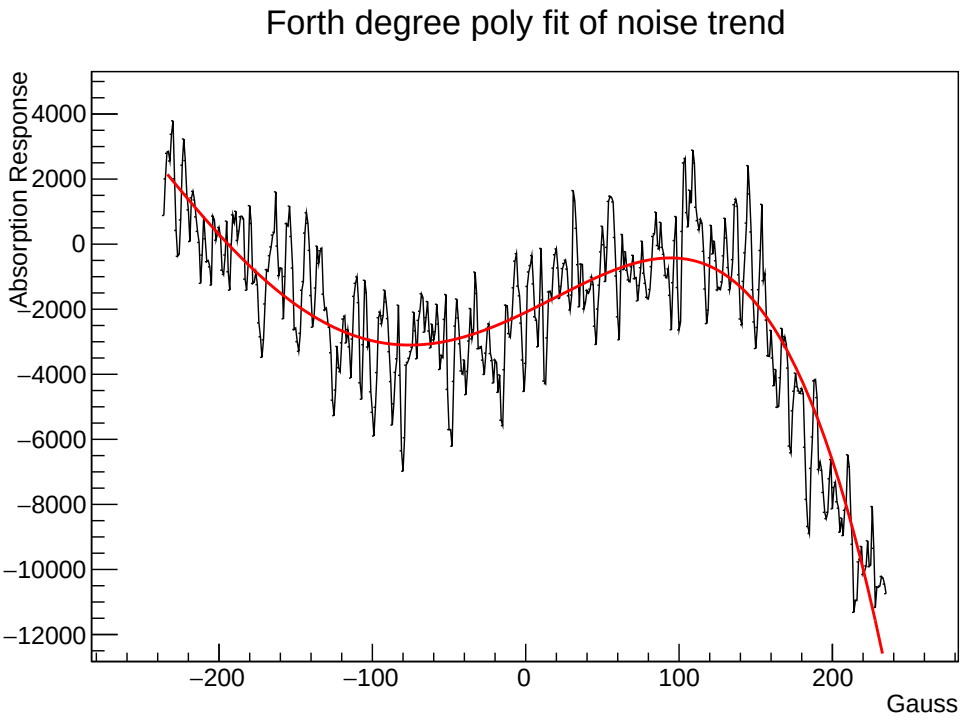

6. The dose is then given as f_{cal}^{-1}(P2P'), where f is one of the calibration curves of figure 22 and 21.

The signal creation of free radicals depend on the temperature as +0.14% pr. degree Celsius [22]. Time for the alanine temperature to acclimate to the phantom temperature is therefore needed before irradiation to know the temperature.

To reduce some of the day to day stability between the day the calibration was made, and the day that A is readout, A_{ref} should be re-readout in the same sitting as the A. The calibration curve is then scaled by the ratio of P2P_{ref} of the new and the old readout.

4.5 Energy Dependence

The photon energy dependence for alanine has been studied many times [44] [40] [48] [9] [50] [4] [5]. Using the notation of Waldeland et. al. [48], the measured dose to water energy dependence is described by:

$$F_{Q,Q_0} = \frac{(M/D_W)_Q}{(M/D_W)_{Q_0}} = \frac{(M/D_{dos})_Q}{(M/D_{dos})_{Q_0}} \cdot \frac{(D_{dos}/D_W)_Q}{(D_{dos}/D_W)_{Q_0}} = G_{Q,Q_0} \cdot H_{Q,Q_0} \tag{65}$$

Where $(M/D_W)_Q$ is the dosimeter reading pr dose to water for beam quality Q, in the notation of this thesis M = P2P. Too better understand what the factors F, G, and H are, we introduce the "big dosimetric picture", where we split up the workings of a dosimeter up into three steps, to better analyse the reasons for energy dependence:

- **Energy Absorption**: We know that the restricted mass stopping power of Spencer-Attix cavity theory depends on the photon energy, so some degree of energy dependence is expected from this step. The quantity of interest would be the ratio of absorbed dose for two different beam qualities $\frac{D_{dos,Q}}{D_{dos,Q_0}}$, where Q_0 is used as a reference beam quality, chosen to be ^{60}Co. We want to make a correction factor that corrects for the energy dependence in the energy absorption step, so it not only corrects for $D_{dos,Q}$ but also converts correctly to D_{W,Q_0}. So the energy absorption correction factor(k_{ea}) should be defined as:

$$\left(\frac{D_W}{D_{dos}}\right)_{Q_0} = k_{ea}\left(\frac{D_W}{D_{dos}}\right)_{Q} \tag{66}$$

  Notice that $k_{ea} = (H_{Q,Q_0})^{-1}$, and that it doesn't depend on the dosimeter readings but only known absorbed doses. H_{Q,Q_0} should therefore be found either through cavity theory calculations, or Monte Carlo simulations as is done in this thesis.

- **Signal Creation**: When free radicals are created during irradiation, electrons are knocked free from the molecules of alanine, which can only happen with hard collisions. So if the fraction of energy absorbed through soft collisions is dependent on the photon energy, we can also expect energy dependence in the signal creation. The quantity of interest would be the radiation yield in free radicals pr. absorbed dose $\frac{F_radical}{D_{dos}}$. The only way to make a measure of the free radicals is through EPR readout, so assuming there is no energy dependence in signal creation(see below) the correction factor for energy dependence in signal creation(k_{sc}) is the ratio of radiation yields for Q and Q_0:

$$k_{sc} = \frac{(M/D_{dos})_{Q_0}}{(M/D_{dos})_{Q}} \tag{67}$$

  Notice that $k_{sc} = (G_{Q,Q_0})^{-1}$. G_{Q,Q_0} is called the relative effectiveness or relative efficiency depending on the author [48] [4].

- **Signal Detection**: Does EPR spectroscopy give different readings depending on whether the free radicals where created by high or low energy photons? Hypothetically we could imaging that free radicals created by high energy photons, would be located in clusters relative to free radicals created by low energy photons, because the free radicals would be created in abundance near the tracks of high energy electrons, where as for low energy photons they would be more evenly distributed. This could potentially effect EPR readings as the unpaired electrons could interact differently to its surroundings. This is called the ionisation density effect [36]. If there is energy dependence in signal detection, then it is corrected for in G_{Q,Q_0}

Therefore the total beam quality correction factor k_{Q,Q_0} is $(F_{Q,Q_0})^{-1}$. F_{Q,Q_0} is found from experiments by irradiating alanine dosimeters at a known dose-rate in different beam qualities, so together with the H_{Q,Q_0} found from Monte Carlo simulations, we can also find G_{Q,Q_0}.

F_{Q,Q_0} is equivalent to the relative response denoted as $r = \frac{D^c}{D}$, which is a different

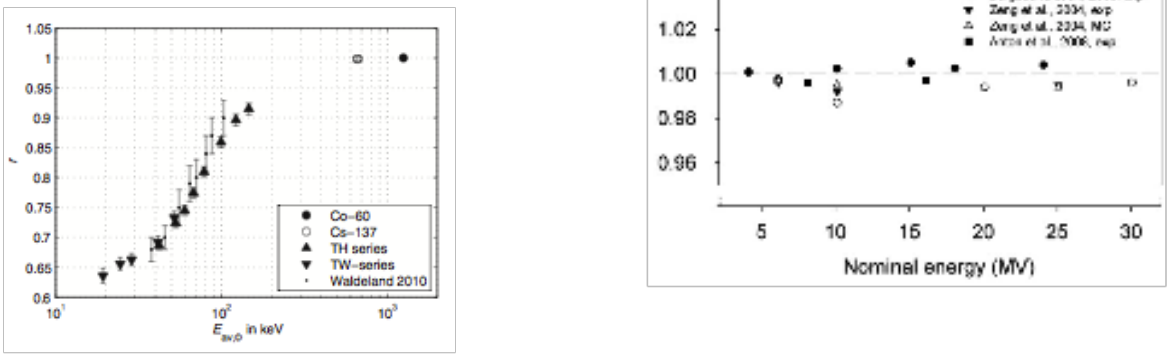

(a) **(b)**

Figure 14: ***a****; This figure show the F_{Q,Q_0} for alanine, for medium energy x-rays including ^{60}Co and ^{137}Cs for reference [4].* ***B****; This figure shows Monte Carlo simulated H_{Q,Q_0} and experimental F_{Q,Q_0} for different MV-beams [48]*

notation often used in literature [4] [5]. D^c is the dosimeter reading in absorbed dose to water based on a ^{60}Co calibration(Q_0), and D is the known value of the absorbed dose, so $D^c = M_Q N_{D,W,Q_0} = \frac{M_Q}{(M/D_W)_{Q_0}}$, $D = D_{W,Q}$, and $r = F_{Q,Q_0}$. In the relative response notation H_{Q,Q_0} is denoted r^{MC} and G_{Q,Q_0} is denoted η.

The results from literature shows that for medium energy x-rays, the energy dependence factor F_{Q,Q_0} increases with energy, see figure 14a, and for MV-beams it is close to unity $\pm 1\%$ see figure 14b.

4.6 Bruker EMX-micro

The EPR machine used for this thesis is an Bruker EMX-micro spectrometer The EMX takes a number of different parameters, which determine the spectrum modulation and readout conditions. In this thesis we used the recipe *Medical 2X4 Quartz 20Gy sweep* containing the used parameters [49]:

- **Frequency** is the microwave frequency set to 9.530787 GHz. This is called the X-band frequency.
- **Sweep width** is the magnetic field strength interval that is searched during sweeps, and is set at 20 Gauss, starting at 3880 Gauss.
- **Modulation**: The absorption response $\frac{\partial S}{\partial B_z}$ is found by calculating $\frac{\Delta S}{\Delta B_z}$ for each data point(there are 512 data points in the EPR spectrum), where the step size ΔB_z is the Modulation amplitude set to 10 Gauss. Too low a modulation amplitude would include too much noise, and too high would remove too much signal. ΔB_z is scanned for each data point by varying the magnetic field sinusoidally, while the

Figure 15: *This figure show the set up of the Bruker EMX-micro. Alanine dosimeter is place in the cavity, the bridge controls microwave emission, and detector.*

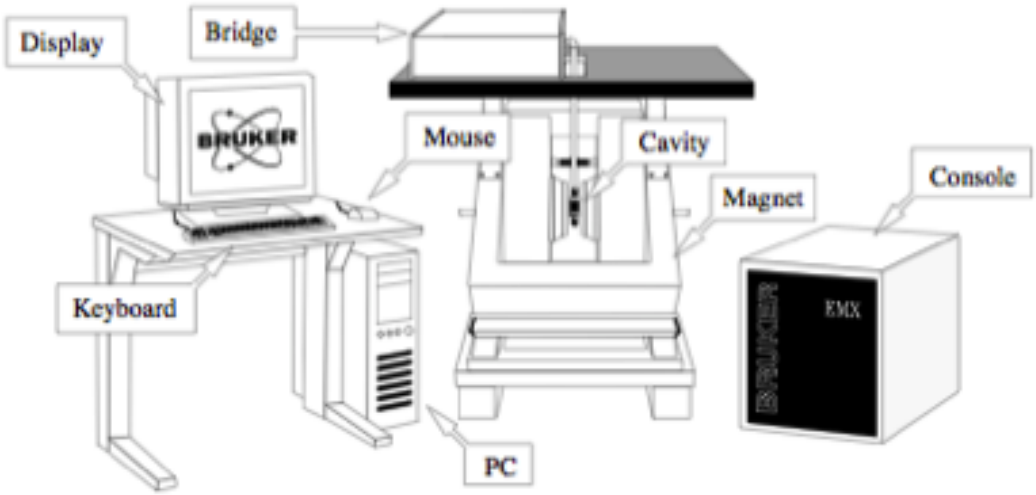

sweep goes through the sweep width. The modulation frequency is the frequency of the sinusoidal variation, and is set to 100 kHz.

- **Conversion time** is the time spend on each data point, which is 41 ms and $512 \times 41 \times 10^{-3} s = 21$ s is the sweep time.
- **Number of positions and sweeps**: The EMX would tune to the resonanse frequincy for each alanine dosimeter, before being given a total of 8 sweeps, first 4 sweeps, then we turn the quartz tube, holding the dosimeter, about $\pi/2$ radians, to filter out asymmetrical signal tendencies. This is especially important for doses in the clinical dose range [44]

The alanine dosimeters used in this thesis were manufactured by Harwell dosimeters, they are 9.1% paraffin wax and 90.9% L-α-alanine, with a bulk-density of 1.24 g/cm^3. They were shaped like small white cylindrical pellets with diameter 4.8 mm, and thickness 2.8 mm.

5 Ionisation Chamber Dosimetry

An ionisation chamber is a dosimeter, meaning it is capable of measuring absorbed dose given by radiation. The ionisation chamber uses a electrical field to collect the ion-pairs made by ionising particles in a volume of gas, or liquid. The connection between the absorbed dose and the ion-pairs made in the gas measuring volume is as described in section 3.4.4. Ionisation chambers come in different designs, but the two relevant for this thesis are the two following:

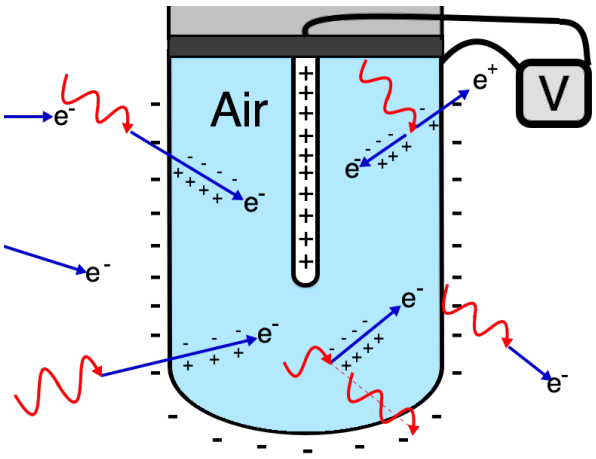

Figure 16: *This figure shows the schematic of a Farmer chamber air cavity during irradiation. High energy electrons ionise the air, and the ion-pairs are collected as charge. Note that in the assumptions of cavity theory, most of the electron fluence originate outside the air cavity, which is poorly represented in this figure.*

- **Farmer Chambers** have a cylindrical air cavity as the measuring volume, with a voltage between the chamber wall and a central electrode, as shown in figure 16 . Farmer chambers, have the size and geometry of a pencil, with the cavity volume, shown in figure 16, as the tip. The small cavity, and low uncertainty of the thimble chamber, is the reason that they are used for dosimetry in medical MV- and electron beams, as it wouldn't perturb the surroundings too much and are easily placed in special phantoms, made to resemble, lungs, chests, and etc.

- **Monitoring chambers** are plane parallel ionisation chambers, placed between the ionisation source and the phantom, as to give a measurement of the beam intensity and dose-rate.

5.1 Farmer Chamber Correction Factors

In relative dosimetry the dosimeters ability to measure a dose all depends upon matching the reference conditions as described in the calibration certificate. Some of these are done by matching the experimental set up, e.g. placing the dosimeter at a total distance between source and effective measuring point to be 1000 mm. Other deviations, however, must be factored out using the correction factors(k_i) described in this section. So if N_{D,W,Q_0} is the calibration factor, that converts measurements, made with beam quality Q_0(see next the page) in the correct reference conditions, into absorbed dose in water, then:

$$D_{W,Q} = (M_Q - M_0) \prod_{i=1} k_i N_{D,W,Q_0} k_{Q,Q_0} \tag{68}$$

We choose, for simplicity to denote an ionisation measurement subtracted a background measurement as:

$$M_Q - M_0 \to M_Q \tag{69}$$

We will now describe the relevant Farmer chamber correction factors [24] :

- k_{TP}: The number of ion-pairs that are made in the cavity, is proportional to the density of the gas, which the cavity is filled by. It is therefore necessary to factor out the difference between the density in the experiment and the density described in

the calibration certificate with a correction factor $k_{TP} = \frac{\rho}{\rho_r}$, where the subscript r means it is the reference conditions value. From the ideal gas law we know $\rho = \frac{p}{RT}$, where R is the gas constant, and T is the temperature in Kelvin, so the correction factor becomes:

$$k_{TP} = \frac{T_r p}{T p_r} \tag{70}$$

- k_{pol}: The polarity of the thimble chamber shouldn't affect the charge measurement, because the sign of collected charge will be the only difference, however a small polarity dependent deviation in the measured charge is observed in Ionization chambers [1]. This arises mostly from electrons stopping in the central electrode of the chamber, as these would be collected the same independent of the polarity, this is called Compton current. The correction factor for polarity is [38]

$$k_{pol} = \frac{|M_+| + |M_-|}{2M} \tag{71}$$

  Where $M_\pm$ is a measurement performed with a $\pm$ voltage in the chamber, and M is the measurement performed with operational voltage sign. k_{pol} must be found for each beam type as the polarity correction depends on radiation energy, and with each measurement multiplied by its associated k_{TP} [38].

- k_s. Some times the ion-pairs created in the cavity will recombine before the charge is collected, this can happen in the following ways:

  - Ions recombine with ions from a different ionising particle track, this would depend on the density of particle tracks and therefore the dose-rate.
  - Ions recombine with ions from the same particle track, this would be independent of the dose-rate.

  Both effects decreases for higher voltage and increases for lower voltages. The correction factor for a pulsed beam is found by Boarg theory [12] [11], to be:

$$k_s = 1.198 - 0.875\left(\frac{M_1}{M_2}\right) + 0.677\left(\frac{M_1}{M_2}\right)^2 \tag{72}$$

  Where M_i is a measurement with voltage V_i, and $\frac{V_1}{V_2} = 3$. For a continuous beam like ^{60}Co the correction factor is found by:

$$k_s = \frac{(V_1/V_2)^2 - 1}{(V_1/V_2)^2 - (M_1/M_2)} \tag{73}$$

  All measurements must be multiplied by its associated k_{TP}, and k_s must be found for each beam quality.

- k_{Q,Q_0}: Each energy spectrum of a photon radiation beam has a unique dose-depth curve, which therefore also deposits the dose with a unique charged particle energy spectrum at the measurement point, which we know from cavity theory in section 3.4.3 would give a different absorbed dose measurement, because $s_{med,cav}$ is dependent on the charged particle energy. It is therefore necessary, when comparing ion

chamber measurements made with different photon beams, to correct for the energy dependence.
First we quantify the beam energy spectrum with a beam quality index, chosen in this report[8] as the tissue phantom ratio $\mathrm{TPR}_{20,10}$:

$$\mathrm{TPR}_{20,10} = \frac{(Mk_{TP}k_{pol}k_s)_{20cm}}{(Mk_{TP}k_{pol}k_s)_{10cm}} \tag{74}$$

$\mathrm{TPR}_{20,10}$ is the ratio of absorbed dose given at a depth of 20 cm and 10 cm in a water phantom, for a fixed SCD(Source Chamber Distance) of 100 cm and a beam size of 10×10 cm at the SCD [24]. The correction factor for measurements made with a beam quality(Q) different from the reference beam quality(Q_0), should change the calibration factor accordingly:

$$M_Q N_{D,W,Q_0} k_{Q,Q_0} = M_Q N_{D,W,Q} \quad \Leftrightarrow \tag{75}$$

$$k_{Q,Q_0} = \frac{N_{D,W,Q}}{N_{D,W,Q_0}} = \frac{(s_{W,air})_Q (W_{air})_Q (p_{\mathrm{fl}} p_{\mathrm{dis}} p_{\mathrm{wall}} p_{\mathrm{cel}})_Q}{(s_{W,air})_{Q_0} (W_{air})_{Q_0} (p_{\mathrm{fl}} p_{\mathrm{dis}} p_{\mathrm{wall}} p_{\mathrm{cel}})_{Q_0}} \tag{76}$$

From equation 44: The combined errors as described in section 3.4.4, give an uncertainty of 1% when using calculated values of k_{Q,Q_0}, which can be diminished a lot by using experimentally determined values. The commonly used reference beam quality is ^{60}Co, so from now on, if the beam quality subscript is missing, then it denotes ^{60}Co as the beam quality, e.g. $k_{Q,^{60}\mathrm{Co}} \to k_Q$, $N_{D,W,^{60}\mathrm{Co}} \to N_{D,W}$.

6 Monte Carlo

Monte Carlo is a computational method, used for solving math and physics problems, by repeating events described by a probability distribution(stochastic processes) e.g. bacterial growth, diffusion, and particle interactions. In this thesis, the egsNRC(electron gamma shower National Research Counsel Canada) software is used to model radiation transport.

6.1 Random Sampling in egsNRC

egsNRC works by simulating a large number of particle histories(called histories), each particle history contains the result of a simulated particle and all its secondary particles(and thirds, and so on till the kinetic energy has reached the cut off value), in a user chosen environment of materials and geometry. The aspects of particle simulation that requires random sampling from probability distributions, are the following:

- **Starting energy** The starting energy of all the primary particles[9] should follow the energy spectrum of the simulated source(radioactive material, MV-beam, or electron beam). This can be done, for finite spectra, using the acceptance-rejection method [14]

[8] There exists other beam quality indexes, which has other ways of defining the beam.
[9] primary particle is the starting particle of a history

If $f(E)$ is the energy spectrum, $\hat{r_1}, \hat{r_2}$ are random numbers of uniform distribution in the interval $[0,1]$, $h = \max(f(E))$ and $k = \max(E) - \min(E)$, then we draw the spectrum in a rectangle of $h \times k$ and make random points in the rectangle with coordinates $(E_r, h_r) = (r_1 k, r_2 h)$. All points with $h_r > f(E_r)$ are discarded and the points with $h_r < f(E_r)$ are accepted with their energies E_r as the random sample drawn from the energy spectrum.

- **Travelling distance** As described in section 3.3.2 and 3.3.3, photons and electrons, have several possible interactions, all of which have cross sections determining their likely hood, so the distance travelled by the particle before interacting is also found by random sampling [34]. We will use photons as example:

  In section 3.3.1 we saw that the probability density function for interacting at distance x is[10] $p_{pdf}(x) = \mu e^{-\mu x}$, so in a area of constant μ we can define the mean free path as the mean distance travelled by the photon before interacting as:

$$\lambda = \langle x \rangle = \mu \int_0^\infty x e^{-\mu x} dx = \mu \left[x \frac{e^{-\mu x}}{-\mu} \right]_0^\infty - \mu \int_0^\infty \frac{e^{-\mu x}}{-\mu} dx = \frac{1}{\mu} \tag{77}$$

  The geometric set up of egsNRC is divided into regions of constant density and materials, so if the photon moves from one material to another, the attenuation coefficient would change, so if $x_0, x_1 \ldots$ are the boundary distances of the regions, in the direction of the photon, and x is the travelled distance, we can patch together the probability function for not interacting, after travelling a distance x, as:

$$p(x) = \begin{cases} e^{-\mu_1 x} & \text{if } x \in [0, x_1[\\ e^{-\mu_2 x} & \text{if } x \in [x_1, x_2[\\ \vdots & \vdots \end{cases} \tag{78}$$

  If we make the coordinate transformation of $x \to \frac{x}{\lambda_i} = N_\lambda$, where N_λ is the number of mean free paths, equation 78 becomes independent of region boundaries and describes the probability of travelling N_λ without interacting. We integrate over $p(N_\lambda)$ to find its cumulative distribution:

$$P(N_\lambda) = \int_0^{N_\lambda} e^{-N'_\lambda} dN'_\lambda = 1 - e^{-N_\lambda} \tag{79}$$

  $P(N_\lambda)$ is the the probability distribution of the number of mean free paths, the photon travels before interacting, and we are therefore interested in making random samples from it, which we can find using the inverse-transformation method: [35] If $\hat{N_\lambda}$ is a random variable, following the distribution of equation 79 then $P(\hat{N_\lambda})$ should equal uniformly random numbers in the interval $[0,1]$, we define such a random variable as $\hat{r}$, and write:

$$\hat{r} = 1 - e^{-\hat{N_\lambda}} \quad \Leftrightarrow \quad \hat{N_\lambda} = -\ln(1 - \hat{r}) = -\ln(\hat{r}) \tag{80}$$

  The algorithm is then as follows: Pick a value of N_λ using equation 80

[10] the factor of μ is easily found by normalising it: $1 = C \int_0^\infty p(x) dx$

1. compute λ at the current location.
2. let t_1 be λN_λ
3. Compute d, the distance to the next boundary in the the photon's direction.
4. Let $t_2 = \min(t_1, d)$, and transport the photon the distance t_2.
5. Deduct $\frac{t_2}{\lambda}$ from N_λ. If the result is zero the photon interacts and the algorithm stops here.
6. If this step is reached then the photon is at a boundary. If the new region is the same material, then go to step 2, with $N_\lambda - \frac{t_2}{\lambda}$ as N_λ. If the region is a different material go to step 1. also with $N_\lambda - \frac{t_2}{\lambda}$ as N_λ.

The algorithm is a bit different for photons in a vacuum as $\lambda = \infty$.

- **Interaction type** Once a interaction happens, the types are chosen according to their cross sections. the possible photon interactions included in egsNRC are: Photoelectric absorption, Compton scattering, Pair production, Triplet production and Rayleigh scattering. The sampling is done using a process similar to the Gillespie algorithm, by summing up the cross sections : $Q = \sum_i \sigma_i$, picking a random number $\hat{r}$ from a uniform distribution in the interval $[0, 1]$, and choosing the j' interaction in the following expression:

$$\sum_i^{j-1} \sigma_{i-1} < \hat{r}Q \leq \sum_i^{j} \sigma_i \tag{81}$$

This will pick the interactions, according to their cross sections.

Once a interaction is found, the parameters are sampled from the differential cross section $\frac{d\sigma}{d\Omega}$, $\frac{d\sigma}{dE_t}$, etc. These are sampled using the inverse transformation, and acceptance-rejection method, if however the PDF $p(x)$ doesn't have a inverse function $p^{-1}(p)$, and a infinite variable interval(e.g. $x \in [0, \infty[$), then neither of the two methods are possible, and a combination of the two are used. We choose a function $h(x)$, for which $h^{-1}(h)$ exists, and $h(x) \geq p(x)$ for all x, we then sample $\hat{x}$ from $h(x)$ using the inverse transformation method, and pick a random number from $\hat{r}$. We reject a value $\hat{x}$ if $\hat{r}h(\hat{x}) \geq p(\hat{x})$ and accept it if $\hat{r}h(\hat{x}) < p(\hat{x})$, this will sample values from $p(x)$, which, if $p(x)$ is the normalized differential cross section, will pick the scattering solid angle Ω, kinetic energy transferred, spin state, and etc.

6.2 Condensed Histories

The electron interactions included in egsNRC are Bremsstrahlung, Møller scattering, Bhabha scattering, electron-positron annihilation, and elastic coulomb scattering of nuclei, which could be simulated according to their cross sections in the same way that photon transport is. However, in the process of slowing down, the electron performs in the range of $10^5 - 10^6$ interactions, of energy loss and direction changes, which would be very time consuming to simulate in the same manner as the photon transport. Therefore in the early sixties M. Berger [8] introduced the technique of condensed histories,

in which many of these interactions are grouped together to a single step of energy loss, path length, change in direction, and physical displacement. This is motivated by the fact that the physical state of the electron is not changed a lot by the single interactions [26] [27]. Only Bremsstrahlung events which make photons of energies high enough to make knock-on electrons are sampled explicitly.

There are user chosen lower energy limits for the energy of electron and photons, for each material, called AE and PE respectively. When the energy of an electron(photon) reaches a value lover than AE(PE),there is no possibility for the creation of secondary particles, and the remaining range and energy transfer can be simulated in an simpler fashion. Globel energy cuts for particle transport called ECUT and PCUT, determine when egs stops calculating it's cross section, and the particles simulation stops.

6.3 User Codes and Uncertainty

The user code chosen for a simulation in egsNRC determines what data is gathered, the type of geometry you can design, and the source type(point source, parallel beam, etc.). There are a number of different user codes in egsNRC, but the ones relevant for this thesis are the following:

- **dosrznrc** collect the dose and kerma in cylindrical geometry. The dosrznrc usercode was used to find the D_W and D_{Ala} needed in equation 65.
- **flurznrc** collects the energy- and particle fluence in a cylindrical geometry. flurznrc was used to find the energy spectrum of the two ^{60}Co source geometries, in the vicinity of the dosimeters.

The data is given pr. region in the geometry, as the average quantity(dose, kerma, energy fluence, etc.) in that region pr. history. The uncertainty is calculated as [26]:

$$\sigma_{\bar{X}} = \sqrt{\frac{1}{N-1}\left(\frac{\sum_{i=1}^{N} X_i^2}{N} - \left(\frac{\sum_{i=1}^{N} X_i}{N}\right)^2\right)} \tag{82}$$

Where N is the number of histories, and X_i is the quantity given to the region during the i' history.

7 Experiments and Simulations

7.1 Open Source Geometry

The calibration is made by first determining the dose-rate for certain reference conditions by using a dosimeter calibrated to a secondary standard by a Secondary dosimetry Lab, and then irradiate alanine dosimeters in the same reference conditions, to get a series of alanine dosimeters with a know dose traceable to a SDL. In this calibration we used a Farmer chamber calibrated by PTB(Physikalische Technische Bundesanstalt). The reference conditions as stated in the calibration certificate of Farmer chamber FC65G, S/N 857:

- Radiation quality: ^{60}Co γ radiation
- Irradiation temperature: 20°
- Air pressure: 1013.25 hPa
- Rel. humidity: 50 %
- Absorbed dose-rate to water: 0.859 Gy/min.
- Beam size at the front of the phantom: 10 × 10 cm.
- Distance between outer phantom surface to the effective measuring point: 5 cm.
- Distance between source and phantom surface: 95 cm.
- Potential of chamber thimble: 0 V.
- Potential of central electrode: 300 V.
- Phantom: 30 × 30 × 30 cm water tank with a 3 mm PMMA entrance window.
- Effective measuring point: is 11 mm from the tip, in the center.

The conversion factor is $N_{D,W} = 4.801^7$ Gy/C, already factored with a $[k_{pol}]_{^{60}\mathrm{Co}} = 1.001$ correction factor. The conversion factor is traceable to the primary standard of PTB with a relative uncertainty of 0.5% coverage factor $k = 2$.

The experiment takes place at RISØ's medical dosimetry laboratory in building 313, due to limited time the irradiations had to be split up over two days: 24/06-2016 and 28/06-2016. The source is a high activity ^{60}Co sample, manufactured in Chech republik by UJP Praho A.S, with an activity of 455TBq on 6/06-2012. The sample consist of 1 mm thick ^{60}Co disc pellets in a cylindrical stainless steel container of height $h = 39.3$mm, and diameter $d = 23.6$mm. The source is placed in a thick lead container that is capable of opening in front of a collimator, which shapes the beam size. The beam hits a water tank phantom made of PMMA, and inside the tank is the dosimeter positioned, see figure 17.

The set up is made to replicate the reference conditions of the Farmer chambers calibration: The total distance between the ^{60}Co source and the dosimeter is SCD(Source to Chamber Distance)= 1000 mm and the combined density thickness of water and PMMA wall is 5 g/cm^2. The beam size is set to be 10 × 10 cm at the depth of the dosimeter, which has been found empirically to be when the collimator is set at 9.97 × 9.97 cm. The remaining difference from the reference conditions are: temperature, Pressure, ion-recombination and polarity, which will be corrected using correction factors described in section 5.1. A reference plate can be mounted in front of the collimator, which is calibrated to a distance of 472.55mm from the source(A on figure 17). Before the water tank is raised and positioned, a board with calibrated distance is placed against the reference plate to find the SCD = 1000 mm. Once the SCD is found, two thin crosses are placed on each side of the SCD, such that aligning both crosses when looking through

with an alignment telescope, the center of the scope would be SCD = 1000 mm see figure 18, the crosses are kept in the same position during both Farmer chamber and alanine positioning, to keep the precision[11] of the dosimeter positions as high as possible. The water tank is then raised up submersing the dosimeter in water, and then slowly moved towards the source until the tank wall is at a distance of 950.63 mm from the source(A + C in figure 17), this distance is determined by a digital calliper attached to a bored, calibrated to 478.08 mm see figure 19. Four independent thermometers[12] where used during the irradiations: 2 for the room temperature, and 2 for the water temperature. 2 barometers and a hygrometer was also present during the experiment.

The uncertainty in copying the reference conditions is listed below:

- u_B = 3 mm, for the source to reference plate distance of 472.55 mm(A), this is mostly due to the fact that we don't know the distribution of ^{60}Co inside the sources container. Therefore when comparing to the reference conditions used with a different ^{60}Co source, we add an estimated uncertainty of ±3 mm.

- u_B = 0.04 mm, for the calliper used in both, the distance between the reference plate and the water tank(C), and the distance between the reference plate and the dosimeter(B). Even though the calliper has a precision of ±0.001mm I found that when calibrating to a fixed distance multiple times, the calliper showed variations of ±0.004mm, due to the human element in calibrating the calliper[13].

The alanine dosimeters where helped in place during irradiations in a PMMA special dosimeter holder, see figure 20, the effective measuring point is chosen to be in the center of the ring with the 6 alanine dosimeters on the periphery, with SCD = 1000 mm as the center of the dosimeters.

On 24/06-2016, 3 batches of 6 alanine dosimeters where irradiated for 3600 s, 1804.9 s and 500 s respectively, thereafter the Farmer chamber where placed and in a continues irradiation of several minutes, in which multiple 30 s measurements where made with 300 V on the central electrode.

On 28/06-2016, First, multiple Farmer chamber measurements of 30 s. where made for 300 V, −300 V and 100 V in one continues irradiation. Then 3 batches of 6 alanine dosimeters where irradiated for 400 s, 200 s and 100 s respectively. Then the first Farmer chamber measurements where repeated. Lastly to investigate the uncertainty in positioning the dosimeter with the alignment telescope, the ion chamber was re-positioned 6 times starting from an unknown position. After each re-positioning the ion chamber was irradiated and multiple 30 s measurement where made.

[11] Not the accuracy

[12] Semi-independent as they where all connected to the same electro meter

[13] the calliper is calibrated to a certain distance by placing its attached plate between two blocks of fixed distance.

Figure 17: *This figure show a simplified schematic of the experimental set up used in the open* ^{60}Co *geometry calibration. A is the distance between the source and the reference plate, used for determining the SCD. B and C, are the distances from the reference plate to the dosimeters measuring point, and the water tanks wall respectively.*

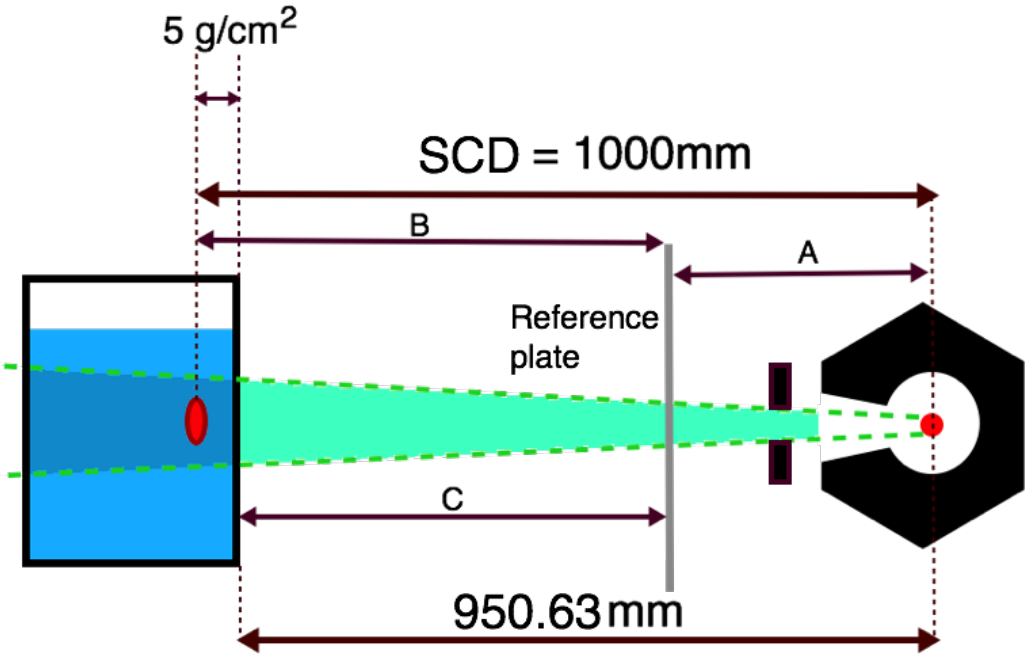

7.1.1 Results

The polarity correction factors where calculated as described in section 5.1, using the data gathered on 28/06-2016 and is shown in table 1. The recombination correction factors are calculated as described in section 5.1, using the data gathered on 28/06-2016 and is shown in table 1.
In calculating the dose-rate for both experiment days, we used the mean of the, before and after, values showed in table 1. The dose-rates calculated according to equation 68, with $k_Q = 1$, are shown in table 2. The alanine dosimeters were readout, and handled as described in step 1 - 3 of the algorithm in section 4.4, the P2P values where then assigned the absorbed dose to water:

$$D_W = \dot{D} t_b \tag{83}$$

where $\dot{D}$ is the dose-rates of table 2, and t_b is the irradiation time of the pellets associated batch. The calibration curve along with it's residuals is shown in figure 21. The alanine signal residuals where calculated as:

$$y_{resi} = \frac{\text{P2P} - fit}{fit} \tag{84}$$

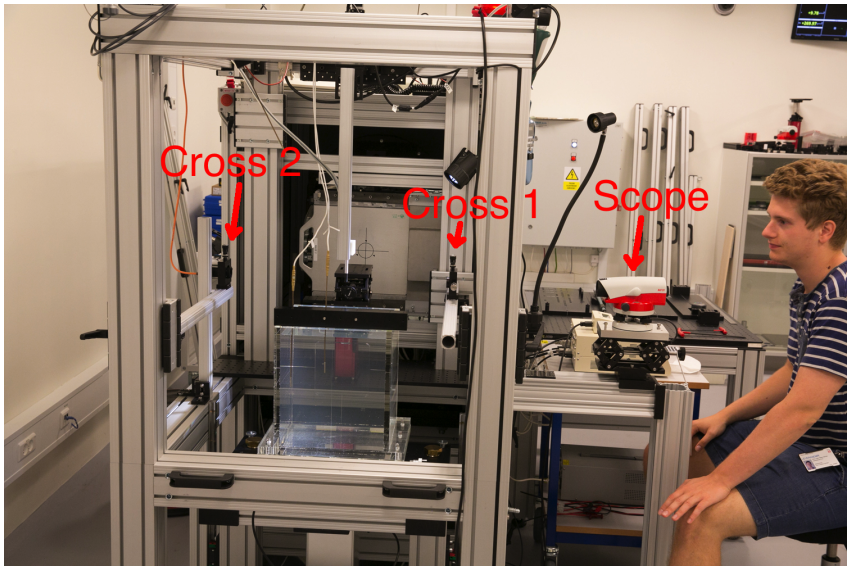

Figure 18: *This Picture was taken while positioning the Farmer chamber at SCD = 1000mm using the Scope and crosses. The mounted reference plate is also visible as the metal plate with the black cross and circle on.*

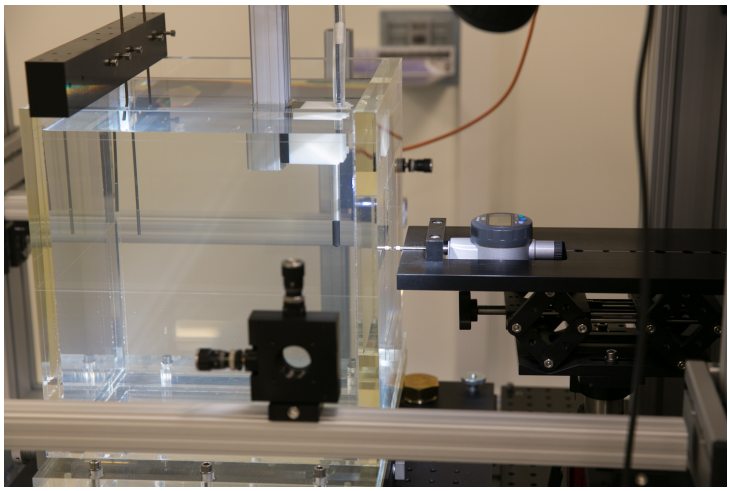

Figure 19: *This Picture was taken during the positioning of the water tank. At the front is shown one of the two optical scope calibration crosses set at SCD = 1000mm, the other one is located behind the water tank. The Black plate shown to the right has a digital calliper calibrated to, when placed against reference plate, give the target distance between the source and the water tank 950.63mm(C + A in figure 17).*

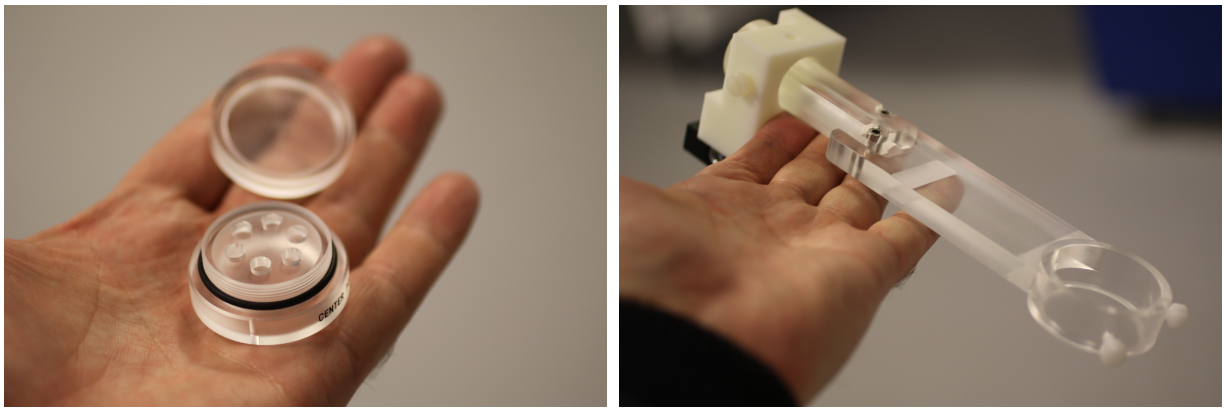

(a) **(b)**

Figure 20: *This figure show two pictures of the alanin holder used in the open source geometry irradiations and MV-beam irradiations. It is made from PMMA, and can contain 6 alanine pellets.* ***a****, is the alanine pellet container which was manufactured by PTW and keep the pellets water proof with a screw-on lid. its serial number is T41023.1.110.* ***b****, is the alanine container adapter, which was also manufactured by PTW, and its serial number is T41023.1.110.*

Table 1: Table of polarity and ion recombination correction factors calculated with equation 71 and 73 for ^{60}Co radiation. The operational voltage for k_{pol} was $M_+ = 300$ V. The type A uncertainty, found with error propagation on the standard deviation of equation 46($N = 4$), is $\pm 0.03\%$ for k_{pol}, and $\pm 0.09\%$ for k_s. k_{pol} has been divided by the $[k_{pol}]_{Q_0}$ of the calibration certificate. All the measurements used in calculating k_s and k_{pol}, where made 28/06-2016 before and after alanine irradiation.

	k_{pol}	k_s
Before	1.0003	0.99961
After	1.0003	0.9993

Table 2: Table of dose-rates of the open ^{60}Co geometry, calculated from equation 68 with type A uncertainty of $\pm 0.16\%$, calculated from error propagation. The used k_{pol} and k_s are the mean values of table 1.

	24/06-2016	**28/06-2016**
Gy pr. s	$(1.9572) \times 10^{-2}$	$(1.9560) \times 10^{-2}$

Figure 21: *This figure shows the open* ^{60}Co *geometry calibration curve, made from 6 irradiations, each batch with 6 or 5 alanine dosimeters*

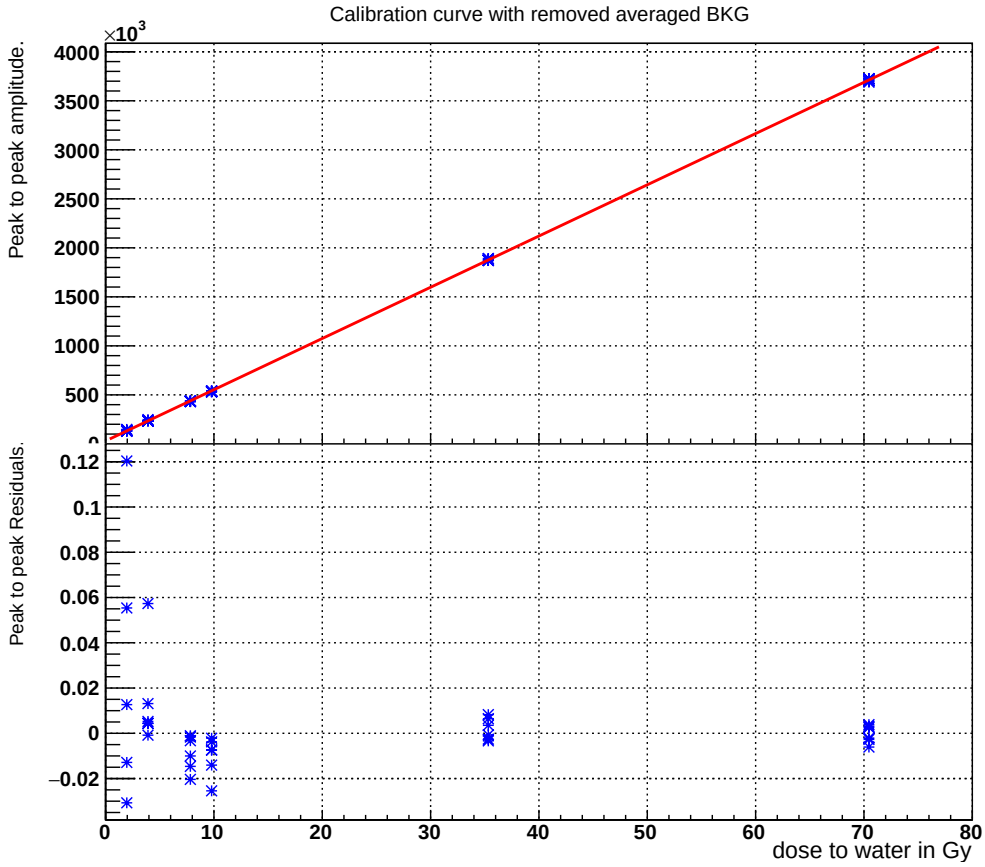

7.2 Closed Geometry

The experiment takes place in the cellar of building 206, at DTU Risø, with the Gammacells of the high dose reference laboratory(HDRL). Gammacell 1, has 16 rods of ^{60}Co

placed in a circle, thereby giving an uniform radiation field in the center. Unlike the open ^{60}Co geometry, this set up is already calibrated to a known dose-rate traceable to the primary standard of NPL with type B uncertainty 1.39%. The gamma cell can contain batches of 4 alanine pellets at the time, which mechanically are lowered into the cell for the irradiation period. The irradiation period is determined by a calibration spreadsheet, which takes into account the transient dose and the calibrated dose-rate. The alanine dosimeters where irradiated in batches of 4, placed as corners of a square in a cylindrical PMMA holder. The holder is placed inside a nylon cylinder, which is placed in a steel cylinder. The steel cylinder containing the batch of alanine dosimeters are lowered mechanically into the gamma-cell for the time calculated by the spreadsheet. Five batches, where put in a heating cabinet, set to 21°, for a minimum of 30 min, before being irradiated to the following doses: 100.0, 19.99, 5.01, 3.99, 3.02, 2.01, and 0.99 Gy

7.2.1 Results

Figure 22: *This figure shows the closed* ^{60}Co *geometry calibration curve, made from 7 irradiations, each with 4 alanine dosimeters*

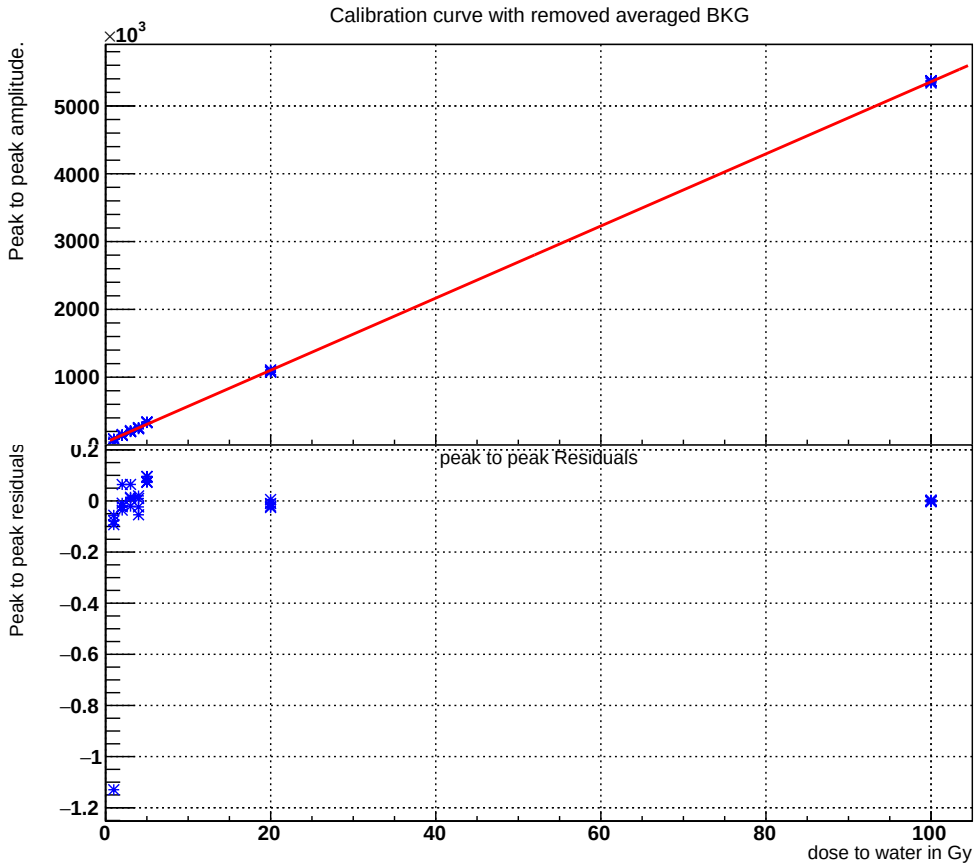

7.3 MV-Irradiations

The experiments took place at RISØ's medical dosimetry laboratory in building 313. The source was a Varian Truebeam linear accelerator, designed for radiotherapy and dosimetry, and capable of firing both photon and electron beams of various energies. A water tank is placed so the SAD(Source Axis Distance) is located at a depth of either 10 cm or 20 cm, see figure 24. The photon energy spectra used, are denoted as EX, where E is the nominal energy of the electrons fired towards the target, in MeV, when producing the x-rays. a functional form of the energy spectra are showed in figure 23. The goal of the experiment is to first measure the beam quality index, and dose-rate with a Farmer chamber, then irradiate batches of alanine dosimeters. All for the different photon beams, and in reference conditions that match the Open ^{60}Co geometry irradiations, as to readout the dose with the calibration curve. Two days were used for the experiments. The first was performed on 24/05-2016 in which three photon energies where used: 6X, 10X, and 18X, the second was performed on 23/06-2016 and was a follow up experiment with five different photon energies: 4X, 6X, 10X, 15X, and 18X.

Figure 23: *This figure Shows both the photon fluence, and energy fluence for the 5 photon energies used in the MV beam experiments, as constructed by the functional form as described by Ali and Rodgers in [2]. Both spectra are normalized, and where used for simulating the source in the particle transport simulations.These spectra were provided by C. E. Andersen DTU Nutech*

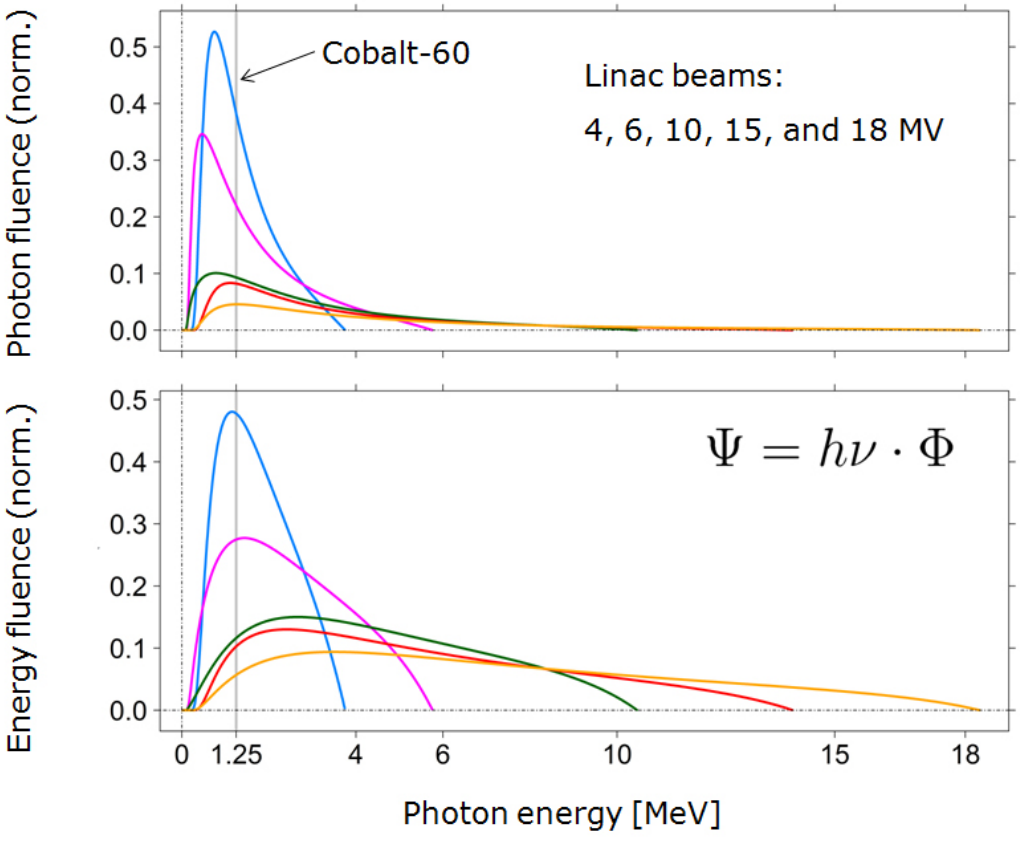

The same Farmer chamber, that was used i the open source experiment, was used for the MV-beam experiments, and the same alanine holder and effective measuring point

Figure 24: *This figure show a simplified sketch of the experimental set up. The gray shape containing letters A,D, and E is the Varian Truebeam linear accelerator, with it's rotating axis as the vertical dotted line in the center of the figure. The triangle next to A is the Target. The red cylinder is the position of the dosimeters, both alanine and Farmer chamber, always placed with there effective measuring point at the SAD. The two black rectangles at C is the collimator calibrated to a beam size of 10 X 10 cm at the SAD. The black line next to F is where the monitor chamber and front pointer is positioned when either performing irradiations or calibrating distances. D and E represent the electron gun and beam, of the complicated inner workings.*

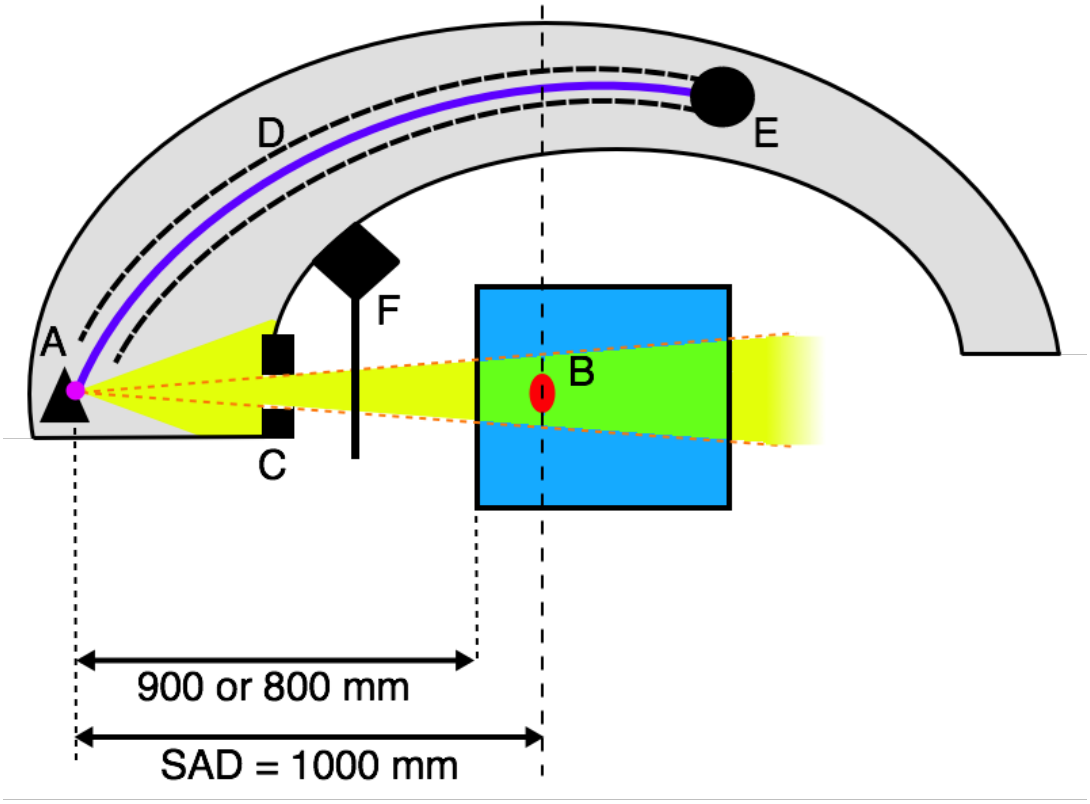

for alanine was also used. They were both placed, using an alignment telescope, at SAD = 1000 mm see figure 27. Both the water tank, and the alignment telescope was positioned at their needed distances from the source, using a manufacture calibrated front pointer(shown as F in figure 24). We estimate the type B uncertainty from the human element in using the front pointer to be 0.5 mm.
On both experiment days, Farmer chamber measurements where made for water depths of 10 and 20 cm, voltages of -300 V, -100 V, and 300 V, for each of the photon energies used in the experiment. At least four repeated measurement where made for each set up. Measurements with 4X, 6X and 10 was of 100 MU, and measurements with 15X, and

Figure 25: *This figure show the experimental set up used for the MV-beam irradiation experiments. Visible in the picture is the monitor chamber and the Farmer chamber.*

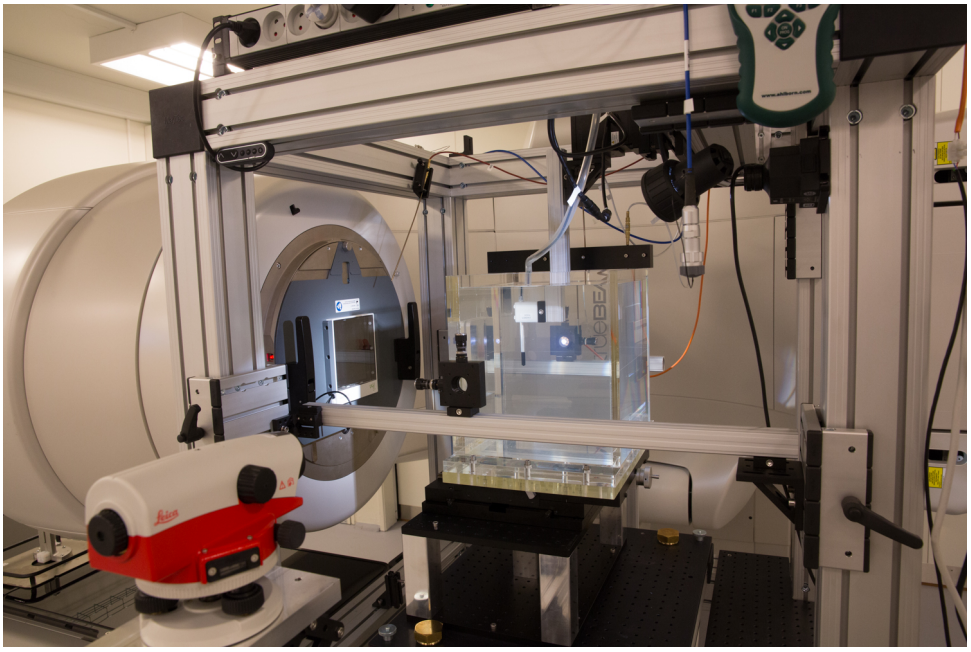

18X was of 90 MU. Four independent thermometers where used during the experiments, two for water temperature and two for room temperature. 2 barometers and hygrometer was also present during the experiment.

On 24/05-2016, batches of four alanine dosimeters[14], were irradiated to 2500 MU in each of the three photon beams 6X, 10X, and 18X.

On 23/06-2016, batches of 6 alanine dosimeters, were irradiated to 4000 MU in each of the five photon beams 4X, 6X, 10X, 15X, and 18X. Two batches where made of each 6X and 15X.

7.3.1 Results

The ionisation chamber correction factors for polarity and ion recombination is found for the experiments performed on 24/05-2016, and 23/06-2016 are shown in table 3 and 4, calculated with equation 71 and 72, and the errors are type A, found with error propagation to be:

$$\sigma_{pol} = \sqrt{\frac{\sigma_{M_-}^2}{M_+^2} + \left(\frac{1}{M_+} - \frac{M_+ + M_-}{M_+^2}\right)^2 \sigma_{M_+}^2} \tag{85}$$

$$\sigma_s = \sqrt{\left(-\frac{0.875}{M_2} + \frac{1.354 M_1}{M_2^2}\right)^2 \sigma_{M_1}^2 \left(\frac{0.875 M_1}{M_2^2} - \frac{1.354 M_1^2}{M_2^3}\right)^2 \sigma_{M_2}^2} \tag{86}$$

Where σ_M is the type A standard deviation from repeated measurements. The beam

[14]they where placed so three alanine dosimeters in the "top", and the last one was in the bottom.

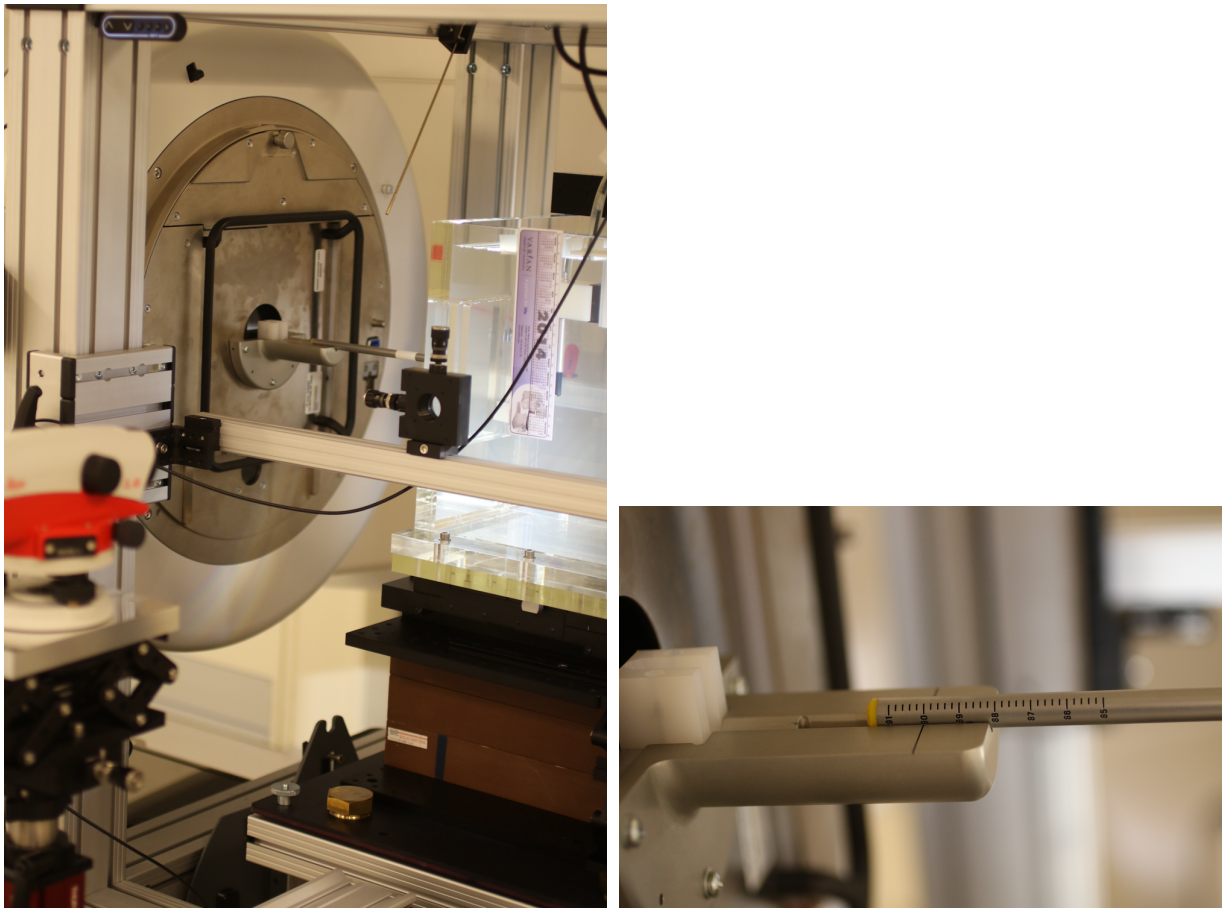

(a) **(b)**

Figure 26: *This figure show two pictures of the manufacture calibrated frontpointer, which is used for determining distances from the source.* ***b*** *show how the the front pointer is placed infront of the source, using the metal pointer to set the water tank at the correct distance from the source.* ***a*** *shows how the distance from source is measured: the pointer has an ingraved ruler on its side, giving the distance between pointer tip and source, as the visible black line.*

Table 3: Table of polarity correction factors k_{pol} for $M = M_+$ divided by $[k_{pol}]_{Q_0}$, and Ion recombination correction factors k_s, for the MV beam experiments performed 24/05-2016. 4 irradiations where made for each energy, in each depth, for both +300 V, −300 V and 100 V. the type A uncertainty of $46(N = 4)$ is ±0.003% for k_{pol}, and ±0.02% for k_s.

	6X	**10X**	**18X**
$k_{pol,10cm}$	0.99992	0.99967	0.99944
$k_{pol,20cm}$	0.99954	0.99961	0.99954
$k_{s,10cm}$	1.0033	1.0040	1.0081
$k_{s,20cm}$	1.0027	1.0033	1.0066

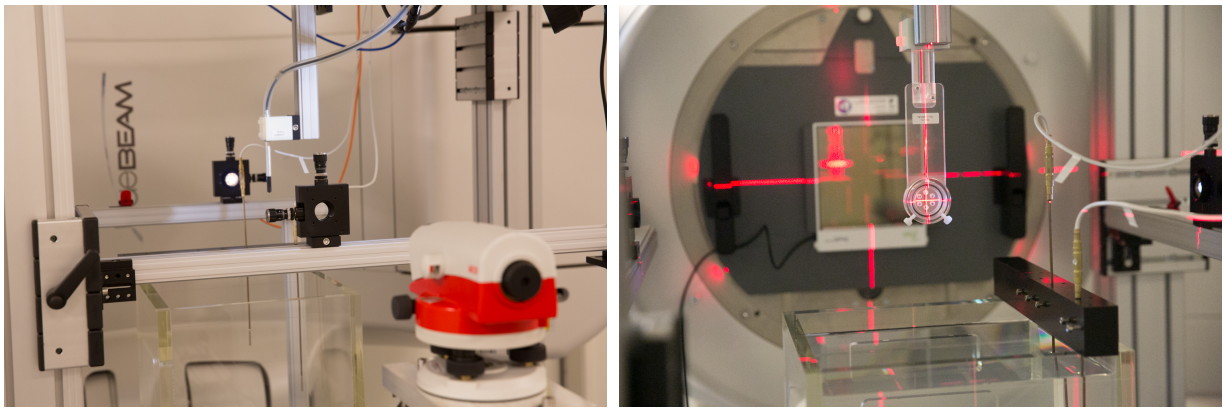

(a) **(b)**

Figure 27: ***a****; This figure shows the alignment telescope, used for positioning the the dosimeters at the correct distance from the source, in both the open source* ^{60}Co *and MV-beam irradiations.* ***b****; This figure shows the lasers used to place the dosimeters correct at the angles that the alignment telescope can't calibrate. Lasers where used in both the open source and the MV-beam.*

Table 4: Table of polarity correction factors k_{pol} for $M = M_+$ divided by $[k_{pol}]_{Q_0}$, and Ion recombination correction factors k_s, for the MV beam experiments performed 23/06-2016. 4 irradiations where made for each energy, in each depth, for both +300 V, −300 V and 100 V. The polarity correction factor was only found for depth of 10 cm. The type A uncertainty of $46(N = 4)$ is ±0.001% for k_{pol}, and ±0.08% for k_s.

Q	$\boldsymbol{k_{s,10\text{ cm}}}$	$\boldsymbol{k_{s,20\text{ cm}}}$	k_{pol}
4X	1.0016	1.0016	0.999679
6X	1.0033	1.0029	0.999905
10X	1.0041	1.0034	0.999750
15X	1.0080	1.0064	0.999808
18X	1.00836	1.0067	0.999565

Table 5: Table of beam quality index $TPR_{20,10}$, for both MV beam experiments. The uncertainty are $\pm 0.3\%$ and are calculated in section 8.2.6. The significance of the difference between the values of the two experiments, is shown in number of sigma z as described in section 3.5.

Q	$TPR_{20,10}$(23/06-2016)	$TPR_{20,10}$ (24/05-2016)	z
4X	0.622		
6X	0.668	0.667	0.7
10X	0.739	0.738	0.9
15X	0.763		
18X	0.782	0.781	0.8

Table 6: Table of Farmer chamber dose-rates from MV radiation in Gy pr MU. The values have been factored by all correction factors including k_Q, The differences in dose-rates between the two experiments are shown in significance z. The uncertainty is $\pm 1\%$ for both dose-rate and k_Q.

Q	Dose-rate(23/06-2016)	k_Q (23/06-2016)	Dose-rate (24/05-2016)	z
4X	7.84×10^{-3}	0.997		
6X	7.82×10^{-3}	0.993	7.87×10^{-3}	0.53
10X	9.21×10^{-3}	0.982	9.27×10^{-3}	0.56
15X	9.59×10^{-3}	0.975		
18X	9.87×10^{-3}	0.968	9.94×10^{-3}	0.58

quality index $TPR_{20,10}$ is calculated according to equation 74, and are shown for both experiments in table 5, the uncertainty is calculated and discussed in section 8.2.6. the dose-rates are calculated according to equation 68, and shown, along with their k_Q factors in table 6

7.4 Monte Carlo Simulations

egsNRC was used to calculate the energy dependence factors of equation 65. The simulation geometries are made in a cylindrical coordinate system, so there is not a perfect way to model the alanine pellet dosimeters as placed in the irradiation experiments. Not knowing whether the best way to model the pellet placement of figure 20, is to model a single pellet in the center, or a cylindrical ring of alanine, we choose to run simulations for both cases. We perform one simulation for each value of $(D_{Ala1})_Q$, $(D_{Ala2})_Q$, and $(D_W)_Q$, for each of the two geometries, with $Q = {}^{60}$Co, 4X, 6X, 10X, 15X, and 18X making it a total of 36 simulations each of $1 - 5 \times 10^9$ histories.

The energy spectra needed for simulating the source are shown in figure 23, for the MV-beam. For simulating the ^{60}Co sources, simulations where made with the flurznrc usercode in geometries matching the source, collimator and phantom, see figure 28 and

29. The source was given a spectra of two possible γ rays: 1.175 MeV for 49.94% of the emitted gammas, and 1.335 MeV for 50.06% of the emitted gammas. The spectra obtained from the flurznrc simulations was then used as the source energy spectra in the ^{60}Co dosrznrc simulations.

The dosrznrc simulations for D_{Ala} where made in the geometries of figure 33, 32, 30, and 31. The simulations for D_{Ala} where also made in the geometries of figure 33, 32, 30, and 31, with the exception of replacing alanine and the surrounding PMMA with water, as to represent removal of the alanine dosimeter holder. In the open ^{60}Co geometry, the source was modelled as a point source(source number = 1) positioned 100 cm from target, with a beam size of radius[15] = 5.6417 cm at target position.
In the closed ^{60}Co geometry, the source was modelled as an isotropic radiating disk of finite size(source number 3), surrounding the target, with inner radius = 10 cm, outer radius = 11 cm, and length = 4.8 cm. A material input file for the alanine dosimeters(PEGS4) was provided. It was made from the data of a elemental analyses of the alanine dosimeters, performed by DB Lab A/S, and the density was chosen to be its known value of 1.24 g/cm^3.

7.4.1 Results

The values of $(D_{Ala})_Q$, and $(D_W)_Q$, are given as the dose pr. history given to the region of interest(alanine or alanine ring), and are shown in table 7 with their uncertainties, which are the type A standard deviations of equation 82. The calculated H_{Q,Q_0}, of equation 65, are shown in table 8 with its uncertainty, which is found using error propagation:

$$\sigma_{F_{Q,Q_0}} = \sqrt{\sum_{i=1} \left(\frac{\partial}{\partial D_i} F_{Q,Q_0} \right)^2 \sigma_i^2} \tag{87}$$

$$= \sqrt{\frac{D_{Ala,Q}^2 \sigma_{W,Q_0}^2}{D_{Ala,Q_0}^2 D_{W,Q}^2} + \frac{D_{W,Q_0}^2 \sigma_{Ala,Q}^2}{D_{Ala,Q_0}^2 D_{W,Q}^2} + \frac{D_{Ala,Q}^2 D_{W,Q_0}^2 \sigma_{W,Q}^2}{D_{Ala,Q_0}^2 D_{W,Q}^4} + \frac{D_{Ala,Q}^2 D_{W,Q_0}^2 \sigma_{Ala,Q_0}^2}{D_{Ala,Q_0}^4 D_{W,Q}^2}} \tag{88}$$

Where σ_i is the standard deviation of D_i described in equation 82.

8 Analysis and Discussion

8.1 Cobalt Source Geometry Comparison

8.1.1 Uncertainty in Matching Reference Conditions

The calliper used for setting up the open geometry experiment resulting in a small type B uncertainty both in water tank placement, and SCD. This would only cause an insignificant change in the calibrated conversion factor $N_{D,W}$ as the energy fluence is insignificantly different from the reference conditions, and will not be included in further analysis.

[15] All experiments with the open ^{60}Co geometry and Varian Truebeam, had a beam size of 10 $\times$ 10 cm, but since dosrznrc operates in a cylindrical coordinate system, we choose a circular beam with area $100cm^2$.

Q	^{60}**Co**	**4X**	**6X**
$\boldsymbol{D_{Ala,\mathrm{OG1}}}$	$(1.068 \pm 0.003) \times 10^{-12}$	$(1.312 \pm 0.003) \times 10^{-12}$	$(1.444 \pm 0.003) \times 10^{-12}$
$\boldsymbol{D_{W,\mathrm{OG1}}}$	$(1.102 \pm 0.003) \times 10^{-12}$	$(1.360 \pm 0.004) \times 10^{-12}$	$(1.490 \pm 0.004) \times 10^{-12}$
$\boldsymbol{D_{Ala,\mathrm{OG2}}}$	$(1.0690 \pm 0.0005) \times 10^{-12}$	$(1.3184 \pm 0.0005) \times 10^{-12}$	$(1.4438 \pm 0.0006) \times 10^{-12}$
$\boldsymbol{D_{W,\mathrm{OG2}}}$	$(1.0962 \pm 0.0005) \times 10^{-12}$	$(1.3561 \pm 0.0006) \times 10^{-12}$	$(1.4868 \pm 0.0006) \times 10^{-12}$
$\boldsymbol{D_{Ala,\mathrm{CG1}}}$	$(2.529 \pm 0.010) \times 10^{-15}$	$(3.772 \pm 0.012) \times 10^{-15}$	$(3.942 \pm 0.012) \times 10^{-15}$
$\boldsymbol{D_{W,\mathrm{CG1}}}$	$(2.597 \pm 0.010) \times 10^{-15}$	$(3.812 \pm 0.012) \times 10^{-15}$	$(3.940 \pm 0.012) \times 10^{-15}$
$\boldsymbol{D_{Ala,\mathrm{CG2}}}$	$(2.547 \pm 0.002) \times 10^{-15}$	$(3.666 \pm 0.003) \times 10^{-15}$	$(3.689 \pm 0.003) \times 10^{-15}$
$\boldsymbol{D_{W,\mathrm{CG2}}}$	$(2.621 \pm 0.002) \times 10^{-15}$	$(3.684 \pm 0.003) \times 10^{-15}$	$(3.653 \pm 0.003) \times 10^{-15}$
Q	**10X**	**15X**	**18X**
$\boldsymbol{D_{Ala,\mathrm{OG1}}}$	$(2.198 \pm 0.010) \times 10^{-12}$	$(2.591 \pm 0.011) \times 10^{-12}$	$(3.121 \pm 0.012) \times 10^{-12}$
$\boldsymbol{D_{W,\mathrm{OG1}}}$	$(2.274 \pm 0.011) \times 10^{-12}$	$(2.674 \pm 0.012) \times 10^{-12}$	$(3.195 \pm 0.012) \times 10^{-12}$
$\boldsymbol{D_{Ala,\mathrm{OG2}}}$	$(2.2040 \pm 0.0017) \times 10^{-12}$	$(2.5721 \pm 0.0018) \times 10^{-12}$	$(3.0953 \pm 0.0019) \times 10^{-12}$
$\boldsymbol{D_{W,\mathrm{OG2}}}$	$(2.2710 \pm 0.0018) \times 10^{-12}$	$(2.6522 \pm 0.0019) \times 10^{-12}$	$(3.191 \pm 0.002) \times 10^{-12}$
$\boldsymbol{D_{Ala,\mathrm{CG1}}}$	$(5.08 \pm 0.02) \times 10^{-15}$	$(5.54 \pm 0.02) \times 10^{-15}$	$(5.83 \pm 0.02) \times 10^{-15}$
$\boldsymbol{D_{W,\mathrm{CG1}}}$	$(4.91 \pm 0.02) \times 10^{-15}$	$(5.34 \pm 0.02) \times 10^{-15}$	$(5.60 \pm 0.02) \times 10^{-15}$
$\boldsymbol{D_{Ala,\mathrm{CG2}}}$	$(4.534 \pm 0.006) \times 10^{-15}$	$(4.837 \pm 0.006) \times 10^{-15}$	$(5.116 \pm 0.006) \times 10^{-15}$
$\boldsymbol{D_{W,\mathrm{CG2}}}$	$(4.367 \pm 0.006) \times 10^{-15}$	$(4.718 \pm 0.006) \times 10^{-15}$	$(4.837 \pm 0.006) \times 10^{-15}$

Table 7: *This table shows the results of the dosrznrc particle transport simulations. All values shown are the dose pr. history, given to the region of interest(see figure 32, 33, 31, and 30) in Gy. The subscripts reference the details of the simulation in the following way:* ***OG*** *is the open geometry of figure 32, and 33.* ***CG*** *is the closed geometry of figure 31, and 30.* ***1*** *is the set up of figure 33, and 30, where the alanine is modelled as a single pellet in the center.* ***2*** *is the set up of figure 32, and 31, where the alanine is modelled as a cylindrical ring.*

Figure 28: *This figure show the geometry used in the flurznrc simulation of the open* ^{60}Co *source geometry. Red is air, blue is cobalt, yellow is a tungsten-nickel-copper alloy, and orange(small plate in front of the* ^{60}Co *source) is steel. The source was modelled as an isotropic radiating disk of finite size(source number 3), with dimensions matching the size and location of the blue cobalt. The simulation parameters used are as follows:* $ECUT = 521$ *keV,* $PCUT = 1$ *keV, and number of histories* $= 5 \times 10^8$*. The materials all had* $AE = 521$ *keV, and* $PE = 10$ *keV with the exception of alanine which had* $PE = 1$ *keV. The resulting spectrum was gathered from the region marked with P.*

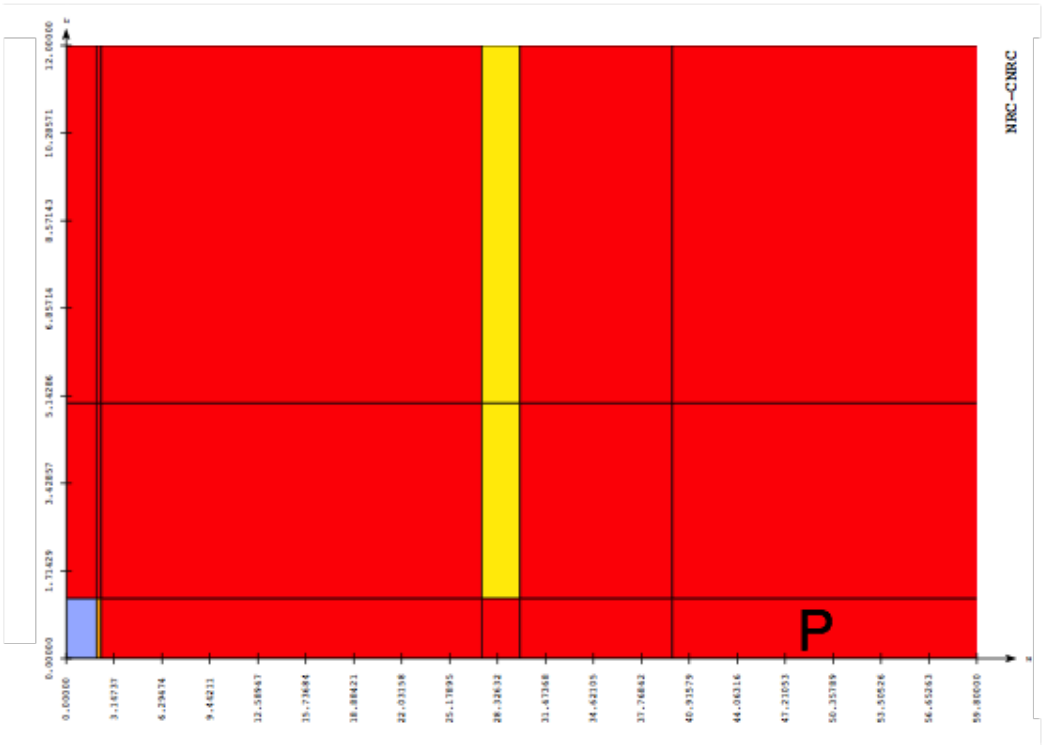

8.1.2 Background Calculations

30 second measurements of the un-irradiated Farmer chamber was made, who had the relative size of $M_0/M \sim 10^{-5}$, and will not be included in the analysis, as we argue that it is negligible small.

8.1.3 Asymmetrical EPR Readout

In the EPR readout procedure, the alanine dosimeter is turned manually as to detect asymmetries in the dosimeter signal. If there is a high deviation between before and after turning the dosimeter, then we discard the dosimeter as something has corrupted the signal. A corrupted signal could be coursed by being in contact with water, high temperature or magnetic dust particles(dropped on the floor). An alanine dosimeter from each of the two lowest dose batches in the open geometry, had a corrupted signal, and was removed from the analysis, remembering to change $N = 5$ for the uncertainty calculations.

Figure 29: *This figure show the geometry used in the flurznrc simulation of the closed* ^{60}Co *source geometry. Red is air, blue is cobalt, dark green is nylon, orange is steel, and green is PMMA. The source was modelled as an isotropic radiating disk of finite size(source number 3), with dimensions matching the size and location of the blue cobalt. The simulation parameters used are as follows:* $ECUT = 521$ *keV,* $PCUT = 1$ *keV, and number of histories* $= 5 \times 10^8$*. The materials all had* $AE = 521$ *keV, and* $PE = 10$ *keV. The resulting spectrum was gathered from the region marked with P.*

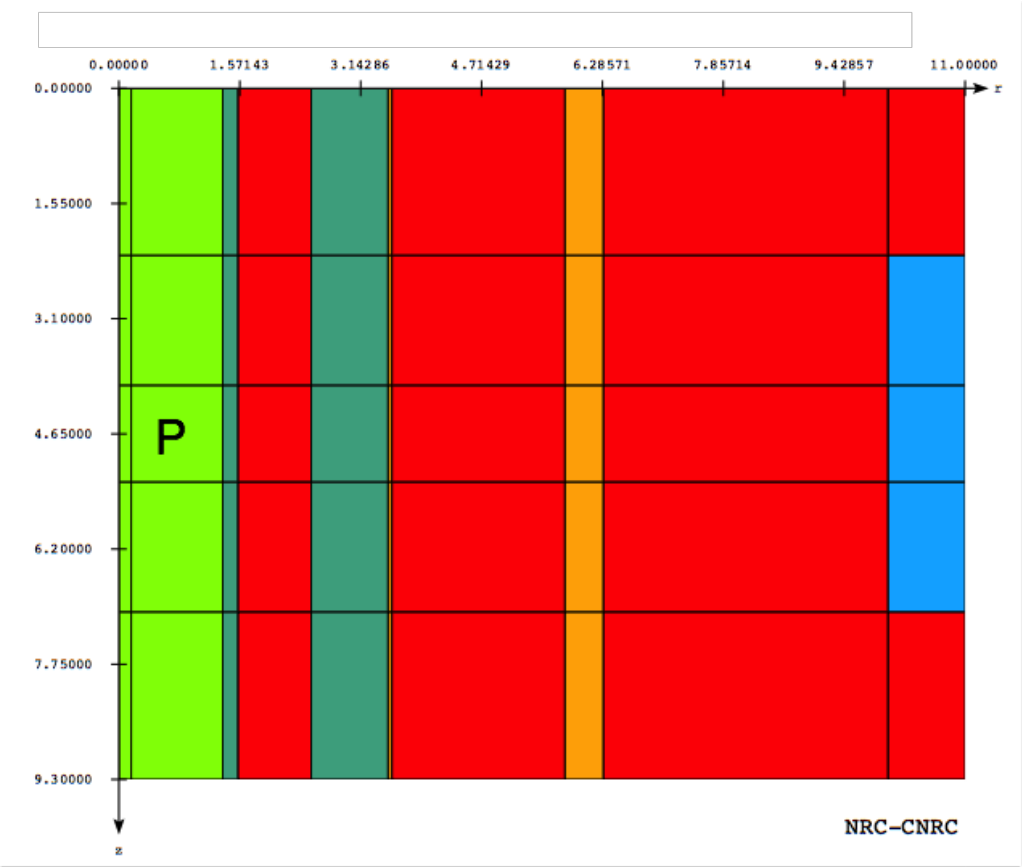

8.1.4 Calibration Uncertainties

We want to perform the χ^2 test on the linear calibration curve fit, to determine whether or not the linear model is good. For this we must choose the uncertainty correctly, using only contributions with errors that would distinguish the alanine batches from each other.

- **Open Geometry**. We can neglect the uncertainty associated with positioning the alignment telescope at SCD = 1000 mm, and positioning the water tank at the correct distance from source, as both were set at the beginning of the experiment and not moved before all irradiations of both alanine and ionisation chamber where complete[16]. Between the irradiation of each batch, the alanine holder had to po-

[16]This is not completely true as the alanine measurements were split over two days and both the alignment telescope and the water tank needed repositioning at the beginning of the next day. The uncertainties can still be neglected though, because the dose-rate used to calibrate the alanine batches, was found from ionisation chamber measurements made on the associated experiment day.

Figure 30: *This figure show the geometry used in the dosrznrc simulation of the closed* ^{60}Co *source geometry, and hypothetical MV-irradiations with a single central alanine pellet as the target. Red is air, blue is PMMA, and orange is alanine. The source was modelled as an isotropic radiating disk of finite size(source number 3), surrounding the target, with inner radius* $= 10$ *cm, outer radius* $= 11$ *cm, and length* $= 4.8$ *cm. The simulation parameters used are as follows:* $ECUT = 521$ *keV,* $PCUT = 1$ *keV, and number of histories* $= 1 - 5 \times 10^9$ *depending on source energy spectrum. The materials all had* $AE = 521$ *keV, and* $PE = 10$ *keV with the exception of alanine which had* $PE = 1$ *keV.*

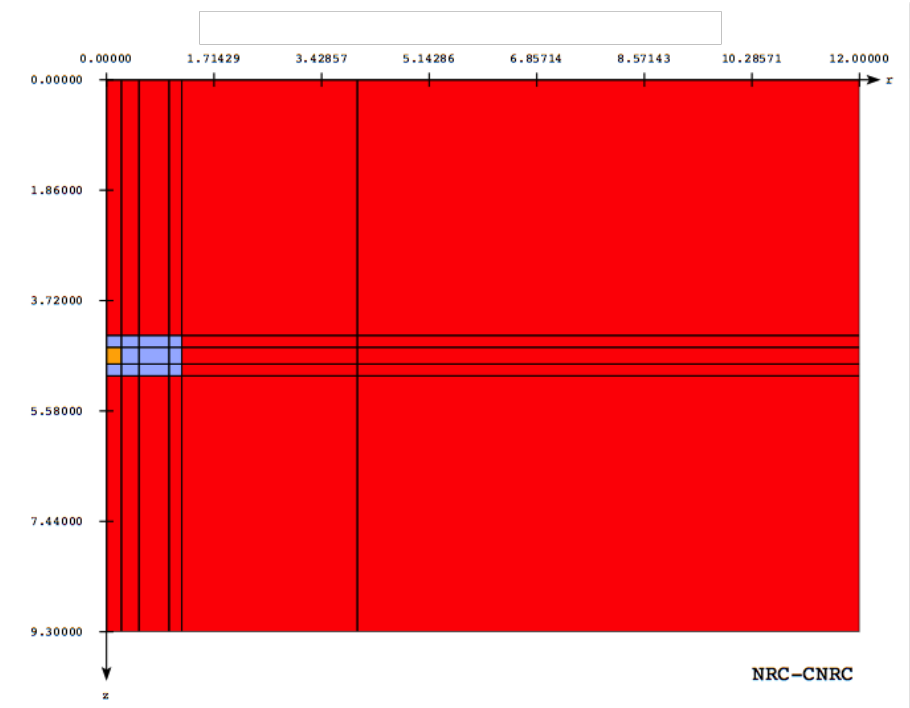

sitioned using the alignment telescope, see figure 19. The variance from repeated ion chamber positioning, gave an $u_A = \sigma_{rep\%} = 0.11\%$ uncertainty to the dose measurements associated with the dosimeter placement. σ_{rep} was calculated as

$$\sigma_{rep} = \sqrt{\frac{1}{N-1}\sum_{i=1}^{N}(\overline{M} - \overline{M}_i)^2} \tag{89}$$

Where $\bar{M}$ is the mean of all measurements made during the repeated ion chamber positioning, and $\bar{M}_i$ is mean of the measurements made for the i'th ion chamber positioning. When matching the alanine dosimeters effective measuring point, to the dose-rate of the ionisation chamber, the uncertainty contribution from dosimeter positioning is $\sqrt{2}\sigma_{rep}$, because both dosimeters are positioned the same way. There where not given time for the temperature of the alanine to acclimate to the phantom temperature, so we will add an uncertainty of $\pm 2°$, which converted to the signal creation uncertainty is $\sigma_{T,ala} = 0.28\%$ [21]. This add up to the uncertainty in the absorbed dose to water given to a single batch(x-axis uncertainty in figure 21):

$$\sigma_{D,W} = \sqrt{2\sigma_{rep}^2 + \sigma_{\dot{D}}^2 + \sigma_{T,ala}^2} \tag{90}$$

Figure 31: *This figure show the geometry used in the dosrznrc simulation of the closed* ^{60}Co *source geometry, and hypothetical MV-irradiations with a cylindrical ring of alanine as the target. Red is air, blue is PMMA, and orange is alanine. The source was modelled as a isotropic radiating disk of finite size(source number 3), surrounding the target, with inner radius* $= 10$ *cm, outer radius* $= 11$ *cm, and length* $= 4.8$ *cm. The simulation parameters used are as follows:* $ECUT = 521$ *keV,* $PCUT = 1$ *keV, and number of histories* $= 1 - 5 \times 10^9$ *depending on source energy spectrum. The materials all had* $AE = 521$ *keV, and* $PE = 10$ *keV with the exception of alanine which had* $PE = 1$ *keV.*

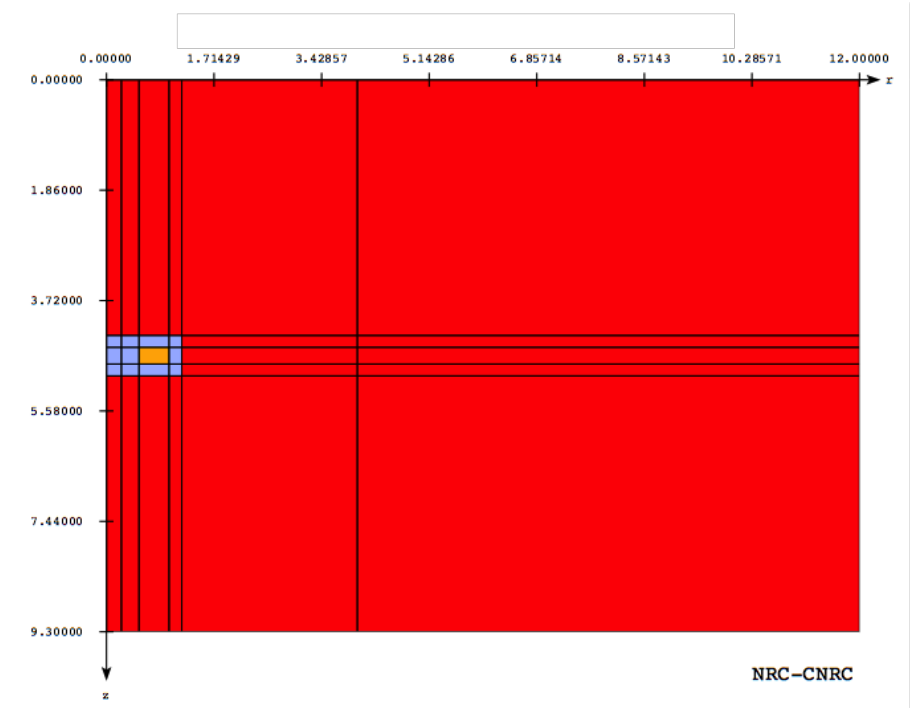

Where $\sigma_{\dot{D}}$ is the type A uncertainty shown in table 2 multiplied by the irradiation time.

The uncertainty associated with the mean readout of the six pellets in a single batch(σ_{EPR}), is the standard deviation of the 6 alanine dosimeters calculated as in equation 46. Since the pellets where readout one batch at a time in one sitting, we should add uncertainty contributions for system drift(0.1%) and temperature correction(0.3%) [22], as these could change the EPR readouts of all the alanine dosimeters in a batch, as they potentially would add a gradually increasing/decreasing error to the EPR readouts[17]. So the total uncertainty in the EPR readout of an entire batch is:

$$\sigma_{\text{EPR}} = \sqrt{(0.003^2 + 0.001^2)\overline{\text{P2P}}^2 + \frac{\sum_{i=1}(\overline{\text{P2P}} - \text{P2P}_i)^2}{N(N-1)}} \tag{91}$$

Where $N = 6$ is the number of pellets in each batch. For these errors the χ^2/n for the fit is 2.0, which for $n = 4$ which has the sampling probability of equation 52 to

[17]If all pellets where readout in random order, then we didn't need to include this as it would be included in the standard deviation of equation 46

Figure 32: *This figure show the geometry used in the dosrznrc simulation of the open* ^{60}Co *source geometry, and Varian Truebeam MV-irradiations with a single central alanine pellet as the target. Grey is vacuum, red is water, blue is PMMA, and orange is alanine. The source was modelled as a point source(source number 1) located 100 cm from target, with beam size radius* $= 5.6417$ *cm at target. The simulation parameters used are as follows:* $ECUT = 521$ *keV,* $PCUT = 1$ *keV, and number of histories* $= 1 - 5 \times 10^9$ *depending on source energy spectrum. The materials all had* $AE = 521$ *keV, and* $PE = 10$ *keV with the exception of alanine which had* $PE = 1$ *keV.*

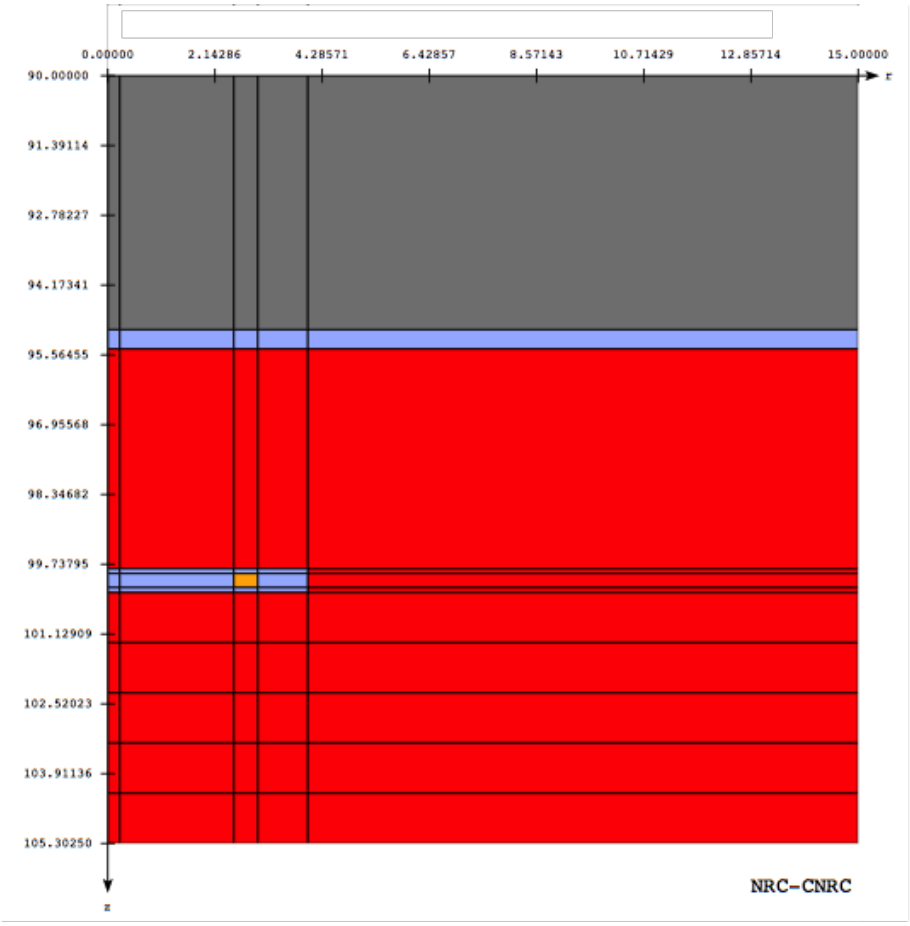

be $> 5\%$, so we see no reason to reject the fit as a valid calibration curve.

- **Closed geometry**, The uncertainty in the dose-rate given to a single batch is given for gamma cell 1 in [21] as 0.53%, which is the combination of ^{60}Co decay, irradiation time, transient dose, and irradiation geometry. This could potentially be higher for doses below 7 Gy, as the lowest dose used to calibrate Gammacell 1 was 7 Gy. We should be able to neglect the irradiation temperature correction, as the pellets spend at least 30 min in a heating cabinet set at 21° before irradiation, so identical irradiation temperature is expected. As for the readout uncertainty, all batches where readout on the same day, so we use σ_{EPR} of equation 91 with $N = 4$. This give a χ^2/n of 14, which is too high for a reliable model, so we look at the unscaled residuals, calculated as $\overline{\text{P2P}} - fit$, in figure 34. It seems that the

Figure 33: *This figure show the geometry used in the dosrznrc simulation of the open* ^{60}Co *source geometry, and Varian Truebeam MV-irradiations with a cylindrical ring of alanine as the target. Grey is vacuum, red is water, blue is PMMA, and orange is alanine. The source was modelled as a point source(source number 1) located 100 cm from target, with beam size radius* $= 5.6417$ *cm at target. The simulation parameters used are as follows:* $ECUT = 521$ *keV,* $PCUT = 1$ *keV, and number of histories* $= 1-5\times10^9$ *depending on source energy spectrum. The materials all had* $AE = 521$ *keV, and* $PE = 10$ *keV with the exception of alanine which had* $PE = 1$ *keV.*

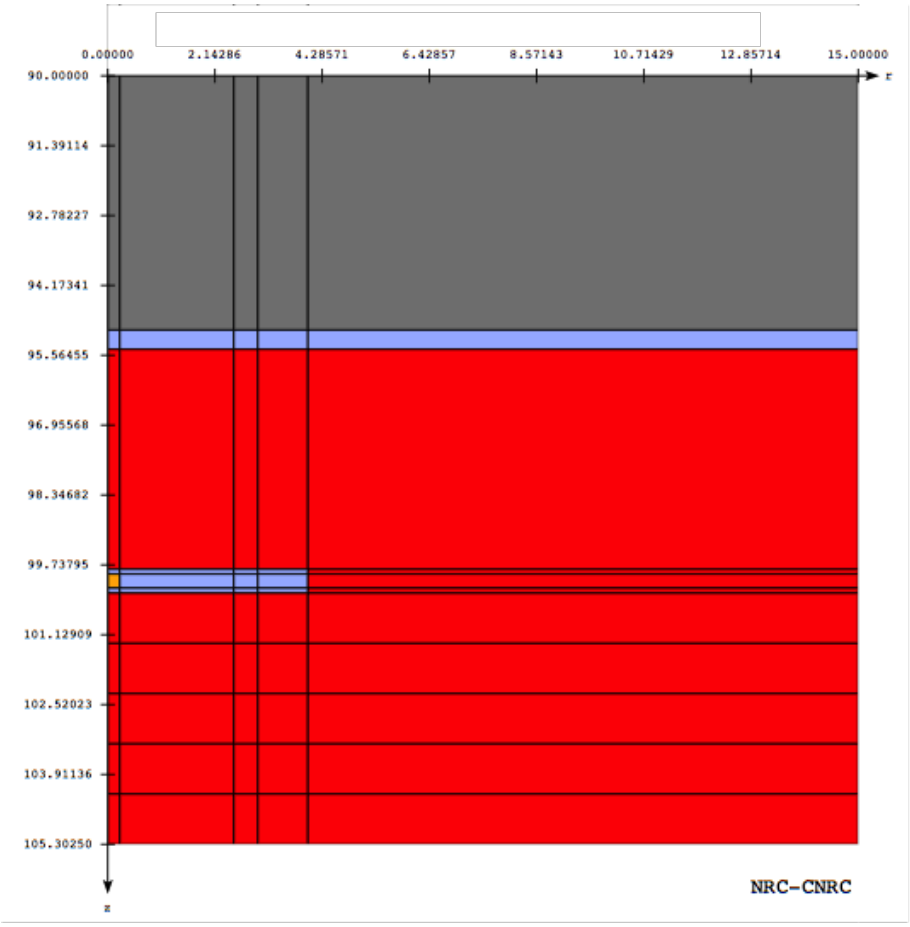

used uncertainties where a lot smaller than the errors they represent, especially for the low doses. But this is not caused by the EPR-readout, as can be seen in the residuals of figure 22, the precision, represented as the uncertainty in EPR readout, of each batch is high, but the accuracy, represented as the uncertainty in the dose-rate, is not.

We could argue for removing the outlying pellet readout of the lowest dose batch in figure 22 using Chuvnets criteria, but it would only change χ^2/n to 13.2, so we keep it, as high noise to signal ratio it expected for doses below 2 Gy [6] [30] [22]. We will instead conclude that the dose-rate uncertainty of gammacell 1 is higher than expected for low dose irradiations.

Q	^{60}**Co**	**4X**	**6X**
$\boldsymbol{H_{Q,\mathrm{OG1}}}$	1.000 ± 0.006	$(9.95 \pm 0.06) \times 10^{-1}$	1.000 ± 0.006
$\boldsymbol{H_{Q,\mathrm{OG2}}}$	1.0000 ± 0.0010	$(9.969 \pm 0.009) \times 10^{-1}$	$(9.958 \pm 0.009) \times 10^{-1}$
$\boldsymbol{H_{Q,\mathrm{CG1}}}$	1.000 ± 0.007	1.016 ± 0.007	1.027 ± 0.007
$\boldsymbol{H_{Q,\mathrm{CG2}}}$	1.000 ± 0.002	1.024 ± 0.002	1.039 ± 0.002
Q	**10X**	**15X**	**18X**
$\boldsymbol{H_{Q,\mathrm{OG1}}}$	$(9.97 \pm 0.08) \times 10^{-1}$	$(9.99 \pm 0.07) \times 10^{-1}$	1.007 ± 0.007
$\boldsymbol{H_{Q,\mathrm{OG2}}}$	$(9.952 \pm 0.013) \times 10^{-1}$	$(9.945 \pm 0.012) \times 10^{-1}$	$(9.948 \pm 0.011) \times 10^{-1}$
$\boldsymbol{H_{Q,\mathrm{CG1}}}$	1.063 ± 0.008	1.066 ± 0.008	1.070 ± 0.008
$\boldsymbol{H_{Q,\mathrm{CG2}}}$	1.068 ± 0.002	1.055 ± 0.002	1.088 ± 0.002

Table 8: *This table shows the calculated H_Q factors of equation 65, using the data of table 7. The subscripts reference the details of the simulation in the following way:* ***OG*** *is the open geometry of figure 32, and 33.* ***CG*** *is the closed geometry of figure 31, and 30.* ***1*** *is the set up of figure 33, and 30, where the alanine is modelled as a single pellet in the center.* ***2*** *is the set up of figure 32, and 31, where the alanine is modelled as a cylindrical ring. The errors are type A, and calculated with equation 88.*

Figure 34: *This figure shows the unscaled fit residuals, of the close geometry calibration curve. each data point is the mean value of a batch, and the error bars are the standard deviation of the four alanine dosimeters in the batch calculated as in equation 46*

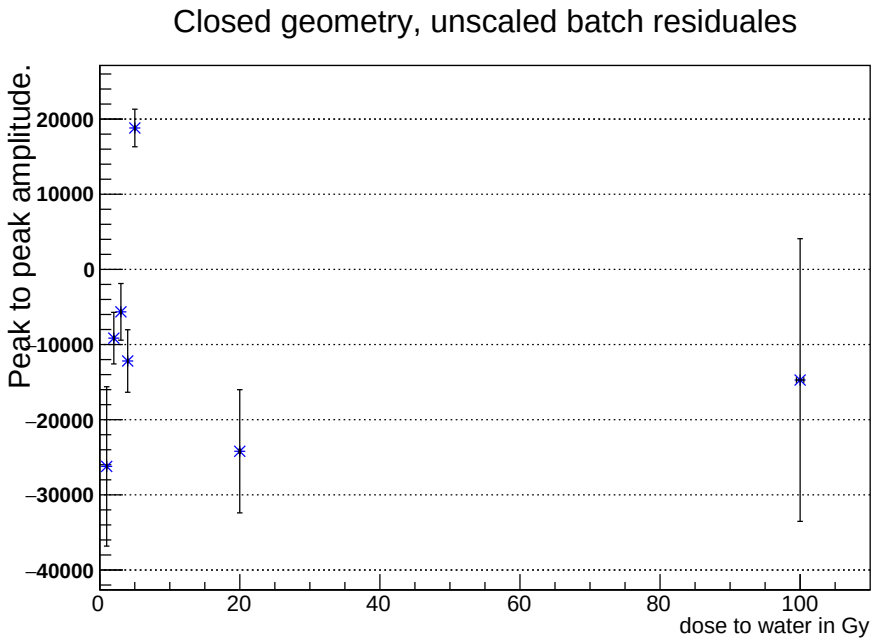

8.1.5 Dose Determination Uncertainty

When determining the dose to water given to a alanine pellet, using the calibration curve as described in the algorithm of section 4.4, the uncertainty is the combination of the

following sources:

- Traceability to the primary standard, is an uncertainty of 1.32% to the primary standard of PTB, for the closed geometry calibration, as given by the transfer-alanine calibration of gammacell 1 [22].
  For the open geometry calibration, the traceability is an uncertainty of 0.25% to the primary standard of NPL. The 0.25% is from the Farmer chambers calibration certificate. Both are type B and can be neglected when comparing values found with the same calibration curve.

- Uncertainty in the calibration curve. This would be the uncertainty in the slope of the calibration curve, which was found during the fit to be 0.4% for the open geometry, and 0.6% for the closed geometry

- The uncertainty in A_{ref} used in the algorithm of section 4.4. A_{ref} is chosen as the mean spectrum of the batch with the highest dose in the used calibration curve. so σ_{ref} is the standard deviation of the batch as calculated in equation 46 and converted to dose through error propagation of the calibration curve fit. Corrections for system drift and temperature are not needed as the calibration curve is scaled to the new readout of A_{ref} see section 4.4.

- The EPR readout uncertainty for A. All the pellets that we analyse in this thesis using calibration curves, are given doses in the range of $20 - 30$ Gy, so to find a measure for the single pellet readout uncertainty(σ_A) we repeatedly readout a alanine dosimeter, given 22 Gy, for $N = 10$ iterations in a single sitting. The pellet was removed and inserted in the quartz tube before each readout, and the EPR was also re-tuned. This gave a type A standard deviation of 1.1% calculated as

$$\sigma_A = \sqrt{\frac{\sum_{i=1}^{N}(\overline{\mathrm{P2P}} - \mathrm{P2P}_i)^2}{N-1}} \tag{92}$$

  With $N = 10$. We then add type B contributions from mass determination(0.3%), and irradiation temperature(0.28%)[18] [22]

$$\sigma_{A'} = \sqrt{(0.003^2 + 0.0028^2)\overline{\mathrm{P2P}}^2 + \sigma_A^2} \tag{93}$$

  The σ_A uncertainty is a useful estimate when we look a single alanine dosimeter, but when we are interested in the mean absorbed dose given to a batch, we exchange σ_A and mass determination with the standard deviation for the alanine dosimeters in the batch:

$$\sigma_{A'} = \sqrt{(0.0028^2)\overline{\mathrm{P2P}}^2 + \frac{\sum_{i=1}^{N}(\overline{\mathrm{P2P}} - \mathrm{P2P}_i)^2}{N-1}} \tag{94}$$

  $\sigma_{A'}$ is converted to dose through error propagation of the calibration curve fit.

[18] We dont add a contribution for the day to day stability as A and A_{ref} are read out in the same sitting.

For a single alanine dosimeter traceable to a primary standard, this give a combined uncertainty of 1.3% for the open geometry, and 1.9% for the closed geometry. For a batch, not including the traceability, we get:

$$\sqrt{(0.6\%)^2 + \frac{\sum_{i=1}^{N}(\overline{\text{P2P}} - \text{P2P}_i)^2}{N-1}}, \quad \sqrt{(0.7\%)^2 + \frac{\sum_{i=1}^{N}(\overline{\text{P2P}} - \text{P2P}_i)^2}{N-1}} \tag{95}$$

For the open- and closed geometry respectively.

8.1.6 Geometry Comparison

To determine which ^{60}Co source geometry, that is preferable for developing the alanine dosimetry system, we look at the following parameters, where the main issue is to make a calibration used for auditing MV-beams in Danish hospitals:

- **Uncertainty**. The doses of alanine pellets will be limited by the calibration curve used to determine the dose, so it is important to have as low a uncertainty as possible. When comparing alanine dosimeters the traceability uncertainty is not needed, and in that case the open geometry is only slightly better than the closed geometry, due to lower uncertainty in the dose-rate. For doses in the low end of the clinical dose-range, the relative dose-rate uncertainty seems to be getting even higher for the closed geometry. For determining the dose traceable to a primary standard, the open geometry is much better, because it is calibrated by ion chamber, and the closed geometry is calibrated by transfer alanine.

- **Matching reference conditions**. The calibration is only valid for determining the absorbed dose of the same effective measuring point, as the one used for making the calibration curve. It is therefore preferable that the calibration is made under reference conditions that are chosen at DTU, for example is it the exact same alanine holder, that is used in the MV-beam irradiations as in the open ^{60}Co irradiations. Whereas for the closed geometry, we should attempt to recreate the reference conditions used for the transfer alanine irradiations. Bottom line is that, in the open geometry, we can make the calibrations reference conditions, match the reference conditions of a certain auditing method.

- **Reproducibility**. To have a long lasting alanine dosimetry system at DTU Risø, the calibration curve should be reproducible for a recalibration, to keep up to date with new pellets, new phantoms, and signal decay(as we read out old alanine dosimeters as A_{ref} along with the new A). This is easier with the closed geometry as all the preparation needed, is acclimating the pellet temperature. It should be noted that the gammacell also should be recalibrated with a few years interval, but that is already being done as it is also used for other dosimetric purposes.

The open ^{60}Co source geometry is favoured as the best to develop the alanine dosimetry system.

8.2 Alanine Energy Dependence

8.2.1 Background Calculations

30 seconds measurements of un-irradiated Farmer chamber were made. the irradiation of the various MV-photon beams take 10 - 20 seconds, but relative size was found to be $M_0/M \sim 10^{-5}$ so we didn't include it in the analysis.

8.2.2 Monitor Chamber

The resolution of the monitor chamber readings, where worse than for the Farmer chamber, so if all was fine then we could expect identical readings for all irradiations made with the same photon energy. This was investigated and confirmed, so the monitor chamber readings will not be included in the further analysis.

8.2.3 Asymmetrical EPR readout

A single alanine dosimeter in the 4X irradiated batch had a corrupted signal and was discarded from the analysis.

8.2.4 Polarity Deviation

In the MV-beam experiments of 24/05-2016, The polarity correction factors k_{pol} in 10 and 20 cm depth(see table 3), showed only a relative deviation of:

$$\frac{|[k_{pol,10}]_Q - [k_{pol,20}]_Q|}{[k_{pol,10}]_Q} < 0.0004 = 0.04\% \tag{96}$$

For the used photon beams: 6X, 10X, and 18X. We choose therefore to only find the polarity correction factor for the 10 cm depth in the follow up experiment on 23/06-2016.

8.2.5 Temperature Interpolation

During the experiments with the MV-beam the signal to the thermometers in the water tank(T1 and T2) would cut out randomly, meaning that not all measurements had a temperature reading. For the experiments performed on 24/05-2016 the resolution of the thermometers was $\pm 0.1^\circ$, and showed no trend in change of temperature above fluctuations of $u_B = 0.08^\circ$, so the missing temperatures were given the mean value. For the experiments performed on 23/06-2016, this was solved by interpolating the temperature readings using a data fit. We choose the errors to be ± 1 in the last digit of the temperature reading($\pm 0.01^\circ$). Inspired by Newtons cooling law, we first fitted with a three parameter exponential, see figure 35:

$$f_1(x) = p_0 + p_1 e^{-p_2 x} \tag{97}$$

Which gave a χ^2/n of 0.42 for T1, and 0.54 for T2, which is "too good" a value, meaning that we probably overestimated errors. We made a Runs test which gave a significance of 4.8σ for T1, and 5.2σ for T2, so we tested various polynomial fits, and choose a third degree polynomial, see figure 36:

$$f_2(x) = p_0 + p_1 x + p_2 x^2 + p_3 x^3 \tag{98}$$

This time we got 2.9σ for T1, and 3σ for T2, even though this should reject the fit as a reliable model, we argue that it is reliable for a few reasons:

- The resolution of the data is given to the closest $0.01°$, so in the flattening region of figure 36(22:30 - 23:30 time of day), the data arranges itself in the shape of steps, which would give less runs than if the resolution was better.
- The functions we fitted with contained few parameters, meaning they should model a simple process, however during the experiments, dosimeters where repeatedly lowered and raised from the water thereby giving small increases/decreases in temperature. Therefore small peaks in the temperature should be expected, which would decrease the number of runs.
- A change in temperature between the lowest($19.98°$), and highest($20.77°$) value, would only change k_{TP}, of equation 70, about $\sim 0.3\%$.
- With T2 as example, the expected number of runs was $\langle r \rangle = 87 \pm 6.5$, and the measured number of runs was 68. so with the arguments above 68 seems to be a fair number of runs, especially with the visually pleasing match of data and model.

Figure 35: *This figure shows one of the two thermometers readings, taken during the MV-beam experiments performed on 23/06-2016. the date is fitted with a three parameter exponential function.*

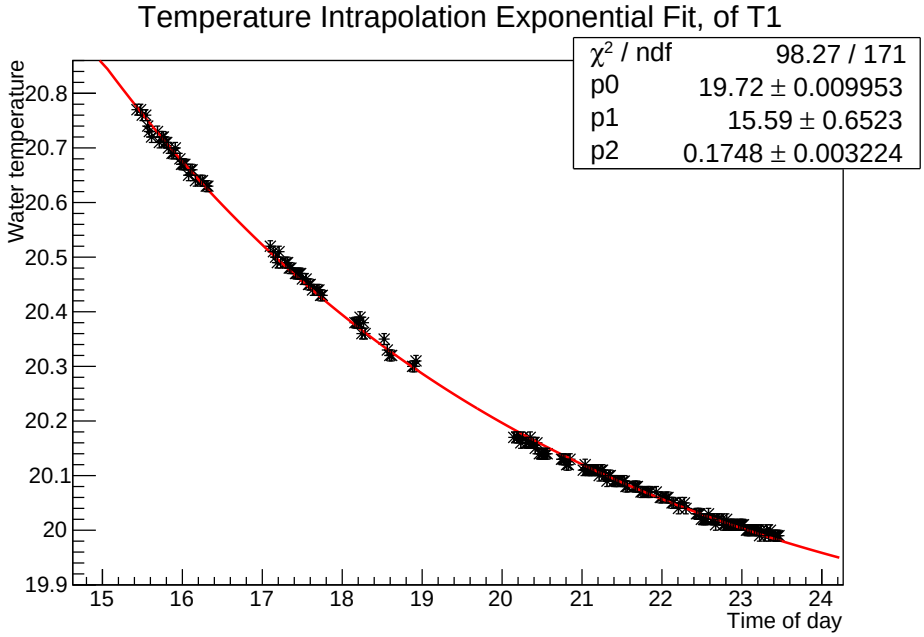

8.2.6 $\mathrm{TPR}_{20,10}$ Uncertainty

The beam quality index $\mathrm{TPR}_{20,10}$ is the ratio between $Mk_{\mathrm{TP}}k_sk_{pol}$ in 20 cm water and 10 cm water as described in section 8.2.6. If there was a small systematic offset in the water depths then, the caused error would be negligible as the distance between the two measurements would still be 10 cm, however, an error in the 10 cm distance between

Figure 36: *This figure shows one of the two thermometers readings, taken during the MV-beam experiments performed on 23/06-2016. The date is fitted with a third degree polynomial.*

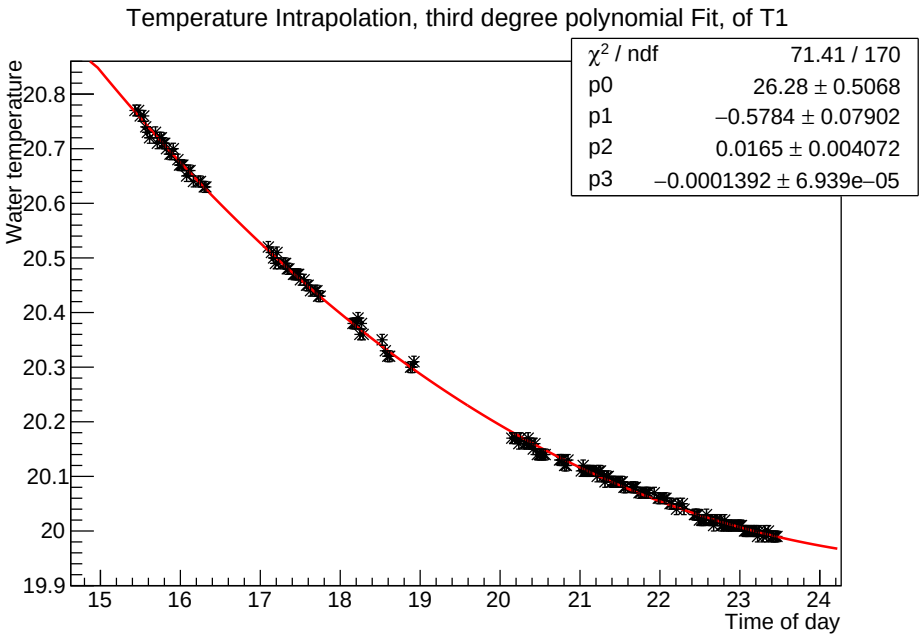

measurements must be added to the $\text{TPR}_{20,10}$ uncertainty.

We estimated the uncertainty of positioning the water tank at a given depth to be $u_B = \sigma_x = 0.5mm$, so the dose at both depths receives the associated uncertainty. If we use the approximation that for a mono energetic photon beam $D \propto e^{-(\mu_{en}/\rho)x}$, then error propagation gives us

$$\sigma = \left|\frac{\partial}{\partial x}D(x)\right|\sigma_x = \left(\frac{\mu_{en}(E)}{\rho}\right)_W D\sigma_x \tag{99}$$

For a non-mono energetic beam we must weight according to the energy fluence:

$$\sigma_{\%} = \frac{\sigma}{D} = \int_0^{E_{max}} \Psi_{norm}(E,x)\left(\frac{\mu_{en}(E)}{\rho}\right)_W dE\sigma_x \tag{100}$$

The energy fluence must represent the spectra of figure 23 after travelling a distance x_d in water, so using mass energy absorption and mass attenuation coefficients for water, and the spectra in figure 23, we calculate σ/D, with the energy fluence:

$$\Psi_{norm}(E,x_d) = \frac{\Psi(E,0)e^{-\left(\frac{\mu(E)}{\rho}\right)_W x_d}}{\int_0^{E_{max}}\Psi(E,0)e^{-\left(\frac{\mu(E)}{\rho}\right)_W x_d}dE} \tag{101}$$

And find the highest uncertainty as 0.14% for 4X in 10 cm depth, and the lowest uncertainty as 0.09% for 18X in 20 cm depth. They are added in quadrature to the type A standard deviation for repeated measurements of M:

$$\sigma_M^2 = (M\sigma_{\%})^2 + \frac{\sum_{i=1}^{N}(M-M_i)^2}{N(N-1)} \tag{102}$$

Error propagation is then used to add uncertainty from correction factors and σ_M to $\text{TPR}_{20,10}$, and they are shown in table 5. For the experiments made on 23/06-2016, the same value for k_{pol} was used in depths 10 and 20 cm, and was therefore not used to calculating $\text{TPR}_{20,10}$.

8.2.7 k_Q Factors.

The calculated k_Q values for ionisation chamber FC65-G is listed in [24](table 14, with the name Scdx-Wellhofer IC 70 Farmer). To get as accurate values as possible, we fit a third degree polynomial(f_Q) to the data in the range of $\text{TPR}_{20,10}$ = 0.62 - 0.8. The uncertainty to each data point is set to $u_B = 1\%$ from appendix 2 in [24], see figure 37. The uncertainties are not independent for each data point, so would would not be usable

Figure 37: *This figure shows the calculated k_Q values for the FC65-G Farmer chamber, taken from [24](table 14, with the name Scdx-Wellhofer IC 70 Farmer). A third degree polynomial is fitted to the data to interpolate intermediate values.*

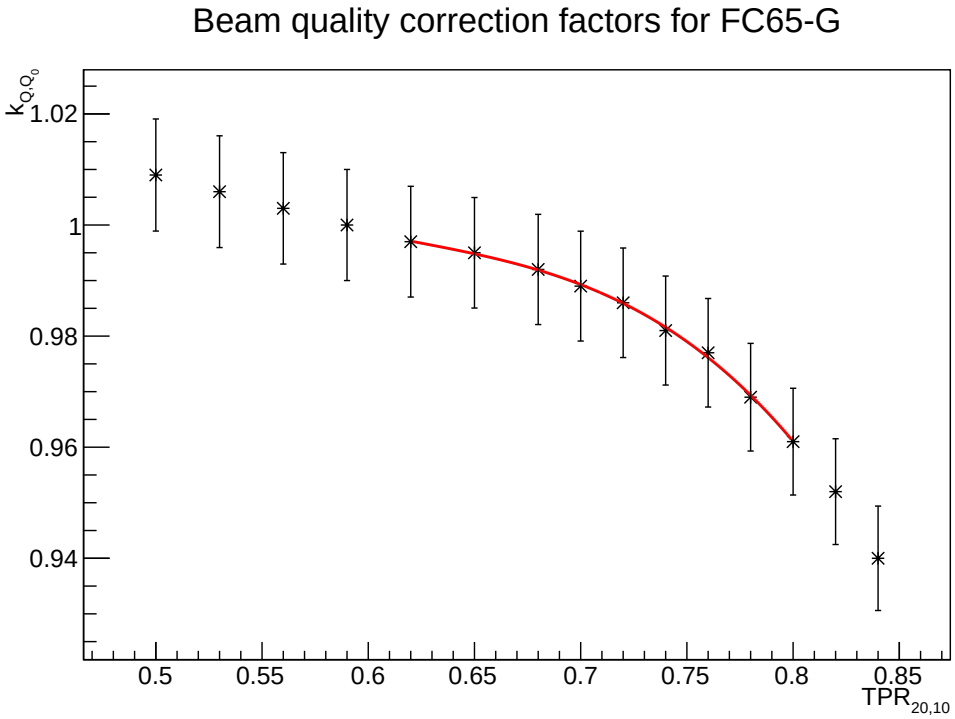

for the χ^2-test, and we will instead use the Runs test to determine the goodness of fit:

$$\langle r \rangle = 5 \pm 1, \quad r = 6 \tag{103}$$

The Runs test give no reason to reject the fit[19], so we use it to find the k_Q factors for the values in table 5.
The combined uncertainty of the k_Q from $u_B = 1\%$ and $\text{TPR}_{20,10}$ is found as $\sqrt{u_B^2 + \sigma_{f,\text{TPR}}^2}$,

[19]Normally if the Runs test gave $r > \langle r \rangle$ with a high z, then it could be that the fit contained too many parameters, and needed simplification.

where $\sigma_{f,\mathrm{TPR}}$ is found from error propagation:

$$\sigma_{f,\mathrm{TPR}} = \sqrt{\left(\frac{\partial}{\partial(\mathrm{TPR}_{20,10})} f_Q(\mathrm{TPR}_{20,10})\right)^2 \sigma^2_{\mathrm{TPR}_{20,10}}} \tag{104}$$

Where $\sigma_{\mathrm{TPR}_{20,10}}$ are taken from table 5.

8.2.8 Vertical Water Tank Placement

Between each alanine batch irradiation, the water tank was lowered down to make it possible to position the alanine holder, with the alignment telescope. This repeated movement could hypothetically change the distance between the source and the water tank. To investigate the effect this could have on the dose-rate at SAD, the Farmer chamber was fixed at the SAD and the water tank was lowered and raised 9 times while two 100 MU irradiations 6X where performed for each iteration. This gave only a 0.009% extra uncertainty calculated as:

$$\sigma = \frac{\sqrt{\sigma^2_{wt} - \sigma^2_M}}{M} \tag{105}$$

Where σ_{wt} is the standard deviation pr. measurement, of the measurements performed during the iterations:

$$\sigma^2_{wt} = \frac{\sum_{i=1}^{N}(\overline{M} - M_i)^2}{N-1} \tag{106}$$

where M_i is the mean of the two measurements performed at the i'th iteration, and $N = 9$. σ_M is the standard deviation pr. measurement, for both Farmer chamber and water tank at fixed positions, calculated as as in equation 106, but where M_i is a single measurement. 0.009% is little compared to the other sources of uncertainty, and will therefore not be included in further calculations.

8.2.9 F_{Q,Q_0}

We want to calculate the energy dependence for alanine $F_{Q,Q_0} = \frac{D^c}{D}$, by taking the ratio of absorbed doses to water, found from alanine dosimeters(D^c) and Farmer chamber measurements(D). The alanine dosimeters where readout as described in section 4.4. For D, we use the dose-rates and uncertainties of table 6. Since we are assuming that both dosimeters are measuring the same dose-rate, we have to add an uncertainty associated with the positioning of their effective measuring points. This was done using the alignment telescope which we know gave a type A 0.11% uncertainty for each positioning, so for positioning both alanine and Farmer chamber at the same spot, the error becomes $\sqrt{2} \times 0.11\%$. The uncertainties of the alanine readouts where found as described in section 8.1.5. We are using the open geometry, that was calibrated using the same Farmer chamber as the doses we are comparing, so we can neglect the 0.5% traceability uncertainty. This add up to a EPR readout uncertainty pr. batch as in equation 95, where N is the number of pellets in the batch. The calculated F_{Q,Q_0} are shown shown in table 9.

When we plot the energy dependence factors as functions of $\mathrm{TPR}_{20,10}$, (see figure 38)

Q	F_Q (24/05-2016)	F_Q (23/06-2016)	F_Q (23/06-2016)
4X		9.98	
6X	1.000	9.97	1.001
10X	9.90	9.98	
15X		9.96	9.93
18X	9.86	9.93	

Table 9: *This table shows the calculated F_Q factors from experimental data for alanine dosimeters, using Farmer chamber measurements as the known dose-rate. At the experiment made 23/06-2016 the photon spectra of $4X$ and $6X$ was used to irradiate two alanine batches each instead of one, the results from the extra batch is shown in the third column. The uncertainty is* $\pm 1.3\%$.

we see that any possible trend deviating from unity is shadowed by the error bars of the uncertainty, for which the dominating sources are the Farmer chambers k_Q and the EPR-readout. It is tempting to use the high precision to explain a decreasing trend for $\text{TPR}_{20,10} > 0.72$, yet this could easily be caused by the error in k_Q. In figure 39 we see the comparison of experimental and calculated k_Q for an ionisation chamber for which [24] comment *"A small, progressive decrease in the values for k_Q at high energies can be seen when PMMA sleeves of thickness 1 mm, 0.5 mm and no sleeve at all are used in the calculation of p_{wall} "*, this could be the reason that a small trend is showing. Beyond that, the values in table 9 line up perfectly, within the uncertainty, to the data collected by Waldeland in figure 14 [48]. For better results, we should have found the Farmer chambers k_Q values experimentally instead of using calculated values, as this would reduce the uncertainty.

Figure 38: *This figure show the experimental energy dependence factor F_Q of equation 65.* the relative uncertainties are 1.2%

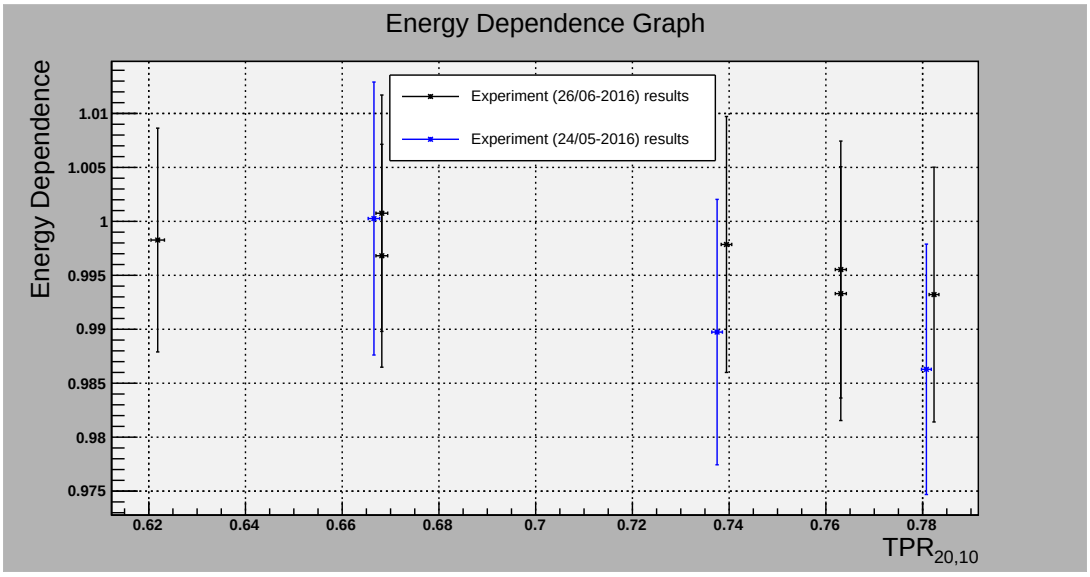

Figure 39: *This figure was taken from page 184 in [24], and shows both experimental(dotted, dashed, and solid lines) and calculated(round dots) k_Q values for a NE 2571 ionisation chamber. It shows how the individuality of an ionisation chamber can shape the energy dependence. The dashed, dotted, and solid lines represent the ionisation chamber with no PMMA sleeve, 1 mm PMMA sleeve, and 0.5 mm PMMA sleeve respectively.*

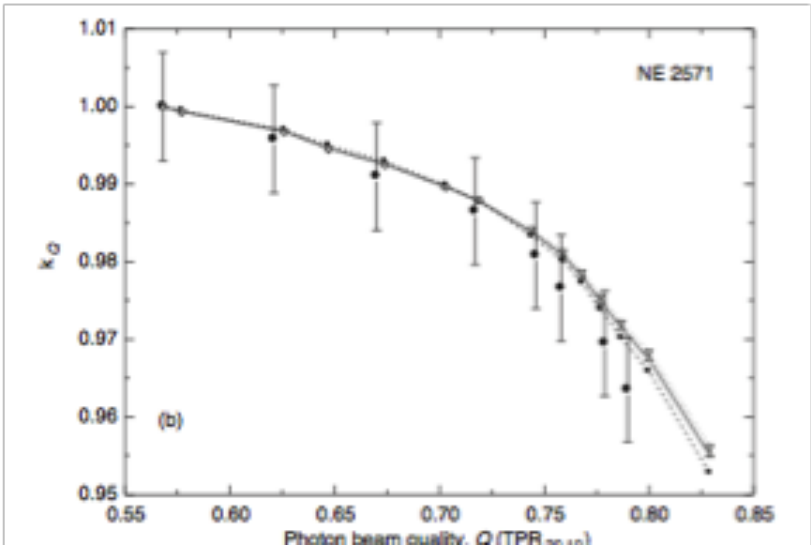

8.2.10 H_{Q,Q_0}

The energy absoption energy dependence factor H_{Q,Q_0} is calculated as in equation 65, using the results from the Monte Carlo simulations, and are shown in table 8. To make better comparisons, we plot them in figure 40. The observation we make is that the uncertainties are a lot smaller for the alanine ring model, this is because the alanine region was a lot bigger for the ring than the single pellet, so more particle histories would deposit energy in the region. The second observation we make is that for the open geometry there is a $z = 1.7$ difference in H_Q between the two alanine models for 18X. To find out if the data show a difference in energy dependence between the two alanine models, we set the null hypothesis to be that there is no difference between them, and, inspired by the data of the ring model, we assume a one parameter constant fit. This gave a $\chi^2/n = 0.74$, so these data does not indicate a difference in energy absorption energy dependence between the two alanine models, which motivate that the data represents the physical pellet set up of 6 pellets placed in a circumference 20. The fit indicated a constant energy absorption energy dependence for MV-beams, which is similar to the results of [50] who finds a constant energy dependence of 0.994 for MV-beams with nominal energies between $6-25$ MV, [9] who finds a constant energy dependence 0.992 ± 0.005 for nominal energy $10-30$ MV.

Due to the design of the alanine holder in figure 20, depending on how tight the lid is screwed on there could be a small amount of air in front of the pellets during the irradiation, so to investigate if this had any effect on H_Q we performed similar simulations in the open geometry of figure 33 and 32, with the only difference being 0.55 mm of air between the alanine pellet and the PMMA lid. The results are shown in table 10, and plotted together with the other open geometry results in figure 41. Again the uncertainty

Figure 40: *This figure shows the values of the simulated H_Q of table 8. the assigned beam qualities, are the experimentally found beam qualities of table 5.* OG is the open geometry, CG is the closed geometry, 1 is the single pellet model for alanine, and 2 is the ring model for alanine.

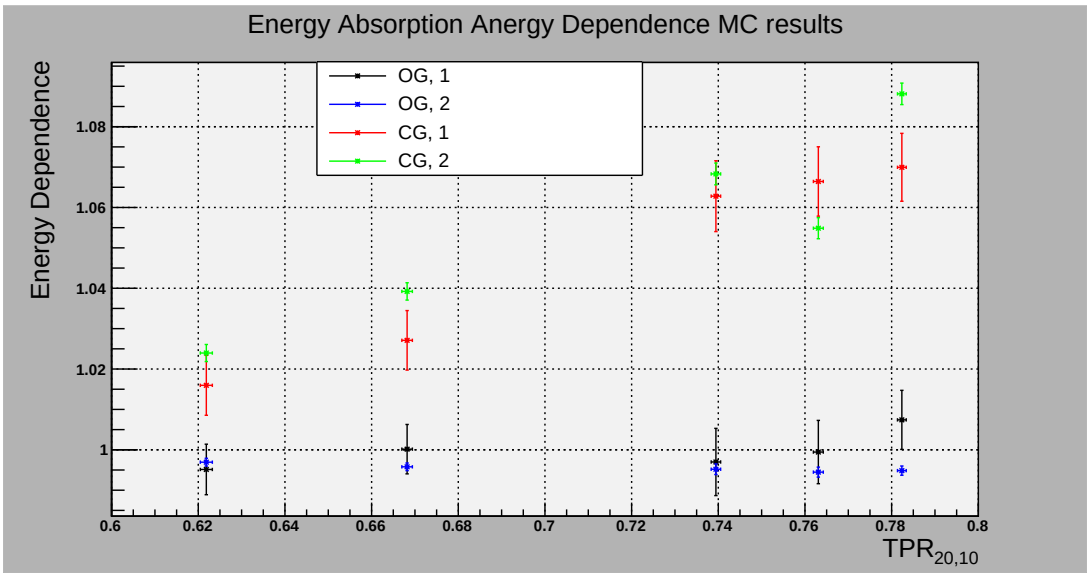

for the singular pellet model is too high for the scope of interest, so we will focus on the ring model. The data shows an almost consistently higher energy dependence for the data with air in front of the alanine, which is unlikely if we assume a null hypothesis of no difference in the energy dependence between air and no air. Instead of performing a Runs test, we will simply find the probability of obtaining these data by chance, if we assume that there is a 50% chance for either result to be higher than the other. We represent each of the five beam qualities as a coin toss, where heads(n) represent the data point, with no air, as being larger than the data point with air, and tails($N-n$) as the opposite. this follows the binomial distribution:

$$P(n,N) = \frac{N!}{n!(N-n)!}p^n(1-p)^{N-n} \quad \Rightarrow \quad P(1,5) + P(0,5) = 0.188 = 18.8\% \quad (107)$$

Which mean that it is not unlikely, and we can't reject the null hypothesis, that the pocket of air have no impact on the energy dependence. We therefore assume the four datasets in figure 41 represents the same value, so we make a constant fit, a linear fit and a second degree polynomial fit, and obtain the following χ^2/n values respectively: 0.95, 0.86, and 0.87. As the $\chi^2/n < 1$ we should favour the model with least parameters: the constant fit at $H_Q = 0.9961$, and we see that smaller uncertainties are needed for detecting a possible trend in the beam quality[20]. the $H_Q = 0.9961$ value should be taken as unique to the reference conditions of the performed experiments, as a different alanine dosimeter placement or different phantom material could effect the energy dependence, as seen in the closed geometry results of figure 40

The Monte Carlo simulations of the closed geometry, is a non-physical situation as the

[20]a constant fit of only the two ring model datasets(blue and green) in figure 41 gave a χ^2/n of 1.01, for $H_Q = 0.9961$

Figure 41: *This figure shows the simulated H_Q values for both the open geometry with 0.55 mm air in front of the alanine dosimeters, and without.*

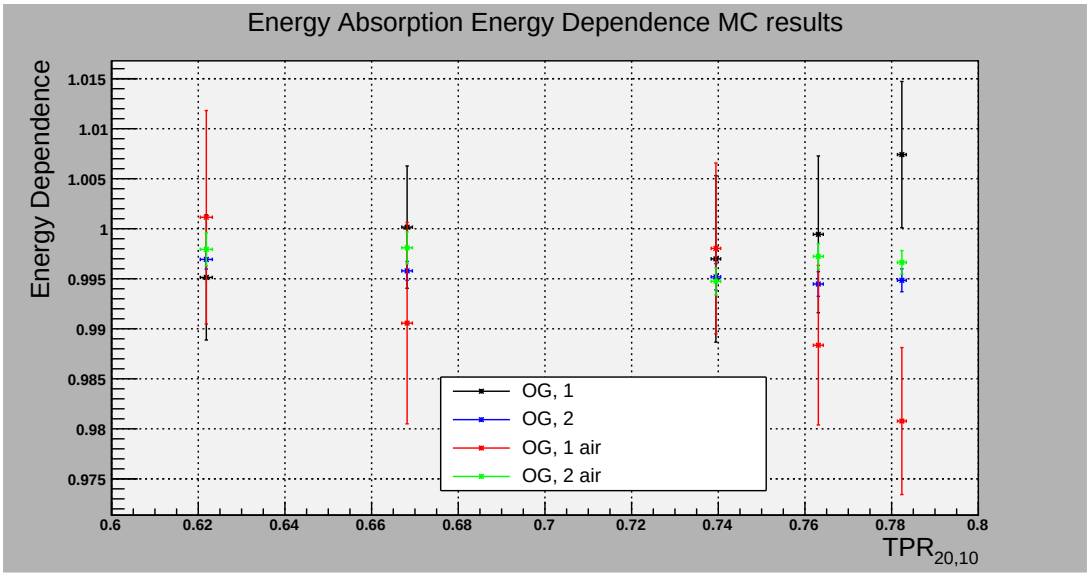

source was modelled to be an isotropic radiating ring of finite size, emitting the photon spectra of figure 23, that being said, it is still interesting to look at how the energy dependence, depend on a uniform radiation field, as opposed to a radiation beam. In figure 40, we see that H_Q in the closed geometry has an increasing trend in the beam quality, of course the spectra at the dosimeter region are different from the open geometry, as there is only air between the source and PMMA alanine holder, this would effect the restricted mass stopping power ratios of alanine and water, which make up the H_{Q,Q_0}:

$$H_{Q,Q_0} = \frac{(D_{Ala}/D_W)_Q}{(D_{Ala}/D_W)_{Q_0}} = \frac{N_{D,Ala,Q}/N_{D,W,Q}}{N_{D,Ala,Q_0}/D_{D,Ala,Q_0}} = \frac{(s_{Ala,air})_Q/(s_{W,air})_Q}{(s_{Ala,air})_{Q_0}/(s_{W,air})_{Q_0}} \tag{108}$$

Where $(s_{med,cav})_Q$ is the Spencer-Attix relation of equation 41 for the photon energy spectrum of Q. To know if the high energy dependence is caused by the non-physical source, the lack of a phantom, or uniform irradiation field, more simulations are needed, and the uniform radiation field could the experimentally tested by having the Varian Truebeam irradiate while turning around the alanine dosimeters and ionisation chamber.

We see no reason to investigate a value for G_Q, for two reasons: **1.** the uncertainties are too big to detect a deviation from unity in F_Q/H_Q. **2.** Results in literature show that the ionisation density effect of G_Q is non-negligible for ion-beams, and that the soft collision limitation to free radical creation is relevant for x-rays with nominalle energies below 100 kV [36] [23]. There is therefore no expected effect of G_Q in MV-photon beams.

8.3 Possibility of Audits

The goal of using alanine dosimeters for auditing clinical photon beams, has been attempted since [40](1982) and [44](1996), because alanine-EPR dosimetry have the following favourable aspects as a transfer dosimeter :

Q	^{60}Co	4X	6X
$H_{Q,^{60}\mathrm{Co},\mathrm{OG1}}$	1.000 ± 0.007	1.001 ± 0.010	$(9.91 \pm 0.10) \times 10^{-1}$
$H_{Q,^{60}\mathrm{Co},\mathrm{OG2}}$	1.0000 ± 0.0010	$(9.979 \pm 0.016) \times 10^{-1}$	$(9.981 \pm 0.015) \times 10^{-1}$
Q	10X	15X	18X
$H_{Q,^{60}\mathrm{Co},\mathrm{OG1}}$	$(9.98 \pm 0.08) \times 10^{-1}$	$(9.88 \pm 0.07) \times 10^{-1}$	$(9.81 \pm 0.07) \times 10^{-1}$
$H_{Q,^{60}\mathrm{Co},\mathrm{OG2}}$	$(9.947 \pm 0.013) \times 10^{-1}$	$(9.972 \pm 0.012) \times 10^{-1}$	$(9.966 \pm 0.011) \times 10^{-1}$

Table 10: *This table shows the calculated $H_{Q,^{60}\mathrm{Co}}$ factors of equation 65, using data from simulations almost identical to the the ones described in figure 32, and 33, but with 0.55 mm of air in front of the alanine pellets. The subscripts reference the details of the simulation in the following way:* ***1*** *is the set up of figure 33, and 30, where the alanine is modelled as a single pellet in the center.* ***2*** *is the set up of figure 32, and 31, where the alanine is modelled as a cylindrical ring. The errors are type A, and calculated with equation 88.*

- **Long lasting signal**, the alanine dosimeters can be readout multiple times, without destroying the signal. And the signal decay is small and understood.
- **Cumulative properties**, the alanine dosimeters can be given repeated doses, that cumulated to the total dose being represented by the signal. This opens the possibility of alanine being used as a personal dosimeters of a radiotherapy patient, which could be included in the patient file [30].
- **Low energy dependence** , as also shown in this thesis, the energy dependence is small and wouldn't change significantly depending on the beam quality. This would make intercomparisons between radiations of beam quality non-problematic.
- **Easy procedure**, the set up of the reference conditions needed for the irradiations, is potentially very simple as there is no need to find an abundance of correction factors, as with ionisation chambers, only the irradiation temperature. If the reference conditions require a solid phantom, then it could potentially be transferred together with the alanine dosimeters.
- **Tissue like density**, alanine has a tissue equivalent density(the pellets used in this thesis has $\rho = 1.22 g/cm^3$), so they don't perturb the beam for the remaining set up. This mean we could have multiple alanine dosimeters in a single irradiation.
- **Non-toxic**, alanine is not toxic for the human body, so they could easily be placed "inside" the body of a patient during irradiation.

8.3.1 Current Clinical Applications of Alanine

Alanine is already being used as an auditing tool for clinical photon beams [15]. In [17] they show that alanine can be used as an independent auditing tool for Intensity modulated radio therapy(IMRT) given by Helical Temotherapy on special phantoms of different shape. The following publications show some of the progress towards the usage of alanine-EPR dosimeters in medical physics:

- **De Angelis**(2005) [3]. A pilot program at ISS(National Institute of health in Italy) where alanine pellets where irradiated to 10 Gy in a water tank phantom and a special anatomical phantom, at 16 Italian Radiotherapy centers. The pellet where sent back for comparison. they conclude that alanine-EPR dosimetry is feasible as postal transfer auditing tool complimenting to the TLD system. In [37](2006) they argument for TLD together with alanine, because TLD's have lower uncertainty for doses ~ 1 Gy.

- **Rech**(2014) [39]. In vivo test of alanine dosimeters, as a dose verifier for patients diagnosed with gynaecological cancer, undergoing 3-D external beam radiation therapy. 4 patients undergoing 20 irradiation sessions gave 220 irradiated alanine dosimeters. Compared to identical irradiations made in a anatomical phantom, they conclude that the alanine dosimeters showed the correct dose was given to the patients(within the allowed uncertainties, as determined by the ICRU, for the tumour in question).

- **Wagner**(2011) [47]. in vivo test of alanine dosimeters, as dose verifier for patients with head and neck cancer undergoing IMRT. A special mouthpiece containing alanine dosimeters, was placed in the patients mouths during each irradiation, thereby obtaining the accumulated dose of the entire treatment. The accumulated dose was compared to the dose expected by the treatment planning system. Five patients participated in the study.

8.3.2 Risø's Alanine Dosimetry System for Auditing Clinical Photon Beams

Using the results of this thesis, and the methods described in literature, we will now propose how the Risø could develop the alanine dosimetry system for auditing clinical photon beams in Danish hospitals. The audit should be able to verify the two following properties of the photon beam:

1. **The dose-rate**. Under certain reference conditions, the photon beam should deliver a known dose-rate within some uncertainty. Too high a dose or too low, both have fatal consequences, and must therefore be audited often, and preferable by multiple independent methods.

2. **The dose distribution**. In IMRT the beam intensity is modulated while the photon beam is turning around the patient, to minimise the absorbed dose given to radiation sensitive body parts like the spinal cord. The instructions is calculated by the treatment planning system. This is a highly complicated system and must be tested often, to make sure it distributes the dose as expected.

A special phantom is designed for both audits. For the dose-rates audit the phantom should be of simple geometry, with room for positioning either alanine dosimeters, or an ionisation chamber. The dosimeter should, when placed in the phantom, be inside a wall with density thickness $5 g/cm^2$, to match the reference conditions of the Farmer chamber calibration. The phantom material should be a solid water-like material(PMMA, solid water, etc.) to match the reference conditions of the Farmer chamber calibration. The correction factor for using a different phantom material can be found for alanine with

Monte Carle simulations as in [46], and for ionisation chambers with experiments [29]. The calibration is then performed similarly to the open ^{60}Co source geometry calibration, with a solid phantom instead of a water tank. Using the energy dependence correction factors for alanine, it is now possible to detect deviations in the dose-rate of clinical photon beams, by irradiating the special phantom. The relative uncertainty goes down for higher dose, and more alanine dosimeters in a irradiation batch. Inspired by De Angelis [3] we could choose 10 Gy irradiations, 6 alanine dosimeters pr. batch. For the dose distribution audit, the phantom should be asymmetrical, as to test the treatment planing system, and it should have alanine dosimeters placed at multiple positions, so the dose distribution can be measured. The Varian Truebeam, located at Risø, would calibrate the phantom by irradiating the phantom with a certain dose distribution using the treatment planning system. During such an audit, both the phantom and alanine dosimeters would arrive by shipping to Danish hospitals, their treatment planning system should then replicate the phantom irradiation made at Risø. This would make the Varian Truebeam at Risø act like a secondary standard for treatment planning precision.

The alanine calibration used for the dose-rate audit, would be traceable to the primary standard used in the Farmer chamber calibration, and for a known irradiation temperature, and a dozen batches(to decrease the calibration fit uncertainty), the traceable batch uncertainty in the absorbed dose to water, should reach $\sqrt{(0.5\%)^2 + \frac{\sum_{i=1}^{N}(\overline{\mathrm{P2P}}-\mathrm{P2P}_i)^2}{N-1}}$, where the second term under the square root is the readout precision of a batch with N alanine dosimeters, which for $N = 6$ is about 0.45% for a absorbed dose of 10 Gy as shown in figure 42. This would give a traceable relative uncertainty of 0.7%, which is less than 1% and therefore sensitive enough for auditing clinical photon beams at hospitals. The alanine calibration of the dose distribution audit is traceable to the treatment planning system calibration of the Varian Truebeam, which is not as sensitive as the dose-rate calibration, but we argue that it is the dose-distribution and not the dose-rate that is the quantity of interest in this audit procedure.

9 Conclusion

We sought out to answer the three key questions, and have found the following answers:

We made two alanine calibrations, one for each ^{60}Co source, with different effective measuring points. We found that the open ^{60}Co source geometry is better to establish the alanine dosimetry than the closed ^{60}Co source geometry, because we found a total uncertainty of 1.3% pr. alanine dosimeter, for the open ^{60}Co source geometry, and 1.9% pr. alanine dosimeter for the closed ^{60}Co source geometry,traceable to the primary standard of NPL and PTB respectively. Also the open ^{60}Co source geometry, has the possibility of matching the calibration reference conditions to a specific auditing procedure, like the phantom and effective measuring point.

We performed multiple alanine and ionisation chamber irradiations in a water phantom, using the Varian Truebeam at DTU Risø, for the same effective measuring point as used in the open ^{60}Co source geometry calibration irradiations. Using calculated k_Q

Figure 42: *This figure shows the relative uncertainties of the 6 dosimeter batch precision, of the open* ^{60}Co *source calibration irradiations, as calculated in equation 46 .*

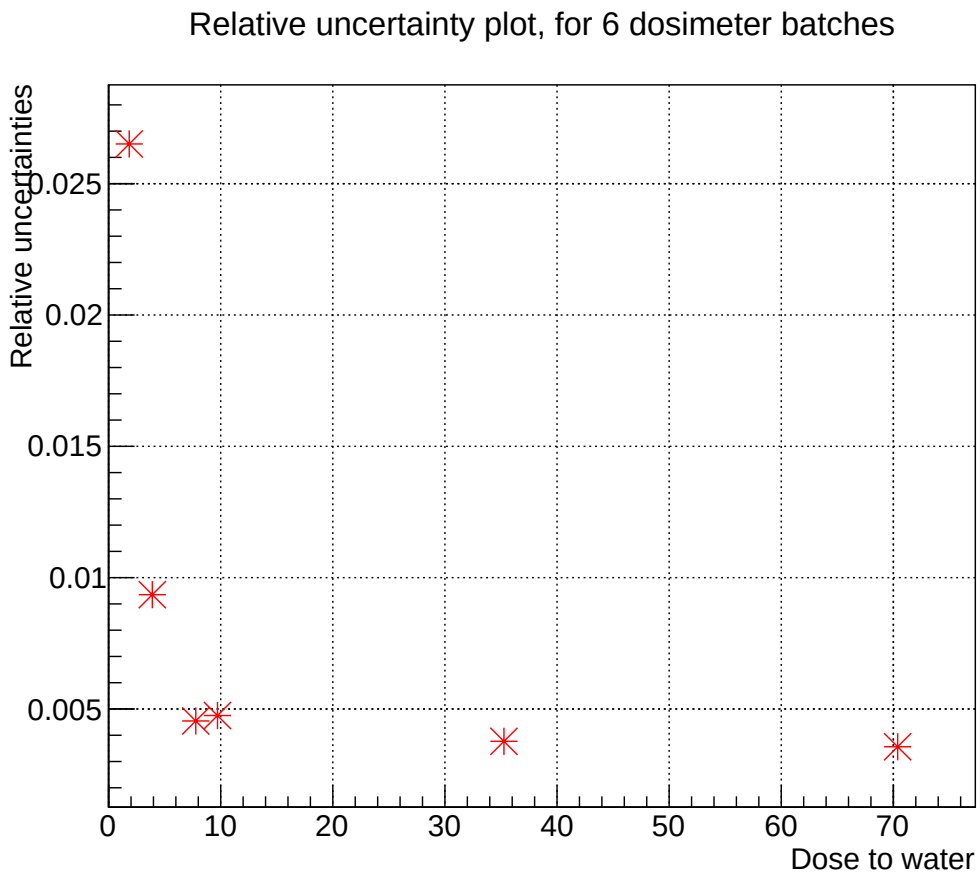

values for the ionisation chamber and the open source alanine calibration, we obtained experimental energy dependence factors F_Q for photon energy spectra with nominal energies 4, 6, 10, 15, and 18 MV. F_Q was found with a 1.1% uncertainty, which was not enough to detect any trend as a function of beam quality. If the ionisation chambers k_Q values where determined experimentally, the uncertainty in F_Q would decrease.

We performed Monte Carlo experiments of particle transport, in set ups matching the performed irradiation experiments, to find the ratio of absorbed doses H_Q. Several models for the best way of representing the experiments in the cylindrical geometry of egsNRC, gave results that deviated insignificantly from each-other, so we feel confident that the results represent the performed irradiation experiments. The H_Q values, for the open geometry, could not reject a constant dependence on beam quality, with value $H_Q = 0.9961$, which matches results found in literature. We argue that the constant value depends on the reference conditions of the irradiation, especially the phantom material and alanine dosimeter placement.

A procedure for setting up an alanine-transfer audit for clinical photon beams at Danish hospitals is described. Alanine is calibrated in special phantoms using the open ^{60}Co source to get a traceable relative uncertainty of theoretically 0.7%, and Varian Truebeam

linear accelerator, traceable to the primary standard of a calibrated Farmer chamber, and calibration of the treatment planing system of the Varian Truebeam.

References

[1] Helene Aget and Jean Claude Rosenwald. Polarity effect for various ionization chambers with multiple irradiation conditions in electron beams. *Medical Physics*, 18(1):67–72, 1991.

[2] E S M Ali and D W O Rogers. Functional forms for photon spectra of clinical linacs. *Physics in Medicine and Biology*, 57(1):31, 2012.

[3] C. De Angelis, V. De Coste, P. Fattibene, S. Onori, and E. Petetti. Use of alanine for dosimetry intercomparisons among italian radiotherapy centers. *Applied Radiation and Isotopes*, 62(2):261 – 265, 2005. Proceedings of the 6th International Symposium on {ESR} Dosimetry and Applications.

[4] M Anton and L Büermann. Relative response of the alanine dosimeter to medium energy x-rays. *Physics in Medicine and Biology*, 60(15):6113, 2015.

[5] M Anton, R-P Kapsch, A Krauss, P von Voigts-Rhetz, K Zink, and M McEwen. Difference in the relative response of the alanine dosimeter to megavoltage x-ray and electron beams. *Physics in Medicine and Biology*, 58(10):3259, 2013.

[6] Mathias Anton. Uncertainties in alanine/esr dosimetry at the physikalisch-technische bundesanstalt. *Physics in Medicine and Biology*, 51(21):5419, 2006.

[7] R. J. Barlow. *Statistics: A Guide to the Use of Statistical Methods in the Physical Sciences (Manchester Physics Series)*. Wiley, 1989.

[8] Martin J. Berger. Monte Carlo calculation of the penetration and diffusion of fast charged particles. 1963.

[9] Eva Stabell Bergstrand, Ken R Shortt, Carl K Ross, and Eli Olaug Hole. An investigation of the photon energy dependence of the epr alanine dosimetry system. *Physics in Medicine and Biology*, 48(12):1753, 2003.

[10] Stephen Blundell. *Magnetism in Condensed Matter (Oxford Master Series in Physics)*. Oxford University Press, 2001.

[11] J. W. Boag. Ionization measurements at very high intensities—part i. *The British Journal of Radiology*, 23(274):601–611, 1950. PMID: 14777875.

[12] J. W. Boag and J. Currant. Current collection and ionic recombination in small cylindrical ionization chambers exposed to pulsed radiation. *The British Journal of Radiology*, 53(629):471–478, 1980. PMID: 7388281.

[13] Herman Cember and Thomas Johnson. *Introduction to Health Physics: Fourth Edition*. McGraw-Hill Education / Medical, 2008.

[14] Glen Cowan. *Statistical Data Analysis (Oxford Science Publications)*. Clarendon Press, 1998.

[15] Schaeken B Cuypers R Lelie S Schroeyers W Schreurs S Janssens H Verellen DEmner. Implementation of alanine/epr as transfer dosimetry system in a radiotherapy audit programme in belgium. *Radiotherapy and oncology*, 2011.

[16] G. X. Ding, D. W. O. Rogers, and T. R. Mackie. Calculation of stopping-power ratios using realistic clinical electron beams. *Medical Physics*, 22(5):489–501, 1995.

[17] S Duane, D Nicholas, H Palmans, B Schaeken, J Sephton, P Sharpe, R Thomas, M Tomsej, K Tournel, D Verellen, and S Vynckier. Su-ff-t-195: Dosimetry audit for tomotherapy using alanine/epr. *Medical Physics*, 33(6):2093–2094, 2006.

[18] Christopher J. Foot. *Atomic Physics (Oxford Master Series in Atomic, Optical and Laser Physics)*. Oxford University Press, 2005.

[19] David Griffiths. *Introduction to quantum mechanics*. Pearson Prentice Hall, Upper Saddle River, NJ, 2005.

[20] David Griffiths. *Introduction to elementary particles*. Wiley-VCH, Weinheim Germany, 2008.

[21] Jakob Helt-Hansen. Emxmicro uncertainty estimates. *unpuplished*, 2013.

[22] Jakob Helt-Hansen, Flemming Rosendal, Inger Matilde Kofoed, and Claus Erik Andersen. Medical reference dosimetry using epr measurements of alanine: Development of an improved method for clinical dose levels. *Acta Oncologica*, 48(2):216 – 222, 2009.

[23] Rochus Herrmann, Steffen Greilich, Leszek Grzanka, and Niels Bassler. Amorphous track predictions in 'libamtrack' for alanine relative effectiveness in ion beams. *Radiation Measurements*, 46(12):1551 – 1553, 2011. Proceedings of the 16th Solid State Dosimetry Conference , September 19-24 , Sydney , Australia.

[24] INTERNATIONAL ATOMIC ENERGY AGENCY. *Absorbed Dose Determination in External Beam Radiotherapy*. Number 398 in Technical Reports Series. INTERNATIONAL ATOMIC ENERGY AGENCY, Vienna, 2005.

[25] INTERNATIONAL ATOMIC ENERGY AGENCY. *Radiation Oncology Physics*. INTERNATIONAL ATOMIC ENERGY AGENCY, Vienna, 2005.

[26] I. Kawrakow, E. Mainegra-Hing, D. W. O. Rogers, F. Tessier, and B. R. B. Walters. The EGSnrc code system: Monte Carlo simulation of electron and photon transport. Technical Report PIRS-701, National Research Council Canada, 2015.

[27] Iwan Kawrakow and Alex F Bielajew. On the condensed history technique for electron transport. *Nuclear Instruments and Methods in Physics Research Section B: Beam Interactions with Materials and Atoms*, 142(3):253–280, 1998.

[28] C Legrand, G H Hartmann, and C P Karger. Experimental determination of the effective point of measurement and the displacement correction factor for cylindrical ionization chambers in a 6 mv photon beam. *Physics in Medicine and Biology*, 57(21):6869, 2012.

[29] Lizhong Liu, Satish C Prasad, and Daniel A Bassano. Evaluation of two water-equivalent phantom materials for output calibration of photon and electron beams. *Medical Dosimetry*, 28(4):267 – 269, 2003.

[30] Kishor Mehta and Reinhard Girzikowsky. Esr dosimetry and applications: Proceedings of the 4th international symposium alanine-esr dosimetry for radiotherapy iaea experience. *Applied Radiation and Isotopes*, 47(11):1189 – 1191, 1996.

[31] Ichiro Miyagawa and Walter Gordy. Electron spin resonance of an irradiated single crystal of alanine: Second-order effects in free radical resonances. *The Journal of Chemical Physics*, 32(1):255–263, 1960.

[32] J. W. MOTZ, HAAKON A. OLSEN, and H. W. KOCH. Pair production by photons. *Rev. Mod. Phys.*, 41:581–639, Oct 1969.

[33] Vitaly Yu Nagy and Marc F Desrosiers. Complex time dependence of the epr signal of irradiated l-α-alanine. *Applied Radiation and Isotopes*, 47(8):789 – 793, 1996.

[34] Walter R Nelson, H Hirayama, and David W O Rogers. *The EGS4 code system*. SLAC, Stanford, CA, 1985.

[35] K. A. Olive et al. Review of Particle Physics. *Chin. Phys.*, C38:090001, 2014.

[36] P. Olko. Calculation of the relative effectiveness of alanine detectors to x rays and heavy charged particles using microdosimetric one-hit detector model. *Radiation Protection Dosimetry*, 84(1-4):63–66, 1999.

[37] S. Onori, E. Bortolin, A. Calicchia, A. Carosi, C. De Angelis, and S. Grande. Use of commercial alanine and tl dosemeters for dosimetry intercomparisons among italian radiotherapy centres. *Radiation Protection Dosimetry*, 120(1-4):226–229, 2006.

[38] Chester R. Ramsey, Kelly M. Spencer, and Adrian L. Oliver. Ionization chamber, electrometer, linear accelerator, field size, and energy dependence of the polarity effect in electron dosimetry. *Medical Physics*, 26(2):214–219, 1999.

[39] Amanda Burg Rech, Gustavo Lazzaro Barbi, Luiz Henrique Almeida Ventura, Flavio Silva Guimarães, Harley Francisco Oliveira, and Oswaldo Baffa. In vivo dose evaluation during gynaecological radiotherapy using l-alanine/esr dosimetry. *Radiation Protection Dosimetry*, 159(1-4):194–198, 2014.

[40] D.F. Regulla and U. Deffner. Dosimetry by esr spectroscopy of alanine. *The International Journal of Applied Radiation and Isotopes*, 33(11):1101 – 1114, 1982.

[41] Francis Weston Sears Hugh D. Young Roger A. Freedman, A. Lewis Ford. *University Physics with Modern Physics*. Pearson, 2011.

[42] C K Ross, K R Shortt, M Saravi, A Meghzifene, V M Tovar, R A Barbosa, C N da Silva, L Carrizales, and S M Seltzer. Final report of the sim 60 co absorbed-dose-to-water comparison sim.ri(i)-k4. *Metrologia*, 45(1A):06011, 2008.

[43] J.H. Scofield. *Theoretical photoionization cross sections from 1 to 1500 keV.* Jan 1973.

[44] P.H.G. Sharpe, K. Rajendran, and J.P. Sephton. Esr dosimetry and applications: Proceedings of the 4th international symposium progress towards an alanine/esr therapy level reference dosimetry service at npl. *Applied Radiation and Isotopes*, 47(11):1171 – 1175, 1996.

[45] R. M. Sternheimer. The energy loss of a fast charged particle by Čerenkov radiation. *Phys. Rev.*, 91:256–265, Jul 1953.

[46] P von Voigts-Rhetz, M Anton, H Vorwerk, and K Zink. Perturbation correction for alanine dosimeters in different phantom materials in high-energy photon beams. *Physics in Medicine and Biology*, 61(3):N70, 2016.

[47] Daniela Wagner, Mathias Anton, and Hilke Vorwerk. Dose uncertainty in radiotherapy of patients with head and neck cancer measured by in vivo esr/alanine dosimetry using a mouthpiece. *Physics in Medicine and Biology*, 56(5):1373, 2011.

[48] Einar Waldeland and Eirik Malinen. Review of the dose-to-water energy dependence of alanine and lithium formate {EPR} dosimeters and lif tl-dosimeters – comparison with monte carlo simulations. *Radiation Measurements*, 46(9):945 – 951, 2011. {EPRBioDose} 2010 International Conference.

[49] Jiang Weber and Walter Barr. Emx user's manual. *The Journal of Chemical Physics*, 1998.

[50] G G Zeng, M R McEwen, D W O Rogers, and N V Klassen. An experimental and monte carlo investigation of the energy dependence of alanine/epr dosimetry: I. clinical x-ray beams. *Physics in Medicine and Biology*, 49(2):257, 2004.